Spatial density and distribution of tumor-associated macrophages predict survival in non–small cell lung carcinoma

Inauguraldissertation
zur Erlangung des Grades eines Doktors der Humanbiologie
des Fachbereichs Medizin
der Justus-Liebig-Universität Gießen

vorgelegt von Xiang Zheng
aus Yunnan, China

Gießen (2021)

Aus dem Fachbereich Medizin der Justus-Liebig-Universität Gießen

Gutachter: Prof. Dr. Rajkumar Savai

Gutachterin: Prof. Dr. Veronika Grau

Tag der Disputation: 8 Oktober 2021

Contents of Dissertation

Introduction 1
Lung cancer 1
Risk factors for developing lung cancer 3
Heterogeneity of NSCLC 4
The tumor microenvironment 5
Cancer-associated fibroblasts (CAFs) 6
T cells 7
Natural killer cells (NK cells) 7
Myeloid-derived suppressor cells (MDSCs) 8
Neutrophils 8
Mast cells (MCs) 9
Dendritic cells (DCs) 9
Tumor-associated macrophages (TAMs) 10
Macrophage development 10
Heterogeneity of macrophage subtypes 11
Multiple phenotypic markers are required to identify TAM subpopulations 14
Spatial heterogeneity of TAM subtypes 15
Significance of TAMs in tumor progression 16
TAM-targeted immunotherapy 18
Interference with TAM survival 19
Inhibition of macrophage recruitment 20
Repolarization of M2 TAMs by manipulation of microenvironment stimuli 23
Multiplex immunofluorescence techniques in cancer research 24
Multiplexed techniques permits comprehensive studies on TME landscape 24
Multiplex immunofluorescence platforms 25
Opal multiplex staining 26
Aim of study 27
Methods 28
Cell culture methods 28
Cell culture 28
Isolation of human peripheral blood monocyte-derived macrophages 28
Generation of mouse bone-marrow derived macrophages 29
Functional assays for cells 29
Proliferation assay 29
Migration assay 30
Cell death assay 30
Tube formation assay 31
Molecular biology and biochemical methods 31
RNA isolation 31
Reverse transcription for cDNA synthesis 32
Quantitative real time polymerase chain reaction (qRT-PCR) 32
Human specimens 39
Flow cytometry and cell sorting 40

RNA sequencing 41
Western blot 41
Cell and tissue morphological techniques 43
Immunocytochemistry (ICC) 43
Haematoxylin & Eosin staining (H&E staining) 44
Immunofluorescence staining (IFC) 44
Opal multiplex staining and multispectral imaging 45
Animal experiments 47
Statistical analysis 48
Results 49
Macrophages consist of antitumoral M1- and protumoral M2-subtypes 49
Gene expression profiling indicates heterogeneity among macrophage populations at the tumor center, invasive margin and non-tumor regions 52
Five specific markers are sufficient for distinguishing M1 and M2 TAM subtypes in lung cancer 55
Higher spatial density of M1 TAMs is associated with significantly longer overall survival of patients with lung cancer 60
Spatial distributions of M1/M2 IM-TAMs are independent survival predictors 66
Proximity of tumor cells to TAMs is associated with tumor cell survival 70
Hypoxia contributes to the accumulation of M2 TAMs 70
Discussion 72
Outlook 79
Can we use RNA-seq-based transcriptomics of macrophages to identify novel lung cancer prognostic markers? 79
How UBXN4/ACTR6/MSFD12 expression influence on lung cancer progression and TAM biology? 80
Can proximity distance between lung cancer cells and other immune cell types predict lung cancer survival? 82
Can we elevate M1 TAM proportion by some clinically feasible approaches? 82
Can we specifically target activated TAMs *in vivo*? 83
How can we apply multiplex staining to improve personalized cancer therapy? 85
Summary 87
Zusammenfassung 88
Appendix 98
List of abbreviation 98
List of reagents 101
List of figures and tables from external sources 102
List of publications 103
List of contributions to the congress 104
Erklärung zur Dissertation 105
Acknowledgement 106

Introduction

Lung cancer

Lung cancer begins in the lungs and may spread to lymph nodes or other organs in the body, such as the brain. Cancer from other organs may also spread to the lungs. According to the GLOBOCAN 2018 database, lung cancer occupies 18.33% cancer mortality around the world. An estimated 2.09 million (95% uncertainty intervals (UI): 2.06–2.13 million) new cases (**Figure 1A**) and 1.76 million (95% UI: 1.70–1.82 million) deaths from lung cancers worldwide in 2018 [1] (**Figure 1B**). There are various risk factors of developing lung cancer, such as cigarette smoking, radiation exposure and environmental toxins [2].

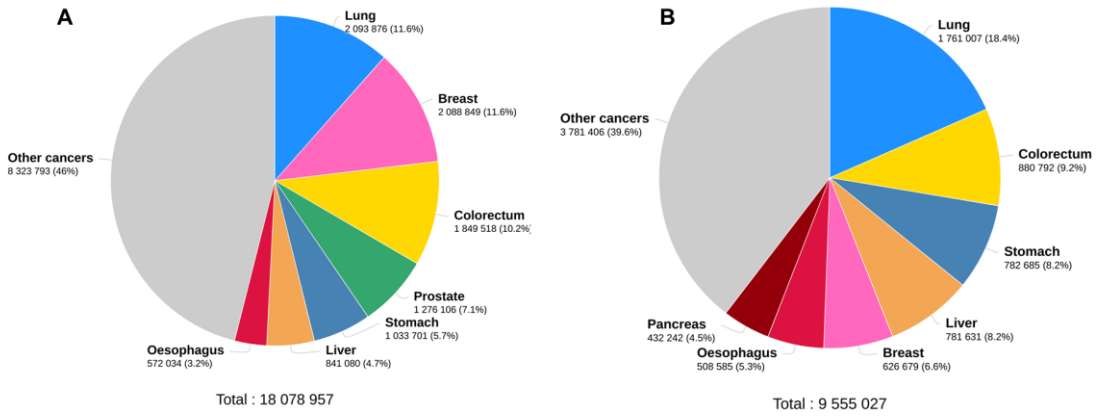

Figure 1 Estimated new cancer cases and cancer death. Data is from GLOBOCAN 2018 database. (A) Estimated new cases of cancer. (B) Estimated cancer death. License details and the terms and conditions provided by John Wiley and Sons and Copyright Clearance Center. License Number: 4940270996559.

Histologically, lung cancer is classified as non-small-cell lung cancer (NSCLC) and small-cell lung cancer (SCLC). NSCLC comprises approximately 85% of lung cancer cases and is subdivided into adenocarcinoma (ADC), squamous cell carcinoma (SCC), and large-cell carcinoma (LCC) [3]. ADC and SCC are the most prevalent histologic subtypes of NSCLC, accounting for around 40% and 27% of NSCLC cases, respectively [4]. Given that targetable driver mutations are mainly identified in ADC and inappropriate drugs need to be avoided for patients with SCC, it is beneficial to differentiate ADC from SCC in terms of effective therapy [3]. Morphologically, ADC is defined as carcinoma with an acinar/tubular structure or mucin production, whereas SCC is defined as carcinoma with keratinization or intercellular bridges. ADC can present diverse histological patterns including lepidic, acinar, papillary, micropapillary, and solid patterns. In current World Health Organization (WHO) classification, a poorly differentiated carcinoma without

glandular structures or mucin production, but with immunohistochemical positivity for "adenocarcinoma markers" such as TTF-1 (NKX2-1) and/or Napsin A is diagnosed as an adenocarcinoma. A poorly differentiated carcinoma without keratinization or intercellular bridges, but with immunohistochemical positivity for "squamous cell carcinoma markers" such as p40, CK5/6, and TP63 (p63) is diagnosed as squamous cell carcinoma [3]. Large-cell carcinoma, accounting for approximately 10% of all lung cancers, is an undifferentiated malignant epithelial tumor. They morphologically have lobular, trabecular, or palisading growth patterns surrounding comedo-type necrosis. Immunohistochemistry reveals that large-cell carcinomas commonly express cytokeratin but not TTF-1 or p63. SCLC, which comprises approximately 15% of lung cancer, is a neuroendocrine tumor with more than 10 mitoses per 2 mm^2 and small cell cytological features [5]. SCLC frequently demonstrates multiple oncogenic mutations and has inactivation of the tumor suppressor genes *p53* and *RB1* [5].

Alterations of various oncogene and tumor suppressor genes represent predictive, prognostic or therapeutic biomarkers for lung cancer. Predictive biomarkers are identified to predict the response of the patients to a targeted therapy. Epidermal growth factor receptor (EGFR) is overexpressed in 40–80% and mutated in 10-35% of NSCLC. Tumors with EGFR mutations are highly responsive to treatment with EGFR tyrosine kinase inhibitors (EGFR TKIs) such as gefitinib, erlotinib, and afatinib[6]. Additionally, translocation of anaplastic lymphoma kinase (*ALK*) is identified in 3-7% of lung tumors [6]. Nucleophosmin (*NPM*), echinoderm microtubule-associated protein-like 4 (*EML4*), kinesin family member 5B (*KIF5B*) and trafficking from ER to golgi regulator (*TFG*) are common fusion partners of *ALK*. Crizotinib, a selective ALK inhibitor, suppresses the proliferation of cells carrying genetic alterations in ALK. Moreover, less than 5% of NSCLC possess activating mutations in the tyrosine kinase domain of human epidermal growth factor receptor 2 (*HER2*). The most common mutation of *HER2* is a 12-base pair duplication/insertion of the amino acid sequence YVMA in exon 20 at codon 776[5]. 1-2% NSCLC are detected with *ROS1* rearrangements that lead to constitutively active fusion proteins, including *SLC34A2-ROS1*, *CD74-ROS1*, *EZR-ROS1*, *TPM3-ROS1*, and *SDC4-ROS1*. NSCLC patients harbor *ROS1* rearrangements can benefit from crizotinib treatment[7]. Similar to *ROS1*, *RET* rearrangements are identified in 1–2% of NSCLC, including *CCDC6-RET*, *NCOA4-RET* and *TRIM33-RET*. RET inhibitors such as vandetanib, sorafenib, sunitinib and cabozantinib are promising targeted therapy for RET fusion-positive lung carcinoma cases[5]. Besides, *NTRK1* fusions are detected in 3.3% of

the ADC cases (3 out of 91 patients)[8]. Overexpression of MET and HGF protein in NSCLC are associated with higher pathologic tumor stage and worse prognosis [5]. Activating kirsten rat sarcoma viral oncogene homolog (*KRAS*) gene point mutations of which 12 and 13 in exon 1 are most frequent mutation positions are detected in 15-25% of lung adenocarcinoma patients[5]. *BRAF* mutations in NSCLC are also most frequently in adenocarcinomas and BRAF inhibitors such as vemurafenib and dabrafenib demonstrated clinical benefit. Furthermore, mutation rate of neuroblastoma RAS Viral (V-Ras) oncogene homolog (*NRAS*), v-AKT murine thymoma viral oncogene homolog 1 (*AKT1*), mitogen-activated protein kinase 1 (*MAP2K1*), phosphatidylinositol-4,5-bisphosphate 3-kinase, catalytic subunit alpha (*PIK3CA*) is relatively low (approximately 1%) in NSCLC [5]. Aside from gene mutation, misregulation of gene expression is also investigated to be predictive biomarkers. For instance, overall lower levels of BRCA1 is associated with greater responses to platinum-based and paclitaxel-based chemotherapy and improved survival [9]. Low ribonucleotide reductase M1 (RRM1) is associated with a better response to gemcitabine-based regimens and better overall survival [10].

Tumor staging is the most pivotal prognostic factor in predicting recurrence rates and survival times. TNM staging system using tumor size, local invasion, and the presence of nodal and distant metastases remains the prevailing method to predict patient survival with 5-year stage-specific survival rates ranging from 81% in stage IA disease to 5% in stage IV disease [11]. In addition to TNM stage, factors that include tumor grade, sex, age over 65 years, smoking status, performance status, comorbidities, type of pulmonary resection, and hospital case volume have been shown to have prognostic value[12]. Combination of TNM stage and molecular biomarkers can yield more precise, individualized survival estimates and treatment algorithms. EGFR and B cell lymphoma 2 (Bcl-2) are considered as favorable prognostic markers and HER-2, vascular endothelial growth factor (VEGF), KRAS, TP53 and Ki-67 are applied as poor prognostic markers[13]. Additionally, late diagnosis of lung cancer is very common in clinical practice, and approximately 67% of patients are at or above stage III before treatment [4]. Further investigations on tumor biology and rapid molecular analysis will improve risk stratification and match potential treatment to individual patients to generate more precise survival prognostication and more individualized treatment plans.

Risk factors for developing lung cancer

There are various risk factors for developing lung cancer, including cigarette smoking,

radiation exposure, and environmental toxins such as asbestos and arsenic [2]. Smokers have at least a 20-fold increased risk of developing lung cancer compared with lifelong non-smokers with a strong association with small cell and squamous histology [14]. Smoking includes not only cigarettes, but also cigars, pipes, electronic nicotine delivery systems and second-hand smoke. Family history of lung cancer displays more than a threefold higher lung cancer risk of smokers compared with non-smokers [15]. In addition, occupational exposure, including work involved in aluminium production, coal gasification, coke production, hematite mining, iron and steel founding, painting and rubber production, increases lung cancer risk [16]. Aside from occupational exposure, environmental exposure is associated with increased risk of lung cancer, including air pollution, indoor pollution from burning coal or cooking oil fumes without appropriate ventilation, water contaminated with high concentrations of arsenic [16]. Besides, lung cancer risk is significantly increased in patients treated for Hodgkin's lymphoma that is associated with radiotherapy and chemotherapy with alkylating agents [17]. Moreover, some diseases are linked with higher risk of lung cancer. Individuals with HIV infection have a threefold increase of risk for lung cancer compared with the general population [18]. Inflammation is one of the hallmarks of cancer and previous lung disease, including emphysema, chronic bronchitis, pneumonia and tuberculosis, predisposes to lung cancer [19].

Heterogeneity of NSCLC

In-depth analyses of lung cancer genomes and signaling pathways have revealed genetic and cellular heterogeneity of NSCLC. Aside from aforementioned genetic mutations and genomic heterogeneity, tumor cells are heterogeneous among each other. Some patients who were initially diagnosed with EGFR-driven ADC develop SCLC after long-term treatment with the EGFR tyrosine kinase inhibitors gefitinib or erlotinib [20]. This observation indicates cancer stem cells occur in lung cancers with a high degree of plasticity. Each subset of NSCLC might harbor cancer stem cells with unique surface markers and molecular drivers, which could each be uniquely targeted. Various subsets of NSCLC might not only have one cancer stem cell population [21]. Further careful evaluation of cancer stem cell activity and plasticity using patient-derived xenograft (PDX) models and multiple genetically engineered mouse models will help us to better understand tumor lineage conversion as a path towards developing chronic treatment resistance [21]. Tumor heterogeneity is revealed by not only distinct tumor epithelial cells

but also the diverse microenvironments with which the tumor cells interact. Lung cancer cells are closely associated with the extracellular matrix (ECM), mesenchymal cells such as fibroblasts, infiltrating immune cells and vasculature. Heterogeneity of intratumoral localization manifests prognostic values. For instance, infiltration of $CD8^+$ T cells are heterogeneous between tumor center (TC) and invasive margin (IM). Higher $CD8^+$ T cell infiltration in TC was associated with better overall lung cancer patient survival, while high $CD8^+$ T cell density in IM was not significantly associated with patient survival [22]. Furthermore, deluge of evidence has suggested that cancer stem cells are enriched in the heterogeneous manner especially at IM. Cancer cells at IM are expected to be composed of both CD44v8-10^{high}Fbw7^{high}/c-Myc^{low} quiescent phenotype and CD44v8-10^{high}Fbw7^{low}/c-Myc^{high} proliferative phenotype. Cancer stem cell heterogeneity at IM manifests the dynamic tumor evolution with the selective pressure of antitumoral treatments [23]. Spatial heterogeneity of immune cell infiltration requires further consideration in regards to prognostic value evaluation.

The tumor microenvironment

Numerous cancer risk factors can be linked to chronic inflammation which is recognized as a hallmark of cancer [24]. The physiological microenvironment of any given organ is usually antitumoral, yet the microenvironment is vulnerable to chronic inflammation caused by, for example, microbial infection or triggers that induce sterile inflammation. As a result, a protumoral microenvironment (TME) can be established. TME is composed of tumor cells, vascular and lymphatic endothelial cells, pericytes, fibroblasts, immune cells, an altered ECM and is in early stages restricted by a basement membrane [25]. The main populations of protumoral inflammatory cells are tumor-associated macrophages (TAMs), myeloid-derived suppressor cells (MDSCs), natural killer (NK) cells, mast cells (MCs), neutrophils, dendritic cells (DCs) and T cells (**Figure 2**). The TME has a fundamental role in tumor progression, metastasis and immunosuppression, and it also accounts for the resistance of tumor cells to drug treatment [25]**.** Therefore, remodeling of the TME provides novel and promising opportunities for cancer therapy.

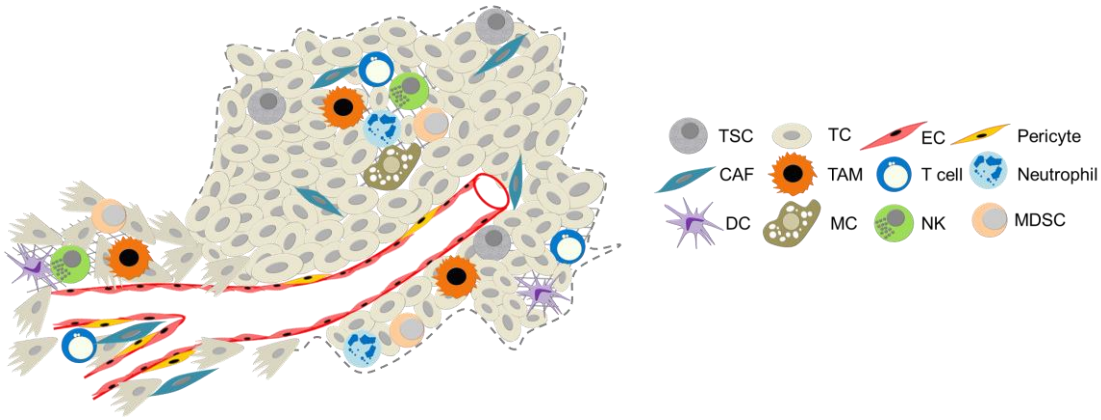

Figure 2 Tumor microenvironment. TSC, tumor stem cell; TC, tumor cell; EC, endothelial cell; CAF, cancer-associated fibroblast; TAM, tumor-associated macrophage; MDSC, myeloid-derived suppressor cell; NK, natural killer cell; DC, dendritic cell; MC, mast cells.

Cancer-associated fibroblasts (CAFs)

CAFs are one of the most dominant components in the tumor stroma and remodel the extracellular matrix (ECM) structure. As the cancer progresses, CAFs continuously release growth factors such as transforming growth factor beta (TGFβ) that can regulate the epithelial–mesenchymal transition (EMT) [26,27]. CAFs acquire the features of myofibroblasts, including increased production of α-smooth muscle actin (α-SMA), whereupon they facilitate tumor initiation and progression[26]. In addition to TGFβ, CAFs release stromal cell-derived factor 1 (SDF-1/CXCL12), which recruits endothelial progenitor cells to the tumor site to facilitate angiogenesis and directly promote tumor growth via binding to its cognate receptor, CXCR4, expressed by cancer cells [26]. SDF-1/CXCL12 production by CAFs is also a chemoattractant of macrophages and promotes M2 macrophage polarization in prostate cancer [28]. CAFs secrete CC chemokine ligand 2 (CCL2), which recruits macrophages to the tumor site through binding to its receptor CCR2 [27] (**Figure 3**). Aside from cytokine and chemokine secretion, modulation of the ECM by CAFs also promotes the enrichment of macrophages. Hyaluronan is a major component of the ECM, and TAMs are preferably attracted to hyaluronan-rich stromal areas [29]. Depletion of hyaluronan synthase 2 in CAFs reduces TAM recruitment and thereby attenuating tumor angiogenesis and lymphangiogenesis [29]. Martinez-Outschoorn et al. suggested an "autophagic tumor stroma model of cancer metabolism" as a mechanism for the protumoral effect of CAFs. Specifically, they propose that tumor cells induce hypoxia-inducible factor 1α (HIF-1α) and nuclear factor κB (NF-κB) in CAFs and drive autophagy in CAFs, leading to nutrient release to support tumor cell metabolism [30].

T cells

T cells are widely distributed within tissues and the TME. Naive T cells are rapidly activated and differentiate into effector T cells that include both $CD8^+$ cytotoxic lymphocytes (CTL) and $CD4^+$ helper T cells upon antigen stimulation [31,32]. The mechanisms underlying T cell cytotoxicity are the granzyme–perforin pathway and killing systems such as Fas/FasL and tumor necrosis factor α (TNF-α)/TNF receptor 1 [31]. Most effector T cells die by apoptosis after antigen clearance, but a small fraction of them differentiate into memory T cells that quickly respond when the same antigen reappears. However, the extent and persistence of antigenic stimulation appear to be vital factors leading to T cell dysfunction and are associated with the severity of dysfunction during chronic infections and cancer [32]. The acquired dysfunction is related to the co-expression of multiple inhibitory receptors including programmed cell death protein 1 (PD-1), cytotoxic T lymphocyte antigen 4 (CTLA-4), T-cell immunoglobulin domain and mucin domain-3 (Tim-3), lymphocyte activation gene 3 (LAG-3), T cell immunoreceptor with Ig and ITIM domains (TIGIT). Overexpression of PD-1 is one of the major markers of T cell dysfunction and blocking PD-1 or its ligand PD-L1 successfully reactivates T cell function [32].

Natural killer cells (NK cells)

NK cells are innate cytotoxic cells that kill malignant cells without prior sensitization through granule exocytosis or death receptor ligation. Human NK cell inhibitory receptors consist of the killer immunoglobulin-like receptors (KIRs) and the lectin-like receptor NKG2A. KIRs bind to human leukocyte antigen (HLA)-A, -B, or -C, whereas the CD159/CD94 complexes ligate HLA-E [33,34]. NK cell activation receptors can be grouped into three categories: those that associate with immunoreceptor tyrosine-based activation motif (ITAM)-containing subunits, the DAP10-associated NK group 2 member D (NKG2D) receptor and a number of other receptors including DNAX accessory molecule-1 (DNAM-1), CD2 and 2B4 [34]. Tumor cells evade NK cell attack through following approaches: 1) upregulation of MHC class I expression; 2) shedding of soluble ligands for NK cell activation receptors; 3) releasing inhibitory cytokines; 4) activating inhibitory regulatory T cells; 5) killing immature dendritic cells to prevent NK cell priming; 6) releasing phagocyte-derived inhibitory cytokines and 7) reducing the number of NK progenitor cells to lower NK cell counts [33-35].

Myeloid-derived suppressor cells (MDSCs)

MDSCs are immature myeloid cells that suppress immune responses and expand during cancer, infection, and inflammatory diseases. The role of MDSCs in solid tumors has been extensively characterized as protumorigenic [36]. MDSCs in human consist of two main subtypes-monocytic-MDSCs (M-MDSCs) are defined as $CD11b^{+}CD14^{+}HLA\text{-}DR^{low/-}CD15^{-}$ cells, and human granulocytic-MDSCs (G-MDSCs) are defined as $CD11b^{+}CD15^{+}CD14^{-}$ or $CD11b^{+}CD14^{-}CD66^{+}$ cells [36]. MDSCs greatly influence the immunosuppressive effects of the TME by impairing $CD8^{+}$ T cell and NK cell functions. They release limited amounts of nitric oxide by expressing both inducible nitric oxide synthase (iNOS) and arginase 1. They induce the differentiation of Tregs that maintain an immunosuppressive environment by secreting TGFβ and interleukin 10 (IL10) and competitively binding and neutralizing the antitumoral cytokines, such as IL2, IL7, IL12 and IL15 [37,38]. TAMs enhance MDSC production of IL10, depending on which macrophage production of IL12 is reduced (**Figure 3**) [39]. Hence, MDSCs are impediment of effective immunotherapy and their reduction may facilitate immunosurveillance to suppress tumor progression [39].

Neutrophils

Neutrophils make up 50–70% of circulating leukocytes and an elevated number of neutrophils indicates a poor prognosis in colon carcinoma, bronchioloalveolar carcinoma, gastric carcinoma, renal carcinoma and melanoma [40]. Neutrophils in TME can be categorized into antitumoral (N1) and protumoral (N2) subtypes. Depletion of TGFβ drives conversion of N2 to the N1 state [41]. Neutrophils are recruited to the tumor site through TME-generated chemokines binding to CXCR1 and CXCR2. Once in tumors, N2 subtypes release factors such as oncostatin M that induce tumor cells to produce VEGF and matrix metallopeptidase 9 (MMP9) to facilitate angiogenesis [42]. Although activated neutrophils which secrete IL8 and TNFα recruit macrophages to the site of inflammation, it remains unknown whether the interaction between neutrophils and TAMs in the TME is comparable to that in non-tumoral chronic inflammatory environment [42] (**Figure 3**).

Mast cells (MCs)

MCs are granulocytic immune cells that play multifaceted roles in tumor progression and inhibition. The multifaceted feature of MCs is due to plastic potential to generate pro- or antitumoral subtypes in response to specific TME stimuli [43]. Histamine produced by MCs polarizes $CD4^+$ T cells toward a Th2 phenotype that favors tumor development through histamine receptor type 2 (H2R). In addition, histamine recruits regulatory T cells (Tregs) to establish an immunosuppressive microenvironment [43]. Furthermore, MCs recruit TAMs to promote tumor invasion via activated PI3K/AKT pathway in inflammation-induced colon cancer [44]. Thus, MCs contribute to mold the TME by interacting with other tumor-infiltrating immune cells, which engenders the opportunity to develop MC-targeted therapies for cancer patients [45].

Dendritic cells (DCs)

DCs are professional antigen-presenting cells. Conventionally, intracellular antigens, such as viral proteins, are presented on MHCI molecules to $CD8^+$ T cells, whereas extracellular antigens, such as bacteria and toxins, are presented on MHCII molecules to $CD4^+$ T cells. However, DCs have the ability to cross-present extracellular antigens to $CD8^+$ T cells, which is important for antitumoral immunity. The mechanism by which the TME inhibits the ability of DCs to present antigens effectively is to retain DCs in an immature state, which blocks expression of co-stimulatory molecules, resulting in tolerance through T cell deletion [46]. Additionally, TAM-derived IL10 inhibits the production of IL12 by dendritic cells, ultimately leading to suppressed $CD8^+$ T cell responses and DC antitumoral functions (**Figure 3)** [47].

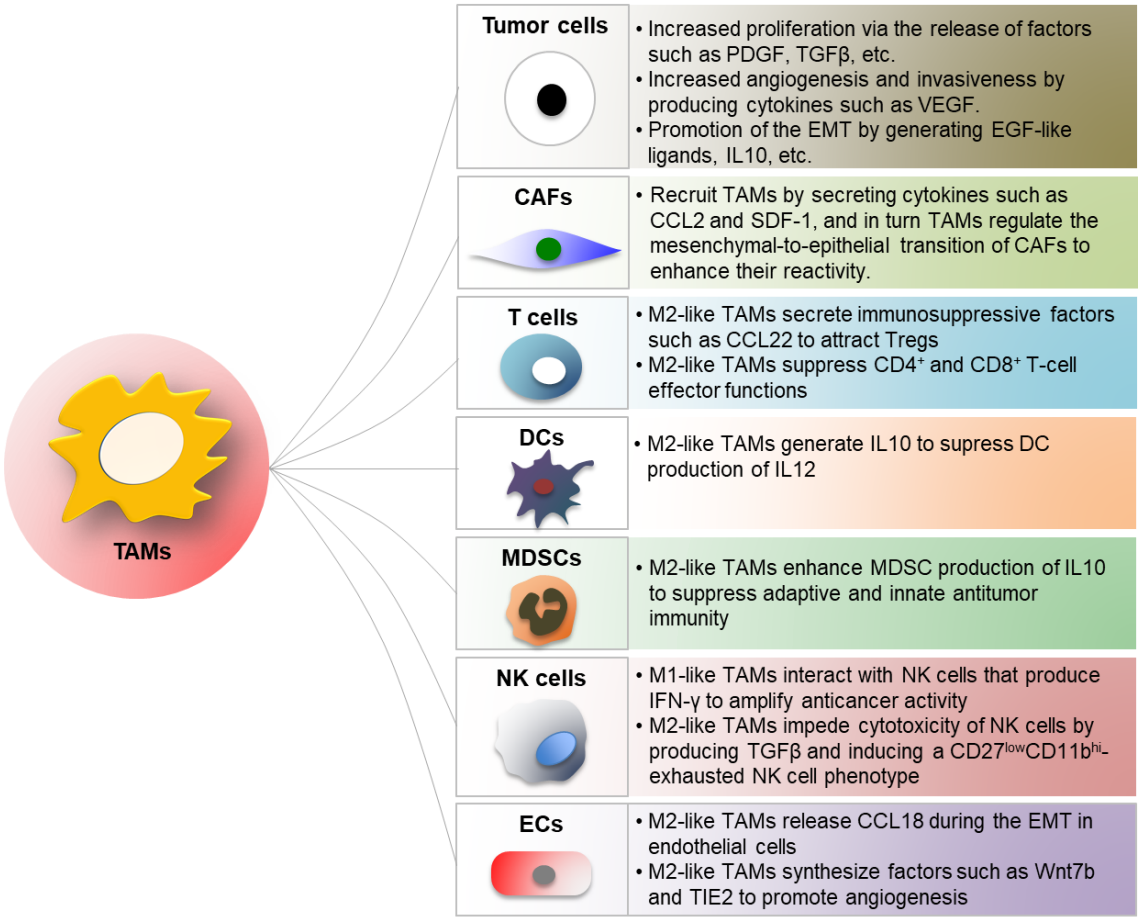

Figure 3 Influence of TAMs on other cells in TME. TAMs interact with tumor cells and other tumor-infiltrating immune cells to influence tumor angiogenesis, invasion as well as metastasis. Some of the interactions mentioned in this review are depicted in the figure. TAM, tumor-associated macrophage; CAF, cancer-associated fibroblast; MDSC, myeloid-derived suppressor cell; NK, natural killer cell; DC, dendritic cell; Treg, regulatory T cell; EC, endothelial cell. Adapted from Zheng et al., 2017 [45]. Reuse permission: distributed under the terms of Creative Commons Attribution 3.0 License.

Tumor-associated macrophages (TAMs)

Macrophage development

Macrophages play important roles in shaping tissues during embryogenesis. They appear from embryonic day 8 (E8) in mice and are involved in branching morphogenesis, the generation of adipose tissue and vascular patterning [48]. In the embryo, the earliest macrophages are derived from mesenchymal progenitors in the yolk sac. Subsequently, they migrate into embryonic tissues as soon as a functional vasculature is established. Accumulating studies indicate that yolk sac–derived macrophages are long-lived, self-sustaining cells [48]. A second wave of tissue macrophages is derived from erythro-myeloid progenitors (EMPs) that colonize the fetal liver at approximately E9. EMPs differentiate into pre-macrophages and subsequently colonize embryonic tissues to differentiate into

tissue-specific macrophages. These EMP-derived macrophages are again long-lived and self-sustaining [49]. Hematopoiesis in bone marrow starts after birth, generating bone marrow–derived monocytes as a third wave of macrophage progenitors. In contrast to embryonic macrophages, bone marrow–derived macrophages are usually short-lived, rarely proliferate and continuously replaced [48,50]. Therefore, a mixture of macrophages arising from different progenitors during ontogeny could be expected in adult tissues.

However, the tissue macrophage pool in adult organs shows some degree of specificity. For example, yolk sac macrophages constitute the vast majority of microglia in the central nervous system owing to establishment of the blood–brain barrier during embryogenesis, which precludes the influx of fetal or adult monocytes [48]. In other tissues, yolk sac macrophages are replaced by fetal EMP-derived or adult monocyte-derived macrophages to some extent [49]. For instance, adult epidermal macrophages, Langerhans cells and alveolar macrophages are derived from EMP-dependent macrophages that proliferate locally, whereas dermal macrophages and intestinal macrophages are constantly replenished by adult monocytes and do not proliferate *in situ*. Furthermore, origins of tissue macrophage change if the tissue is subjected to inflammation because inflammatory monocytes are recruited to the inflamed areas from the circulation and differentiate into macrophages [48,50]. As for the origin of TAMs, a study using primary mouse mammary tumor suggests that most of TAMs arise from the circulating $Ly6C^{hi}CCR2^{hi}$ monocytes derived from bone marrow hematopoietic stem cells [51]. Moreover, proliferation of resident macrophages and *in situ* monocyte-macrophage differentiation are the other origins of TAMs [52], and photoconvertible fluorescent lineage tracing of spleen indicates splenic monocytes are a minor source of TAMs [53]. Thus, both the original macrophage pool of a tissue and adult monocytes might contribute to the pool of TAMs in cancer [51]. However, local TME, shaped by a varying content of cytokines, growth factors and oxygen, as well as the presence of tumor cells, rather than ontogeny, appear to contribute to TAM function [54,55].

Heterogeneity of macrophage subtypes

Macrophages are innate immune cells that specialize in maintaining tissue homeostasis. They command a broad sensory arsenal to detect perturbations in tissue integrity and possess a remarkable functional plasticity to combat diseases [48]. Macrophages reside in distinct tissues, including the liver (kupffer cells, which are involved in iron storage, steatosis and liver repair), lungs (alveolar macrophages, which contribute to clearance of

particulates), brain (microglia, which play a role in the removal of naturally aging neurons), skin (Langerhans cells, which are involved in antimicrobial immunity and skin immunosurveillance), spleen (splenic macrophages, which assist in the transport of microbial antigens to B and T cells and clear aged red blood cells) and other tissues, such as the gastrointestinal tract, cardiovascular system and granulomata [50]. That macrophages possess specialized functions in distinct anatomical locations underscores their heterogeneity.

The lineage-determining transcription factor for macrophages is PU.1, which determines the availability of factors necessary to generate the vast spectrum of different tissue macrophages [55]. Other stimulus-specific transcription factors include myocyte-specific enhancer factor 2c and SMAD in microglia, PPARγ in alveolar macrophages, PU.1-related factor (SPI-C) in iron-recycling macrophages of the spleen and bone marrow and GATA binding protein 6 (GATA6) in peritoneal macrophages [55]. These examples illustrate that the tissue microenvironment likely dictates the genetic signature of its resident macrophages by inducing expression of specific transcription factors.

Independence of genetic imprinting owing to ontogeny or differentiation in a specific steady-state microenvironment, macrophages need to retain a high level of functional plasticity to respond to inflammatory stimuli of varying nature [54,55]. Indeed, a plethora of macrophage phenotypes can be induced by different stimuli or by the same stimulus at different concentrations or different exposure times [56]. Following early observations of macrophage heterogeneity, two discrete activation states of macrophages are identified. Macrophage activation by activated Th1 cell–derived IFNγ in combination with TNFα or the activation of toll-like receptors (TLRs) by bacterial cell wall components such as lipopolysaccharides (LPS) creates cells with a strong pro-inflammatory profile [57]. IFNγ–stimulated macrophages show a transcription factor signature characterized by signal transducer and activator of transcription 1 (STAT1) and interferon regulatory factor 3 (IRF3) [56,57]. These transcription factors enable ‘classically activated’ M1 macrophages to generate pro-inflammatory mediators such as TNFα, IL1B, IL12, IL23 and reactive oxygen and nitrogen species and to present antigens to T cells via induction of MHCII molecules [54,57]. M1 macrophages are potent defenders against microbes and are able to eliminate tumor cells. In contrast, macrophage activation by activated Th2 cell–derived IL4 or IL13 produces an alternative set of cytokines and chemokines that oppose the repertoire of classically activated M1 macrophages, and these ‘alternatively activated’ macrophages are designated as M2 macrophages. In addition to expressing phagocytic

receptors such as the mannose receptor (CD206), M2 macrophages also produce the ECM components and growth factors to promote tissue remodeling and combat extracellular parasites [57], and their transcription factor profile is dominated by STAT6 and IRF4 [57]. Although the M1 and M2 macrophage distinctions are helpful for investigation, they hardly do justice to the multitude of macrophage phenotypes that are observed in tissues. Moreover, macrophage activation states are more transient than the stable M1/M2 activated macrophages, which maintain functional flexibility. Macrophage responses to any stimulus change over time and usually revert to the original state, and M2 macrophages readily acquire even more potent M1-associated functions when they are subsequently stimulated with TLR ligands or IFNγ [54,58]. The ability to switch phenotypes enables macrophages to perform different tasks sequentially during the course of an inflammatory reaction, including pathogen killing, engulfing and digesting cellular debris, stimulating adaptive immunity and promoting tissue regeneration (**Figure 4**) [54,55,57].

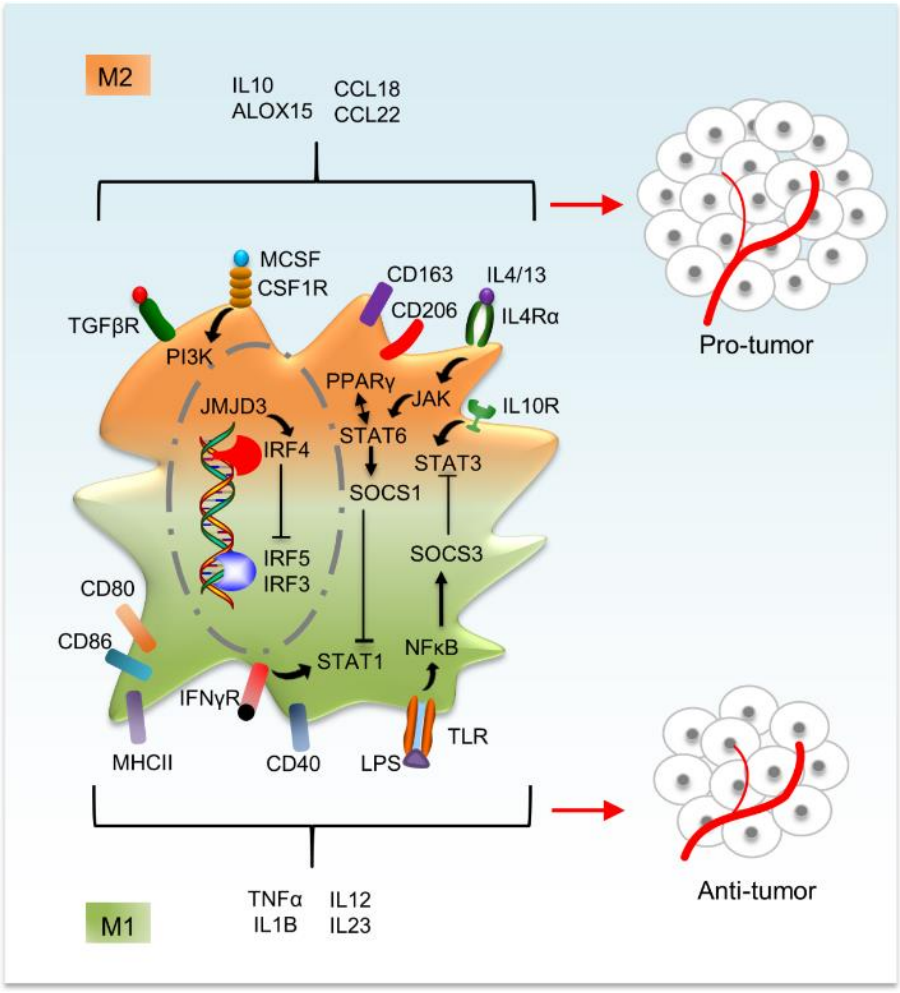

Figure 4 Macrophage activation phenotypes. Macrophages are activated either classically (M1 phenotype) or alternatively (M2 phenotype). M2-polarized macrophages

express high levels of CD206, CD163 and TGFβR, whereas M1 macrophages express high levels of CD40, CD80 and CD86 on the cell surface. STAT1 and STAT3 are highly activated in M1 phenotype and STAT6 in M2 phenotype. IRF3, 5 and 7 are activated in M1 phenotype, whereas IRF4 is activated in M2 phenotype. High levels of the cytokines and chemokines such as TNFα, IL1B and IL12 are observed in M1 phenotype and factors such as IL10, ALOX15 and CCL18 are highly expressed in M2 phenotype. Adapted from Zheng et al., 2017 [45]. Reuse permission: distributed under the terms of Creative Commons Attribution 3.0 License.

Multiple phenotypic markers are required to identify TAM subpopulations

To properly describe macrophage activation and achieve experimental standards, Murray et al. recommended a reproducible experimental standard and summarized marker systems for activated macrophages. Human IL4-induced M2 macrophage markers include ALOX15, CD163, IRF4, SOCS1, GATA3, CCL4, CCL13, CCL17, CCL18. CD206, STAB1, FN, TGFB1, MMP1, MMP12, TG, F13A1, TGM2, ADORA3 and IL17RB. Human LPS+IFNγ-induced M1 macrophage markers include IL12B, IL12A, CCR7, pSTAT1, IRF5, IRF1, TNFα, IL1B, IL23A, CCL5, CXCL9, CXCL10, CXCL11, IDO1, KYNU, GBPI and CD40. Mouse Il4-induced M2 macrophage markers include Arginase, Chitinase, pSTAT6, pSTAT1, Ifr4, Socs2, Ccl17, Ccl24, Ccl22, Retnla and Alox15. Mouse LPS+Ifnγ-induced M1 macrophage markers include Tnfα, iNOS, Il12a, pSTAT1, pSTAT6, Socs1, Nfkbiz, Irf5, Il23a and Il27 [59].

Although there is ample evidence that TAMs are preferentially M2-polarized (for instance, roughly 70% of TAMs are M2-polarized in non-small cell lung cancer), the basis of the regulation and maintenance of this polarization imbalance remains unclear [60,61]. In the TME, several factors can impact on the macrophage phenotype. Cytokines such as TGFβ, IL10 and IL4; growth factors such as epidermal growth factor (EGF), macrophage colony-stimulating factor (M-CSF) and granulocyte-macrophage colony-stimulating factor (GM-CSF) and lipid mediators such as sphingosine-1-phosphate (S1P) and prostaglandin E2 (PGE2) promote a protumoral phenotype [62-64]. However, mixed polarization phenotypes have been described in human ovarian carcinoma and pancreatic ductal adenocarcinoma [65,66]. In ovarian carcinoma, the expression of the M2 marker CD163 on TAM surface correlates with patient relapse-free survival, although gene expression profiles reveal an unrelated M1/M2 mixed-polarization phenotype [66]. CD163 expression also correlates with the levels of IL6 and IL10, which exhibit context-dependent pro-inflammatory and/or anti-inflammatory functions [66]. Although expression of CD206 is not associated with survival benefit of breast cancer patients, the presence of

subsets of $CD206^+$ TAMs, expressing SERPINH1 and collagen 1, or MORC4 are associated with improved breast cancer patient survival [67,68]. Freshly isolated TAMs from pancreatic ductal adenocarcinoma display M1 (HLA-DR, IL1B, TNFα) and M2 (CD163, IL10) characteristics [65]. A mixed phenotype is also evident at the transcriptional level, where differential expression of signal transducer and activator of transcription 1 (*STAT1*) and *STAT3* lead to gene expression profile that cannot be categorized exclusively as M1 or M2 [56]. Furthermore, TAM heterogeneity also depends on their localization. Perivascular migratory TAMs are $CD68^+MHCII^{hi}CD206^{low}$ and have a more M1-like profile. Sessile TAMs resemble a more M2-like or "trophic" phenotype, which are $CD68^{hi}MHCII^{low}CD206^{hi}$ and are mainly found at the tumor–stroma border and in hypoxic regions within the tumor mass [62,69]. Indeed, solid tumors contain areas of hypoxia that triggers increased accumulation of macrophages and leads to upregulation of HIF-1α and HIF-2α, which enhance HIF-mediated expression such as VEGF and the glucose receptor GLUT1 in TAMs, to contribute to tumor angiogenesis and sustains tumor progression [70]. Also, the stability of HIF-1α and HIF-2α is controlled by PTEN/PI3K/AKT signaling axis - expression of PTEN and inhibition of PI3K/AKT signaling induces the degradation of HIF-1α and HIF-2α in a proteasome-dependent manner in TAMs [70]. Additionally, the localization of TAMs in hypoxic niches is controlled by a Sema3A/Neuropilin-1 signaling axis, which elicits PlexinA1/PlexinA4-mediated stop signals that maintain TAMs in hypoxic area [71]. And tumor hypoxia selectively promotes M2 macrophage polarization by activating ERK signaling triggered by IL6 in Lewis lung carcinoma [72]. Therefore, multiple phenotypic markers are required to identify TAM subpopulations and predict their impact on cancer prognosis.

Spatial heterogeneity of TAM subtypes

Recent literatures suggest topologically distinct distribution of immune cells within the TME. For example, the prognostic impact of $CD8^+$ T cell density with survival is highly significant at IM in contrast with TC of lung cancer [73]. In NSCLC, the immune infiltrate at IM is dominated by B cells, and Th2 is predominantly expressed in stromal lymphocytes, while Th1 is most commonly expressed in intraepithelial immune cells, indicating the immune tumor microenvironment of NSCLC is complex and partially heterogeneous. However, distribution patterns of TAMs and TAM phenotypes between TC and IM in lung cancer remain unexplored [74]. M2 TAM density is different between TC and IM, with higher proximity between tumor cells and M2 TAMs, indicating TAMs

in situ are not just randomly distributed but are influenced by their proximity to tumor cells and the tumor microenvironment [75]. In addition to genomic heterogeneity of immune cells, their spatial distribution may be particularly relevant to tumor progression [74,76]. Close interactions among immune and tumor cells generate complex ecological dynamics that can ultimately influence tumor progression and response to treatment [77,78]. Hence, the proximity of immune cells to tumor cells may have profound influence on both cell types as this allows them to interact via soluble factors or cell-cell contact. These analyses could be linked to prognosis and treatment outcomes and computational immuno-oncology models to guide prognostic evaluation and patient stratification and identify predictive biomarkers for responder/non-responder characterizations.

Significance of TAMs in tumor progression

A clear contribution of TAMs to disease progression has been shown in multiple cancer types, holding promise for the development of innovative macrophage-based prognostic and therapeutic tools. High density of macrophages is associated to poor prognosis in many human cancer types, including breast, bladder, prostate, head and neck, glioma, melanoma, and non-Hodgkin lymphoma [79]. While high infiltration of macrophage correlates with better prognosis in colorectal and gastric cancer. The intrinsic variety of the tissues, the approaches to identify diversity of macrophages, and the cancer regions chosen to study macrophages to investigate their correlation with patient prognosis might contribute to the heterogeneity of these studies. Therefore, more critical phenotyping with retention of spatial context is required to unearth the complexity of macrophage.

Different mechanisms govern tumor initiation and progression promoted by TAMs. Macrophages contribute cancer-initiating inflammatory responses because expression of the anti-inflammatory transcription factor STAT3 is inhibited. Genetically inactivating *Stat3* in macrophages gives rise to chronic inflammation in the colon which creates a mutagenic microenvironment and subsequently causes invasive carcinoma [80]. Besides, STAT3 is a critical maintainer of cancer stem-like cells (CSC), and M2 TAMs secrete activators of STAT3 such as oncostatin M and IL10 to promote tumor cell activation and proliferation via interaction between TAMs and tumor cells [81]. Although accumulating evidence suggests an antitumoral role of M1 TAMs [58,82], more studies are required to clearly demonstrate whether macrophages in a cancer-initiating inflammatory environment are capable of eliminating cells that undergo aberrant transformation. In addition, TAMs support tumor development by interacting with T cells. M2 TAMs either

produce immunosuppressive factors such as IL10 and TGFβ to inhibit $CD4^+$ and $CD8^+$ T cell effector function or secrete chemoattractant such as CCL3, CCL4, CCL5, CCL18 and CCL22 to recruit factors associated with Tregs by targeting chemokine receptors CCR4, CCR5, CCR6 and CCR10 to TME to suppress the antitumoral response [51].

TAMs also play a pivotal role in tumor metastasis. VEGF as well as type IV collagenases MMP2 and MMP9 produced by M2 TAMs not only promote tumor growth and angiogenesis, but also cause vascular permeability to facilitate tumor migration [83]. Therefore, TAMs contribute to both intravasation and extravasation. Because recruitment of TAMs to target vessels to induce vascular permeability requires CCL2 and colony-stimulating factor 1 (CSF1) synthesized by tumor cells to target receptor CCR2 and CSF1R on TAMs [27,84], inhibition of CCR2 or CSF1R signaling reduces tumor growth and metastasis [85-88]. Moreover, Toll-like receptor 4 (TLR4) on TAMs can be targeted by serum amyloid A3 to promote metastasis through establishing premetastatic niches that constitute 'homing signals' to provide an environment to guide tumor cell adhesion and invasion [89]. Additionally, EMT is a key step for invasiveness and metastasis of tumor cells and recruitment of TAMs to the tumor site promotes tumor progression by enhancing EMT. Activation of TLR4 on M2 TAMs elevates IL10 production and promotes EMT in pancreatic cancer cells [90]. M2 TAMs secrete EGF-like ligands to activate EGFR pathway in lung cancer cells, which ultimately promoting EMT that can be inhibited by a cannabinoid receptor 2 (CB2) agonist JWH-015 via downregulation of EGFR signaling [91]. Thus, regulation of metastasis-promoting M2 TAMs is a rational method to inhibit tumor metastasis and progression.

TAM metabolism influences the establishment of TME. Hypoxic TAMs exhibit an increased glycolysis rate accompanied by upregulation of growth factors, such as vascular endothelial growth factor (VEGF) and platelet-derived growth factor, which can sustain tumor growth by inducing angiogenesis and metastasis [92]. TAM metabolism can force cancer cells to adopt glycolysis as their primary metabolic pathway, thereby rendering an invasive cancer cell phenotype [93]. In addition, dysregulated metabolism of arginine and tryptophan by TAMs promotes tumor growth and development by impairing the antitumoral immune response [94-96]. Although glucose and amino acid metabolism mostly renders the protumoral phenotype of TAMs, TAMs can use lipid metabolism depending on the tumor stage as either a protumoral or an antitumoral tool [97].

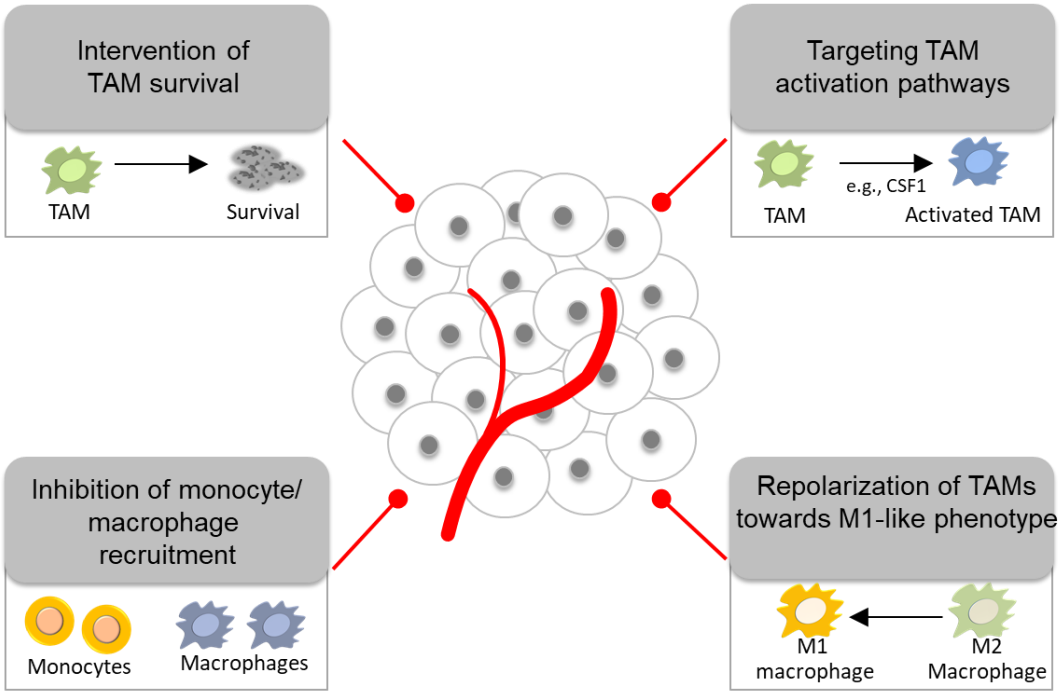

Figure 5 TAM-targeting immunotherapies. These immunotherapeutic strategies include interference with TAM survival and activation, repression of macrophage recruitment and repolarization of protumoral M2 TAMs toward antitumoral M1 TAMs.

TAM-targeted immunotherapy

Aside from conventional therapies, immunotherapy has emerged as an effective strategy for cancer treatment. Vaccination with tumor antigens, adoptive cellular therapy with *in vitro* activated T cells and NK cells, and oncolytic viruses are approaches of immunotherapies to activate effector immune cells. The most promising strategy, which is scheduled to begin clinical application, is administration of antibodies against immune-checkpoint molecules such as CTLA-4, PD1 and its ligand PDL1 to neutralize immunosuppression [98]. Clinical evidence shows that an increased number of M2 TAMs correlates with treatment failure and poor prognosis in different cancers types. And M2 TAMs express not only ligand for CTLA-4 but also PDL1, thereby contributing immunosuppressive activity and providing target for therapy with anti-PDL1 [99]. Analysis of the fractional prevalence of leukocytes among 5,782 tumors based on the iPRECOG dataset showed M2 TAMs are the predominant immune cells in most solid tumors [100]. Unlike T cells which are physically excluded in terms of penetrating a solid tumor to kill malignant cells inside, macrophages are uniquely capable of penetrating solid tumors, which broadens their feasibility in treating lung cancer. Additionally, targeting macrophages might be capable of boosting existing T cell-based antitumoral activity,

increasing the number of immunogenic dendritic cells, whereas reducing the number of regulatory T cells and monocytic myeloid-derived suppressor cells [101,102]. Therefore, TAM-targeting immunotherapies represent a promising cancer therapeutic approach. These immunotherapeutic strategies include interference with TAM survival, repression of macrophage recruitment and repolarization of protumoral M2 TAMs toward antitumoral M1 TAMs (**Table 1**; **Figure 5**).

Interference with TAM survival

Inducing apoptosis of TAMs appears to be an effective immunotherapeutic tactic for tumors. Trabectedin (ET-743) is an antitumoral agent that, with respect to immune cells, is specifically cytotoxic to mononuclear phagocytes. The specificity is due to activation of caspase-8, which is essential for monocyte apoptosis via Fas and TNF-related apoptosis inducing ligand receptors (TRAILRs), whereas neutrophils and T cells are protected from depletion by the presence of a decoy receptor [103]. In addition, liposomal bisphosphonates, which can be phagocytized by macrophages, are widely considered as a promising drug for macrophage ablation. For instance, administration of liposome-encapsulated bisphosphonate clodronate leads to depletion of macrophages and reduces tumor progression [104]. Compared with clodronate liposomes, liposomal trabectedin targets all macrophage subsets in tumors to a similar extent but leads to more persistent macrophage depletion. Mechanistically, trabectedin upregulates TRAIL-R2 and Fas-associated protein with death domain (FADD) that facilitate the recruitment of caspase-8 and the activation of apoptotic cascade in macrophages [103]. However, targeting all subtypes of macrophages is not an ideal way to deplete M2 TAMs. And the issue of introducing specific agents that are more specific to M2 TAMs might be addressed by a peptide (M2pep) with high affinity for murine M2 macrophages, thereby selectively abrogating M2 TAMs and consequently improving the survival rate of tumor-bearing mice [105]. Furthermore, targeting cell surface proteins that are highly expressed in M2 TAMs is a practical approach to reduce TAM survival. Legumain is an ideal target because it is highly expressed in M2 TAMs in murine breast tumor tissues, whereas M1 TAMs do not express legumain. A legumain-based DNA vaccine stimulates $CD8^+$ T cells and selectively abrogates M2 TAMs in mice with metastatic breast, colon and lung cancers , thereby increasing survival rate and regression of metastasis and angiogenesis [106]. Scavenger receptor A (CD204), which is highly and specifically expressed on the surface of M2 TAMs, is also a promising target. Administration of anti-CD204

immunotoxin to mice challenged with peritoneal ovarian cancer eliminates TAMs and impedes tumor progression [107]. An RNA aptamer that targets murine or human IL4Rα/CD124 on TAMs can also promote TAM apoptosis with increasing $CD8^+$ T cell infiltration *in vivo* [108]. Folate receptor β is identified as a marker for M2 TAMs, and targeting this protein using a recombinant immunotoxin in mouse glioma xenografts dramatically abrogates TAMs and suppresses tumor growth [109,110]. Although it is unclear whether depletion of TAMs alone is effective for eliminating human cancer, targeted abrogation of TAMs in conjunction with antitumoral agents may improve cancer therapy.

Inhibition of macrophage recruitment

Tumor-derived chemokines, including CCL2 and CSF1, recruit peripheral monocytes to the tumor site [27]. Within the TME, peripheral monocytes differentiate into antitumoral M1-like or protumoral M2-like subsets in response to distinct microenvironmental signals that are specific to each tumor stage. Therefore, targeting these signaling molecules is another potential strategy to inhibit the accumulation of TAMs.

CCL2 is highly produced by bone marrow osteoblasts, endothelial cells and stromal cells as well as tumor cells, including breast cancer, prostate cancer and myeloma cells [84,85,87]. CCL2 directly promotes tumor cell proliferation, migration and acts as a chemotactic factor to recruit macrophages that express the CCL2 receptor CCR2 to the tumor site, inducing an inflammatory response that promotes tumor growth [87]. Blockade of either CCL2 or CCR2 has shown pre-clinical antitumoral success. The CCL2 inhibitor Bindarit significantly suppresses M2 macrophage recruitment and tumor growth in human melanoma xenografts [85]. Additionally, neutralizing antibodies against CCL2 (anti-human CNTO888 and anti-mouse C1142) in combination with docetaxel diminishes prostate cancer cell–mediated tumor burden and induces tumor regression [86]. Moreover, applying the CCR2 kinase antagonist PF-04136309 to murine pancreatic cancer inhibits M2 macrophage recruitment and reduces cancer progression [87,111]. Our previous study revealed that IL10 drove CCR2 and CX3CR1 upregulation, whereas CCL1, granulocyte colony-stimulating factor (GCSF) and CCL3 are required for upregulation of CCL2 and CX3CL1 [112].

CSF1 and its receptor CSF1R regulate macrophage homeostasis by modulating their proliferation, differentiation and migration. Blockade of the CSF1/CSF1R axis by inhibitors and/or neutralizing antibodies efficiently decreases macrophage recruitment. For instance, each of the CSF1R inhibitors PLX6134, GW2580 and PLX3397 reduces

M2 macrophage infiltration and improves chemotherapeutic efficacy with enhanced $CD8^+$ T cell responses [111]. Besides, inhibition of CSF1 using either an antisense oligonucleotide or anti-CSF1 antibody suppresses macrophage recruitment and results in reduced tumor growth in human MCF-7 breast cancer cell–xenografted mice [113]. From a mechanistic perspective, MMP2, MMP12 and VEGFA, which are produced by macrophages and are important in tumor invasion and angiogenesis, are downregulated upon blockade of the CSF1/ CSF1R axis [113,114]. Likewise, the monoclonal antibody (mAb) RG7155 against CSF1R reduces macrophage infiltration and enhances $CD8^+$ T cell responses in diffuse-type giant cell tumors [115]. In addition to mAbs and inhibitors, a study on hepatocellular carcinoma showed that miR-26a expression downregulates CSF1 and leads to inhibition of TAM recruitment [116]. A recent study showed Luteolin that is a common flavonoid derived from various herbal plants suppresses STAT6 activation and CCL2 secretion triggered by IL4 in TAMs, which leads to reduced recruitment of macrophages to tumors as well as decreased migration of Lewis lung carcinoma cells [117]. Apart from decreasing accumulation of TAMs, targeting CSF1/ CSF1R axis is also capable of repolarizing M2 TAMs to an M1-like phenotype. For instance, in a mouse proneural glioblastoma multiforme model, the CSF1R inhibitor BLZ945 targets TAMs and leads to reduced M2-associated genes such as *arginase 1* and *CD206*, but BLZ945 does not affect the number of TAMs [88].

Interestingly, Wang and Kubes recently proposed a non-vascular route for peritoneal macrophage recruitment, which they referred to as “wormhole migration”, [118]. In this novel paradigm, fully differentiated GATA-binding protein 6^+ macrophages are recruited from the peritoneal cavity to the liver through the mesothelium. However, whether tumor cells similarly induce peritoneal macrophage recruitment and whether this non-vascular macrophage migration can be targeted as a cancer therapeutic strategy require further study.

Table 1 Clinical and experimental therapeutic approaches targeting TAMs		
Mechanism	Target	Strategy
Interference with TAM survival	Legumain	Legumain-based DNA vaccine [106]
	CD204	Anti-204 immunotoxin [107]
	IL4Rα/CD124	RNA aptamer [108]
	CD52	Alemtuzumab▲ [119]
	FRβ	Anti-FRβ mAb [110]
	Cytotoxicity in monocytes	Trabectedin (ET-743)▲ Liposomal clodronate M2pep [103-105]
Inhibition of macrophage recruitment	CCL2/CCR2	Neutralizing antibody CNTO 888 CCL2 inhibitor bindarit CCR2 kinase antagonist PF-04136309▲ Luteolin [84-87,117]
	CSF1/CSF1R	Neutralizing antibody RG7155 CSF-1R inhibitor PLX6134, GW2580 or PLX3397 Liposomal bisphosphonate miR-26a [111,113-115]
Repolarization of M2 TAMs toward an M1-like phenotype	CSF1/CSF1R	CSF-1R inhibitor BLZ945 [88]
	Microenvironmental stimuli	IL12 IFNγ polyl:C bacteria-mediated tumor therapy [58,82,120-124]
	Vascular normalization	Zoledronic acid▲ Histidine-rich glycoprotein Hydrazinocurcumin DMXAA▲ [125-128]
	NF-κB pathway	TLR agonists (polyl:C, CpG-ODN, TLR9 ligand, IL10R mAb) PA-MSHA Flavone glycoside Baicalin CD40 mAb Natural compound corosolic acid [129-134]
	MAPK/ERK pathway	CuNG [135]
	Epigenetic regulation	Overexpressing miR-155/miR-511-3P Deletion of miR-146a [136-139]
	Metabolic regulation	2-deoxyglucose (2-DG) Metformin Rapamycin, RAD001 L-norvaline, CB-1158 Paclitaxel [97]
Nanoparticle and liposome-based drug delivery systems	Engulfed by TAMs and subsequently target cancer cells	Mitoxantrone-loaded SLNs Cisplatin- and cyclodextrin-loaded polymer nanoparticles Albumin nanoparticle–based Abraxane▲ Liposomal Doxil▲ [158,159]
▲Clinically feasible; Adapted from Zheng et al., 2017 and Zheng et al., 2020 [45,97]		

Repolarization of M2 TAMs by manipulation of microenvironment stimuli

As mentioned above, macrophages are functionally plastic because they are induced in response to and modulated by the alteration of molecules in the TME, including cytokines, chemokines, pattern recognition receptors and hormones [54,55]. Therefore, manipulation of environmental stimuli to repolarize M2 TAMs to an antitumoral phenotype under pathological conditions is a potential clinical strategy for cancer therapy. Administration of IL12 to mice bearing hepatocellular carcinoma cell–based tumors alters the functional phenotype of M2 TAMs by downregulation of Stat3 and its downstream transcription factor c-myc, thereby reducing the production of protumoral cytokines and inhibiting tumor growth [124]. TAMs derived from human ovarian cancer ascites are repolarized to an M1-like phenotype, producing less CCL18, MMP9 and VEGF, by being exposed to IFNγ [58]. Furthermore, injection of polyinosinic:polycytidylic acid (polyI:C) into Lewis lung carcinoma tumor–implanted mice to activate the TLR3/Toll–IL1 receptor domain–containing adaptor molecule 1 (TICAM-1) switches protumoral macrophages into tumor suppressors [120]. Intriguingly, apart from cytokine therapy to modify the immunosuppressive microenvironment by boosting T cell–based antitumoral activity, bacteria-mediated tumor therapy has been shown to be a promising strategy [121]. For instance, introduction of attenuated *Listeria monocytogenes* to the TME of ovarian cancer–bearing mice switches M2 TAMs into a tumoricidal phenotype and induces tumor cell lysis through Nos2-dependent production of nitric oxide [82]. Bacillus Calmette-Guérin (BCG) vaccine directed against *Mycobacterium bovis* has also been applied to treat bladder cancer because it enhances the cytotoxic potential of macrophages [122]. Similarly, a recent study demonstrated that heat-killed *Mycobacterium indicus pranii* induces repolarization of TAMs derived from B16F10 tumors toward an antitumoral M1-like phenotype [123].

Abnormal tumor vasculature, which can be caused by M2 TAMs, is one of the key hallmarks of cancer. Abnormal tumor vasculature has detrimental effects on tumor progression because it changes the TME and promotes metastasis. Therefore, vascular normalization is considered as a potential approach for improving antitumoral therapy. The anti-angiogenic effect of zoledronic acid, a clinical agent for inhibition of spontaneous mammary carcinogenesis, is partly due to repolarization of pro-angiogenic M2 TAMs to suppressive M1 TAMs [125]. However, the mechanism of zoledronic acid–induced repolarization has not yet been deciphered. Histidine-rich glycoprotein repolarizes M2 TAMs to enhance antitumoral immune responses and vessel

normalization via downregulation of placental growth factor (PlGF) [126]. Likewise, the STAT3 phosphorylation inhibitor hydrazinocurcumin converts TAMs to an M1-like phenotype to suppress angiogenesis and metastasis in breast cancer[128]. And 5,6-dimethylxanthenone-4-acetic acid (DMXAA) repolarizes M2 TAMs toward an M1-like phenotype which has an effect on mediating the vascular disrupting via STING activation in mouse models of non-small-cell lung cancer [127].

Multiplex immunofluorescence techniques in cancer research

Multiplexed techniques permits comprehensive studies on TME landscape

Conventional immunohistochemistry is limited with a low number of markers can be detected. Multiplexed techniques have emerged to circumvent these constraints, allowing simultaneous detection of multiple markers on a single tissue section and the comprehensive study of complexity of TME.

Among these techniques, multiplex immunofluorescence provides high-throughput staining with retention of spatial context and standardized quantitative analysis for highly reproducible, efficient and cost-effective tissue studies in the era of cancer immunotherapy [140]. For instance, higher frequencies of intraepithelial $CD8^+$ T cell infiltration demonstrates improved survival in several cancer types, such as ovarian cancer [141]. However, $CD8^+$ T-cell infiltration into the tumor beds is related to a poor prognosis in renal cell carcinoma. Multiplex staining facilitates the identification of $CD8^+$ T cell spatial heterogeneity and evaluation of its association with clinical outcome. A high infiltration of $CD8^+CD39^+PD\text{-}1^+$ T-cells at TC in patients with renal cell carcinoma indicates a poor prognosis and $CD8^+$ $CD39^-$ T-cells are recruited more to IM. In addition, immunosuppression under PD-1 blockade can be explained by high proximity between $CD8^+$ $CD39^+PD\text{-}1^+$ T-cells and $Foxp3^+$ $PD\text{-}1^+$ Treg cells [142]. Hence, multiplex staining and imaging enable us to have a deep insight into the immunobiological landscape of TME.

Given that heterogeneity is the most cumbersome nature of cancers, single-cell analysis is essential for understanding the tumor cell and non-tumor cell heterogeneity and their association with prognosis, drug response and drug resistance. Multiplex staining linked with individual cell collection approach, such as laser-capture microdissection, provides a decent platform for genome, transcriptome, epigenome, proteome analyzes at single-cell resolution [143]. Therefore, multiplex staining enables us to generate individual cell inputs from distinct cellular phenotypes of the same specimen for single-cell multiomics

analysis.

Multiplex immunofluorescence platforms

According to different antibody conjugation strategies, there are four classes of multiplex immunofluorescence platform: (i) bright-field based platform (such as Discovery ultra system): after primary antibody incubation, a HRP conjugated-secondary antibody is introduced. The HRP is reacted with a substrate bound to a chromogenic dye, resulting in colored precipitates at the site where the antigens are located. In the Discovery ultra bright field setting, pathologists can assess the staining without any particular software or visualization tool. Nevertheless, it might increase human error for recognizing co-localization of 2-3 markers; (ii) Epitope-targeted mass spectrometry-based platform (such as metal-based techniques, eg. Imaging mass cytometry (IMC)): a primary antibody is tagged with a metal isotope of known molecular mass, which can be further analyzed by mass spectrometry (MS). IMC combines high-resolution laser ablation with mass cytometry for the simultaneous evaluation of more than 100 biomarkers, but the number of slides that can be imaged remains limited; (iii) tyramide-based Vectra platform: after primary antibody incubation, a HRP conjugated-secondary antibody is introduced. Vectra is base on tyramide signal amplification strategy (TSA). Tyramide is a phenolic compound that covalently binds to electron rich moieties of adjacent proteins when activated by enzyme HRP. The primary and secondary antibodies can then be stripped away by heating, while the TSA fluorophore is largely unaffected by heating because it is covalently bound. This makes similar species of antibodies amenable for multiplex staining on the same tissue section without cross-reactivity; (iv) Oligonucleotide-tag based platform (such as Nanostring's digital spatial profiling (DSP) and CO detection by indEXing (CODEX)): the primary antibody is coupled with a photocleavable oligonucleotide tag. Oligonucleotide tags can be cleaved by UV light and collected using a microcapillary tube. The oligonucleotide tags bind to the reporter probe, which can be imaged and counted. The CODEX platform is compatible with the existing three-colored fluorescence microscope, enabling the conversion of a simple fluorescence microscope into a tool for multiparametric imaging and cytometry [140]. Additionally, 3-dimension (3D) Imaging allows for a more detailed reconstruction of the molecular properties. 3D imaging has been used extensively to study dynamic processes in live animals. Nevertheless, conventional 3D imaging using intravital microscopy has limited imaging volume [144]. Newly developed Clearingenhanced 3D (Ce3D) imaging has superior

scanning depth and allows for adequate visualization of large tissue volumes, while preserving the capacity for multiplex antibody staining. However, antibody penetration in thick tissues limits its application [145].

Opal multiplex staining

Opal/Vectra multiplex staining system, which is based on TSA strategy, is the most widely adopted multiplex staining system. It allows the quantitative assessment of variations of protein abundance and spatial context among complex cellular phenotypes. Recently, nine-color multiplex staining using the Opal/Vectra system has been developed to investigate the immune landscape [146]. In reality, there may be little tissue left after routine diagnostic panels for TTF1, Napsin, p63 and cytokeratin for a lung cancer patient. Additional tissue may be used for molecular testing, such as for EGFR mutations and tumor mutational burden. It may be difficult to obtain even one section of useful tissue to image biomarkers such as PD-L1, PD-1, CD68, CD45, CD8 and CD3. Additionally, analyzes of co-localization of mulptiple markers might be beneficial for precision medicine, since multiple marker panels may serve as predictive biomarkers for dichotomizing patients to responders and non-responders to different cancer treatments [147]. Opal/Vectra TSA-based immunofluorescence, images can be acquired using a Vectra pathology imaging system microscope and analyzed using the inForm software (Akoya Bioscience, Menlo Park, California, USA) and the HALO software (Indica Labs, Albuquerque, New Mexico, USA). Of note, other potential analytic pipeline includes Oncotopix (Visionpharm), HistoCAT (Bodenmiller Lab) and Qupath (P. Bankhead and team). Hence, Opal/Vectra multiplex staining system displays a promising utility in personalized cancer immunotherapy.

Aim of study

Macrophages display a high heterogeneity and plasticity in response to different environmental stimuli. In addition to genomic heterogeneity of TAMs, their spatial distribution may be particularly relevant to tumor progression and patient response to treatments [75]. Given that the proximity of immune cells to tumor cells may have profound influence on both cell types as this allows them to interact via soluble factors or cell-cell contact, it is pivotal to recognize that the orchestrated influence of microenvironmental components on cancer is often accompanied by strong spatial differences [148]. *In situ* spatial analyses of TAMs could be linked to lung cancer patient prognosis and treatment outcomes, which will enable us to identify prognostic and predictive biomarkers for responder/non-responder stratification. Thus, the aims of this study are listed as below **(Figure 6)**:

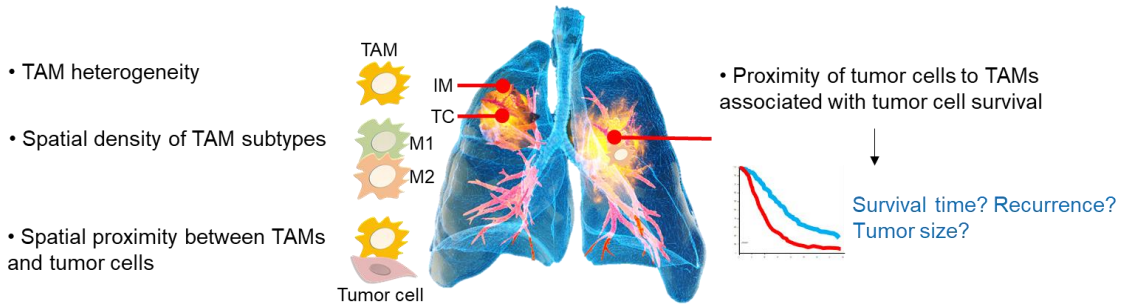

Figure 6 Aims and hypotheses of the study. Spatial density and proximity of TAMs with association with lung cancer survival. IM, invasive margin; TC: tumor center.

1. To understand spatial heterogeneity of TAMs in human lung cancer tissues.
2. To delineate the association of distinct TAM subtype density with overall lung cancer survival.
3. To investigate spatial proximity between TAM subtypes and tumor cells as prognostic biomarker for overall survival of lung cancer.
4. To evaluated the association of proximity of tumor cells to TAMs with tumor cell survival.

Methods

Cell culture methods

Cell culture

Human lung adenocarcinoma cells A549, human umbilical vein endothelial cells (HUVECs) and mouse Lewis lung carcinoma cells LLC1 were obtained from ATCC. A549 cells were cultured in DMEM medium (Gibco) supplemented with 10% fetal calf serum (FCS, Th. Geyer) and 1% penicillin/streptomycin (100 I.U./ml and 100 µg/ml, respectively, Gibco). LLC1 were cultured in RPMI medium (Gibco) supplemented with 10% FCS and 1% penicillin/streptomycin. HUVECS were cultured in endothelial cell growth medium (Sigma-Aldrich) supplemented with 10% FCS and 1% penicillin/streptomycin. All cells were cultured at 37 °C with 5% CO_2 (HERAcell 150i, Thermo Fisher Scientific).

When cells reach 80-90% confluence, they were subcultured and split in a ratio of 1:3 to 1:6 depending on the density needed and cell type. Medium was aspirated, and cells were washed with 1x phosphate buffered saline (1x PBS, Gibco® by Life Technologies) and incubated with 1x trypsin solution (Thermo Fisher Scientific) for 3-5 minutes at 37 °C until cells detached. To stop the trypsin activity, media with FCS or FCS alone was added to the cells and the cell suspension was collected and centrifuged at 300 g for 5 minutes. Cell pellet was then resuspended in fresh medium and cells were plated at the desired ratio. For freezing purposes, cells were trypsinized and cell pellet was resuspended in freezing medium containing 10% dimethylsulfoxide (DMSO, Sigma-Aldrich) and 20% FCS. Cells were frozen in cryovials and stored in liquid nitrogen tank until further use. The cell line was authenticated by the manufacturer and checked for mycoplasma, using LookOut® Mycoplasma PCR Detection Kit (Sigma-Aldrich).

Isolation of human peripheral blood monocyte-derived macrophages

Buffy coats obtained from the blood bank of the Universities of Giessen and Marburg Lung Center Peripheral blood monocytes were isolated from human buffy coats by using Ficoll (GE Healthcare) by means of density gradient centrifugation. Each Leucosep™ Centrifuge Tube (Greiner Bio-One) was firstly filled with 15 mL Ficoll and then centrifuged at 500 g for 1 minute. After each tube being layered with 35 mL blood, centrifugation was performed at 440 g for 35 minutes at 20 °C in a swinging-bucket rotor

without brake. Next, the interphase mononuclear cell layer was transferred to a new 50 mL tube. For removal of platelets, cell pellet was resuspended in 50 mL PBS and centrifuged at 200 g for 10–15 minutes at 20 °C. Then cell pellet was resuspended in RPMI medium and 1% penicillin/streptomycin and seeded to Poly-D-Lysine culture dishes (Thermo Fisher Scientific). After one hour, medium was replaced with RPMI medium supplemented with 2% human serum (Blood bank of the Universities of Giessen) and 1% penicillin/streptomycin. Cells were cultured for 10 days with replacing with fresh medium every other day until generation of undifferentiated macrophages. M1 macrophages were polarized by 100 ng/mL Lipopolysaccharide (LPS, Sigma-Aldrich) and 100U/mL Interferon-γ (rhIFNγ, R&D Systems) and M2 by 20 ng/mL rhIL4 (R&D Systems) for 24 hours [149].

Generation of mouse bone-marrow derived macrophages

Bone marrow from the femur and tibia of five to seven-week old mice (The Jackson Laboratory) were isolated, erythrocyte-depleted and cultured in RPMI medium supplemented with L-glutamine, 10% FCS and 1% penicillin/streptomycin in the presence of 20 ng/mL recombinant murine macrophage stimulating factor (rmM-CSF, R&D Systems). Medium change was performed every other day for 5 days to allow differentiation and maturation of macrophages. Sequentially, cells were applied to coculture experiment or stimulated with cytokines. M1 macrophages were polarized by 100 ng/mL Lipopolysaccharide (LPS, Sigma-Aldrich) and 100 U/mL Interferon-γ (rmIfnγ, R&D Systems) and M2 by 20 ng/mL rmIl4 (R&D Systems). Polarized macrophages were harvested for isolation of RNA and protein or *in vivo* injection.

Functional assays for cells

Proliferation assay

Proliferation of cells was determined using colorimetric cell proliferation ELISA BrdU kit (Roche) according to the manufacturer's protocol. A549 Cells were seeded as 4-8 replicas in 96-well plate at a density of $5x10^3$ cells/well in 100 µL full medium and cultured overnight. Medium was then removed and cells were serum starved in medium without serum supplementation. After 24 hours of serum starvation, the medium was replaced with medium to be tested and cells were cultured for 24 hours. Additional controls were performed with medium containing 0% and 10% FCS. BrdU was then

added to the cells for 2 hours in serum-free medium. Cells were then fixed and BrdU incorporated in proliferating cells was detected with antibody having horse radish peroxidase (HRP) conjugation. An HRP-substrate was added and the color developed was measured spectrophotometrically at 370 nm with reference measurement at 492 nm using Tecan Infinite M200 PRO reader (Tecan Group Ltd).

Migration assay

For the evaluation of the migratory capacity, the Boyden chamber migration assay was performed. A volume of 700 µL of conditioned medium was distributed with triplicates into the wells of 24-well companion plates (BD BioSciences). Cells were seeded on filters (8.0 µm pore size; BD Falcon cell culture insert, transparent PET membrane, Corning, Inc.) at a density of 5×10^4 cells per filter in 300 µL serum-free medium. Additional controls were performed with medium containing 0% and 10% FCS. A549 Cells were incubated for 6 hours in the incubator at 37 °C with 5% CO_2. Sequentially, the filters were washed with PBS and dried from the inner side with a cotton swab to remove non-migrated cells and fixed in methanol (Roth) for 3 minutes, followed by being stained for 10 minutes with Crystal Violet solution (Sigma-Aldrich). After the final wash in ddH_2O, filters were dried, cut out from the inserts and mounted on slides with Pertex (Medite GmbH). Slides were scanned with Nanozoomer 2.0HT digital slide scanner C9600 (Hamamatsu Photonics) and the migrated cells per membrane were counted using ImageJ software.

Cell death assay

Apoptosis was assessed using Cell Death Detection ELISAPLUS (Roche Applied Science. The assay is based on a quantitative sandwich-enzyme-immunoassay-principle that allows the specific determination of mono- and oligonucleosomes in the cytoplasmatic fraction of cell lysates. Since the apoptotic cells maintain the membrane integrity while necrotic cell lose the membrane integrity, after centrifugation with 200 g, supernatant can be applied to analyze necrosis and cell pellet was collected to analyze apoptosis. In addition, ICC staining of cleaved caspase-3 was performed to test apoptosis. $1x10^4$ adherent cells were applied to extract cytoplasmic histone/DNA fragments by adding 200 µL lysis buffer and then incubated in microtiter plate modules that were coated

with anti-histone antibody. Sequentially, immobilized histone/DNA fragments were detected by peroxidase-conjugated antibody and a color was developed with an ABTS (2, 2'-azino-bis (3-ethylbenzothiazoline-6-sulphonic acid) substrate, which was read at 405 nm with reference measurement at 490nm using Tecan Infinite M200 PRO reader (Tecan Group Ltd).

Tube formation assay

200 µL of growth factor-reduced Matrigel (BD Biosciences) was pipetted into a well of a 24-well culture plate and polymerized for 30 minutes at 37 °C. Then, early passage HUVECs (no more than passage 5; 1×10^4 cells/well) were seeded onto polymerized Matrigel and incubated with endothelial cell growth medium (Sigma-Aldrich) supplemented with 2% FCS for 2 hours to allow cells to attach, followed by replacing supernatant with medium to be tested. Additional controls were performed with endothelial cell growth medium containing 0% and 10% FCS. After 6 hours of incubation under standard conditions tube formation was evaluated in microphotographs taken under 100x magnification in phase-contrast mode. Length of formed tubes were counted using ImageJ software in 5 random field of view taken from each plate well.

Molecular biology and biochemical methods

RNA isolation

Cells or tissues were resuspended in Trizol (Thermo Fisher Scientific) and vortexed for 1 minute (tissue samples were then centrifuged at 12000 g for 30 minutes at 4 °C). Next, 0.2 mL chloroform (Sigma-Aldrich)/ml Trizol was added to the supernatant and mixed vigorously, and then incubated for 10 minutes at room temperature and centrifuged at 12000 g for 15 minutes at 4 °C. The upper aqueous layer was transferred to another tube and overlaid with 500 µL isopropanol/ml Trizol. After gentle mixing, mixture was incubated for 10 minutes at room temperature and then centrifuged at 12000 g for 10 minutes at 4 °C to collect the precipitated RNA. The supernatant was then removed and the pellet was washed twice with 75% ethanol and then left to dry. The isolated RNA was then resuspended in an appropriate amount of Nuclease-free water and the concentration and purity of RNA were measured using NanoDrop (Peqlab Biotechnologies GmbH). After checking the integrity of RNA on 1% agarose gels, RNA was stored at -80 °C until

further use. Regarding RNA samples for RNA-sequencing, total RNA from the macrophages was isolated using RNeasy Micro Kit (Qiagen) and the RNA quality and quantity were assessed using Labchip GX touch (PerkinElmer).

Reverse transcription for cDNA synthesis

RNA was pre-treated with DNase (Fermentas) to eliminate possible contamination with genomic DNA. The RNA concentration was adjusted to 100 ng/μL and 1000 ng of RNA in total were used per sample. RNA was transcribed to cDNA using High Capacity cDNA Reverse Transcription Kits (Applied Biosystems). RT master mix was prepared on ice as described in **Table 2**. 10 μL RT master mix was then added to each sample, followed by being loaded to thermal cycler (**Table 3**). The synthesized cDNA was diluted 1:3 before proceeding with qPCR.

Table 2 Reaction mixture for qPCR

Component	Volume
Nuclease-free water	2.0 μL
10X RT Buffer	3.7 μL
25XdNTP Mix	0.8 μL
10XRT Radom Primers	2.0 μL
RT	1.0 μL
Rnase Inhibitor	0.5 μL
Total	10.0 μL

Table 3 Thermal cycling condition

Settings	Step 1	Step 2	Step 3	Step 4
Temperature	25°C	37°C	85°C	4°C
Time	10 minutes	120 minutes	5 minutes	-

Quantitative real time polymerase chain reaction (qRT-PCR)

The Real Time-qPCR reaction mixture was prepared using Applied Biosystems™ PowerUp™ SYBR™ Green Master Mix as described in **Table 4**. qRT-PCR primers were designed using the NCBI tool Primer-BLAST. Gene bank accession numbers of the gene sequences were obtained in Pubmed gene database. Primers were designed according to standard PCR guidelines: the amplicon length was approximately 50–200 bp; primers should be about 18–24 nucleotides in length and specific for the target sequence, and be free of internal secondary structure; primers should avoid stretches of

homopolymer sequences (e.g., poly (dG)) or repeating motifs, as these can hybridize inappropriately. Primer pairs should have compatible melting temperatures (within 5 °C) and contain approximately 50% GC content. **Table 5** and **Table 6** list all primers used, as well as their sequences and the corresponding annealing temperature. Master mixture and cDNA template were pipetted into non-skirted 96-well plates and the reaction was run in Applied Biosystems StepOne Real-time PCR using following reaction conditions: 10 minutes at 95 °C following 40 cycles of 15 seconds at 95 °C and 1 minute at 60 °C. For each qRT-PCR run, a no template control (NTC) omits any cDNA template from a reaction was set as a technical control for extraneous nucleic acid contamination. To evaluate the PCR efficiency and specificity, the efficiency of a PCR reaction and the melt curve was analyzed. The single peak for an amplicon and the reaction with serial diluted template had an efficiency between 90% and 110% was observed to guarantee a decent reaction (**Figure 7**). A PCR efficiency was determined by the following equation: Efficiency = $10^{(-1/\text{slope})}/2$ *100%. Data were analyzed with the StepOne Software v2.3 and normalized to the expression of housekeeping gene hypoxanthine phosphoribosyltransferase1 (*HPRT*). And the level of mRNA expression was represented as either ΔCt values (Ct value of the housekeeping gene – Ct value of the gene of interest) or $2^{-\Delta\Delta Ct}$ values.

Table 4 Reaction conditions for qPCR program

Component	Volume (μL)
Applied Biosystems™ PowerUp™ SYBR™ Green Master Mix	5
Forward primer (10 mM)	0.25
Reverse primer (10 mM)	0.25
Nuclease-free water	3.5
cDNA template	1
Total	10

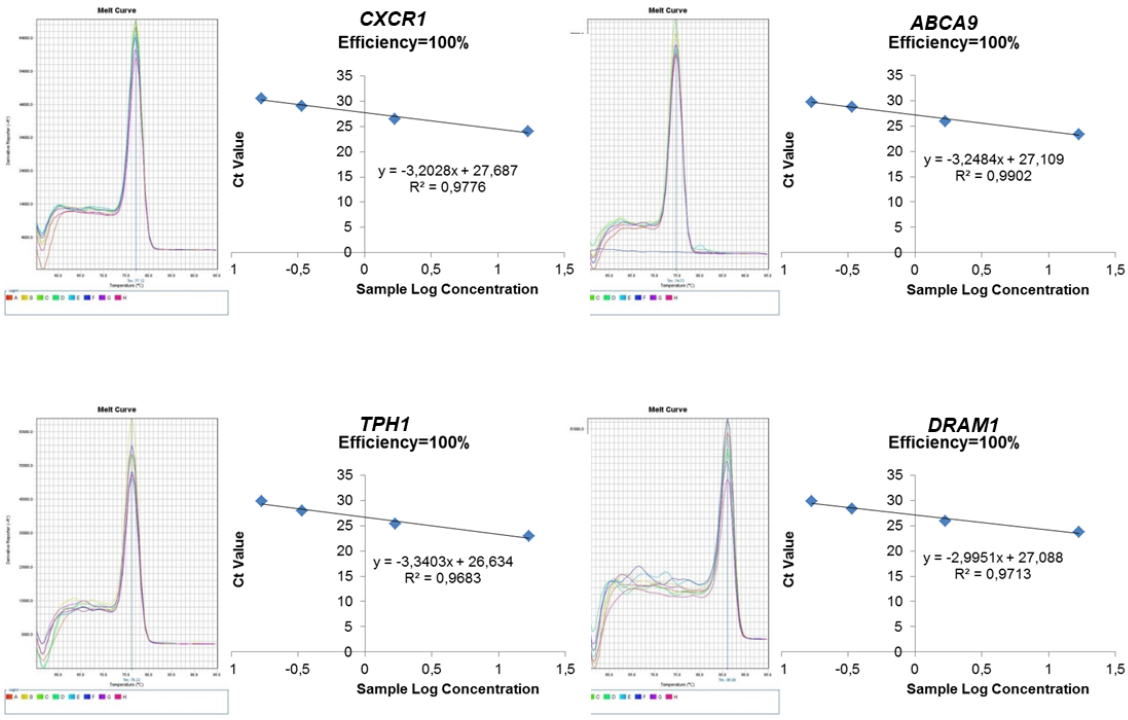

Figure 7 Melt curves and PCR efficiency. Examples of melt curves and PCR efficiency of four genes detected with human macrophage samples.

Table 5 List of primers used for quantitative real time PCR (homo sapiens)

Gene	Accession number	Primer Sequence (5'-3')		Annealing temperature
ABCA9	NM_080283.4	FP	AGCTTTCCTGAGAGAAACAGG	58
		RP	GTTCTTGCAGAGAAGAGCCC	
ACTR6	NM_022496.5	FP	GCCATGAAAATGTGTCGGTT	58
		RP	GCTGTTTTTGACCGGAACTG	
ACVR1C	NM_145259.3	FP	GCAAATTCATCAGGCGAAGG	58
		RP	GACATACACACTTCAGTCCTGG	
ADIPOR1	NM_015999.6	FP	ATGTAGCGCGGGGGAC	58
		RP	CCCTCTGATGGTAGACAAGCC	
ALOX15	NM_001140.5	FP	CTTCAAGCTTATAATTCCCCAC	58
		RP	GATTCCTTCCACATACCGATAG	
ANAPC4	NM_013367.3	FP	CCCGAGCTGAATAAGGTAATGA	58
		RP	GTGTTAGGGGGTGACACAAG	
AP1S3	NM_001039569.2	FP	GCCCAGCCACGATGATAC	58
		RP	AAACTGCTTGTCCTGTGACC	
ARG2	NM_001172.4	FP	GACAAGCAACAAACCCTTGATG	58
		RP	AGGACAAACTGCTCTGCCAATT	
BCL2L1	NM_138578.3	FP	CTGGTGCTTTCGATTTGACTTA	58
		RP	TAAGATTCAGAACTGGTTTCTTTGT	
BNIP3L	NM_004331.3	FP	GATGTGCAGTTGTTTCTGCTC	58
		RP	CAGGAACCTTGTGAACTTGTCTTT	
C5/C5a	NM_001735.3	FP	ATGACGACTTGAAGCCAGCC	58

		RP	CTACCATGTCAACTTCTGATCC	
CCL18	NM_002988.4	FP	AAGCCAGGTGTCATCCTCCT	58
		RP	CAGCTTCAGGTCGCTGATGT	
CCL19	NM_006274.3	FP	TGGGTACATCGTGAGGAACT	58
		RP	GTGTGGTGAACACTACAGCA	
CCL20	NM_004591.3	FP	CCATGTGCTGTACCAAGAGT	58
		RP	AAGTTGCTTGCTTCTGATTCG	
CCR7	NM_001838.4	FP	GCTGGTGGTGGCTCTCCTT	58
		RP	GTAATCGTCCGTGACCTCATCTT	
CD163	NM_203416.4	FP	AGCATGGAAGCGGTCTCTGTGATT	58
		RP	AGCTGACTCATTCCCACGACAAGA	
CDKN2C	NM_078626.3	FP	CGACTAATTCATCTTTTCCTGATCG	58
		RP	GATTTCCAAGTTTCATAACCTGC	
CFD	NM_001928.4	FP	TGCTACAGCTGTCGGAGAA	58
		RP	ATCAAGCGCTCGGTGATG	
CFH	NM_000186.4	FP	AAAGCGCAGACCACAGTTAC	58
		RP	AGGGTAAAGCTGACACGGAT	
CHMP3	NM_016079.4	FP	GTTGGGACTACCTCCTTTTCC	58
		RP	ATGACCACTCATTGACCAGTT	
CPD	NM_001304.5	FP	GGGCAGAATGGCTAATGGTC	58
		RP	TTTCCAGAAAGCACAAACCTCA	
Cripto-1	NM_003212.4	FP	TGTAAATGCTGGCACGGTCA	58
		RP	AGGCAGATGCCAACTAGCATAA	
CRP	M11725.1	FP	GTGTTTCCCAAAGAGTCGGATA	58
		RP	CCACGGGTCGAGGACAGTT	
CSF1R	NM_005211.4	FP	GAGAGCTATGAGGGCAACAG	58
		RP	TCCGAGGGTCTTACCAAACT	
CTSD	NM_001909.5	FP	AGGGCGAGTACATGATCCC	58
		RP	ACCTTGAGCGTGTAGTCCTC	
CXCL10	NM_001565.4	FP	GCACCATGAATCAAACTGCC	58
		RP	GGTACTCCTTGAATGCCACT	
CXCL12	NM_199168.4	FP	TGCCCTTCAGATTGTAGCC	58
		RP	CGGAAAGTCCTTTTTGGCTG	
CXCL3	NM_002090.3	FP	GATACTGAACAAGGGGAGCAC	58
		RP	ATTTTCAGCTCTGGTAAGGGC	
CXCR1	NM_000634.3	FP	TCAAGTGCCCTCTAGCTGTT	58
		RP	GTTTGATCTAACTGAAGCACCG	
DBF4	NM_006716.4	FP	AAAGGACATTTCCAGGGTGG	58
		RP	TTCTTCAACTCGATTTGGATTTTTC	
DCAF7	NM_005828.5	FP	CACCTTTGACCACCCATACC	58
		RP	GTCTCTGTTTCACCAACCCTC	
DESI2	NM_016076.5	FP	GGCAGAGAATTTGCTTATGGTG	58
		RP	TCCGTGCTCCCTAAAACAAC	
DRAM1	NM_018370.3	FP	GCTGTCATCCCCATGATTGT	58
		RP	CTGTCCATTCACAGATCGCA	
E2F8	NM_024680.4	FP	CGTGTGTGTAAGGGGAGAAA	58
		RP	AAGTTTTAATATCCTGTTCGCAGAT	
ERAP2	NM_022350.5	FP	TTCATCAGGGGTCAAGGTGT	58

		RP	TTGATTCCGTTTGTCTGGGG	
FAM199X	NM_207318.4	FP	ACCAACAGGTGGAACCTAAC	58
		RP	CTTCTGAGCTGGCAACACTT	
FCGR3A	NM_000569.8	FP	AAGGAAATTGGTGGGTGACA	58
		RP	ATGCCAGCTGAAACTAGAAGT	
FCN1	NM_002003.5	FP	CTGCTAGACCGGGGGTATT	58
		RP	TCCGCTGGAAAACGGTCC	
GET4	NM_015949.3	FP	GCCGTGCTACAGTTTCTCTG	58
		RP	CTTCTGGGTGTACGTCGTG	
GPX1	NM_201397.3	FP	GGGGCAAGGTACTACTTATCG	58
		RP	TTCTTGGCGTTCTCCTGATG	
GYG1	NM_004130.4	FP	CACCAACGTTTTACCTCTGC	58
		RP	ATAGACCAAGTCTGAAAGCACA	
HABP4	NM_014282.4	FP	GAGTCTCCAGCCAAAGTTCC	58
		RP	ACAGTGGATTCTGGTTTCCG	
HAMP	NM_021175.4	FP	TTTCCCACAACAGACGGG	58
		RP	GCAGGTAGGTTCTACGTCTTG	
HIVEP1	NM_002114.4	FP	TGAGCGAGAGTCTGCCTTAG	58
		RP	GTGCTTCTTCAATTTTGTCAGC	
HLA-DRA	NM_019111.5	FP	CTGGCGGCTTGAAGAATTTG	58
		RP	GGAGGTACATTGGTGATCGG	
HMGA1	NM_145899.3	FP	CGCTGGTAGGGAGTCAGAAG	58
		RP	GGTGGTTTTCCGGGTCTTG	
HPRT	NM_000194.3	FP	TGACACTGGCAAAACAATGCA	58
		RP	GGTCCTTTTCACCAGCAAGCT	
IER3	NM_003897.4	FP	ATCTTCACCTTCGACCCTCT	58
		RP	GGCGCCGGACCACTC	
IL10	NM_000572.3	FP	CAAGCTGAGAACCAAGACCC	58
		RP	ACAGGGAAGAAATCGATGACAG	
IL12B	NM_002187.3	FP	GCCCAGAGCAAGATGTGTCA	58
		RP	CACCATTTCTCCAGGGGCAT	
IL17A	NM_002190.3	FP	AATCTCCACCGAATGAGCA	58
		RP	ACGTTCCCATCAGCGTTG	
IL19	NM_153758.5	FP	AAATCAGCAGCATTGCCAAC	58
		RP	ACTGCCTCTGTTCCTGACAT	
IL1B	NM_000576.3	FP	AGAAACTGGCAGATACCAAACC	58
		RP	TGGAAGGAGCACTTCATCTGT	
IL1ra	NM_173843.3	FP	CTGCAGTCACAGAATGGAAATC	58
		RP	CAACTAGTTGGTTGTTCCTCC	
IL22	NM_020525.5	FP	ACAAGTCCAACTTCCAGCAG	58
		RP	GCGCTCACTCATACTGACTC	
IL23A	NM_016584.3	FP	AGGCAAAAAGATGCTGGGGA	58
		RP	TCCTTTGCAAGCAGAACTGAC	
IL5	NM_000879.3	FP	ACCTTGGCACTGCTTTCTAC	58
		RP	CAGTGCACAGTTGGTGATTTT	
IL8	NM_000584.4	FP	ACAGCAGAGCACACAAGCTTC	58
		RP	ATCAGGAAGGCTGCCAAGAG	
IQGAP2	NM_006633.5	FP	AGCAGACAGCAACTTTAGCA	58

		RP	CCCTACAGCTACAACTCCTTT	
IST1	NM_014761.4	FP	TGAACCCTGAAGTCGGTGTC	58
		RP	ATCAGCAACCTAACCGAATCCT	
KMT2C	NM_170606.3	FP	GATACGGCCGAAATCCTCTC	58
		RP	GTGAGGCCTTAACACAAACC	
Leptin	NM_000230.3	FP	CATTTCACACACGCAGTCAG	58
		RP	TCTGGAAGGCATACTGGTGA	
LIF	NM_002309.5	FP	CCGGCTAAATATAGCTGTTTCTG	58
		RP	CCTGGGCTGTGTAATAGAGAATAA	
LILRB2	NM_005874.5	FP	GACATCGAGTCCAGCCCAG	58
		RP	CTTCAGGCTGTGTGTCCTTC	
LMNA	NM_170707.4	FP	CAGCATCATACAAGAGATGGGA	58
		RP	CTAGGGAAGGCAGCTCAAAC	
LRRFIP2	NM_006309.4	FP	ACCATCACTAAGGGCTGAAAA	58
		RP	TCGGTCTTTCACAGGTGTTC	
LST1	NM_205839.3	FP	TCGCCTAAAAGAGCAAGGAC	58
		RP	AGCCTCTTTACATCATTCCGC	
MED16	NM_005481.3	FP	CCGAAATCTCATCGCCTTCA	58
		RP	CGGGAGCCTGACTGGT	
METAP2	NM_006838.4	FP	ATGATGAAGCAAAAGTTCAAACAG	58
		RP	TCGCATTCTTGTCCTTTGGG	
MFSD12	NM_174983.5	FP	CGCTACGGCACCGTCT	58
		RP	AGCCAAACTGGAAGATCACG	
MMP9	NM_004994.3	FP	GTACCACGGCCAACTACGACA	58
		RP	TGGTGCAGGCGGAGTAGGATT	
MPO	M19507.1	FP	GGATAAGAGAGCAGTGAGCC	58
		RP	CTGCTTGATGCTTTCCCGC	
NTS	NM_006183.5	FP	GGCTTTTCAACACTGGGAGTTAAT	58
		RP	TCTCATACAGCTGCCGTTTCAG	
PACS2	NM_015197.4	FP	CGGAGCCAGCTACAGATCC	58
		RP	GATGTGGTTGAGCTGGTCAT	
PAG1	NM_018440.4	FP	AGCCTTAGAAGACGTTCATGTT	58
		RP	CCAGGGTGCCTCCTACAAT	
PAQR4	NM_152341.5	FP	TCAGGCGTCCGGGCT	58
		RP	TGGTGGCACATAAAGAGGTGA	
PIH1D1	NM_017916.3	FP	CTGCAGGCCTCGAAGGAG	58
		RP	TATGCAGAAACCAGGCTGAGG	
PLOD1	NM_000302.4	FP	CCGGAGGACAACCTTTTAGT	58
		RP	CACATTCCAGTCCTCCCCTA	
PMP22	NM_153321.3	FP	TTGGAAGAAGGGGTTACGCT	58
		RP	CACGATCCATTGGCTGACG	
PTGS2	NM_000963.4	FP	CTGGCGCTCAGCCATACAG	58
		RP	CGCACTTATACTGGTCAAATCCC	
PUS7L	NM_031292.5	FP	TAGTGCAGGGTGATTTGGTC	58
		RP	AGTACTGGAAGAACCACCTGA	
RBP4	NM_006744.4	FP	GTGCTGACAGCTACTCCTTC	58
		RP	CAGTAACCGTTGTGGACGAT	
RBP4	NM_006744.4	FP	GCTTGCGCGCGGTTCC	58

		RP	CCCAGAGAAGCGAGCCTTGT	
Relaxin-2	NM_134441.3	FP	TGCTCCTCAGACACCTAGAC	58
		RP	ACAATTTGGAAAGGGCACCA	
Resistin	NM_020415.4	FP	CCACCGAGAGGGATGAAAG	58
		RP	GGATCCTCTCATTGATGGCTT	
SDF4	NM_016176.6	FP	CTCAAAGTGGATGAGGAAAGACAT	58
		RP	AGTCCCAAAGGTAGACGGAG	
SEC61A1	NM_013336.4	FP	GTCATCTATTTCCAGGGCTTC	58
		RP	AGCTTGATGGGATAGGTGTTG	
Serpin E1	NM_000602.5	FP	TCAGGAAGCCCCTAGAGAAC	58
		RP	GGCTCTTGGTCTGAAAGACT	
SERPINB9	NM_004155.6	FP	ATAAACCAGGAGGAGCAAAGG	58
		RP	AACGTGGCCTCCTGATACAT	
SMPD1	NM_000543.5	FP	ACCGAATTGTAGCCAGGTATG	58
		RP	TTTGGTACACACGGTAACCAG	
SMPD1	NM_000543.5	FP	GGAAGGGAAAAGAAAGAATTGGGG	58
		RP	AGAGCCAGAAGTTCTCACGG	
SMTNL1	NM_001105565.3	FP	TTCTCCACAGCAGAGAAACTG	58
		RP	ATGTGTAGACGCACTTGGAG	
SPATA2	NM_006038.4	FP	ACACTTTCGAGTAGAGCTGTC	58
		RP	AGCGGAGTGCTCCTAAGTC	
SPP1	NM_000582.3	FP	TGCAGTGATTTGCTTTTGCC	58
		RP	AGGTACATCTTTAGTGCTGCTT	
STK38L	NM_015000.4	FP	TGCCTAGGGGCAGAAGAAAT	58
		RP	CGCACCTCTTCATCTGCTAA	
TFF3	NM_003226.4	FP	CTGCAGGAAGCAGAATGCAC	58
		RP	TCTCAGGCACGAAGAACTGT	
TFR	NM_003234.4	FP	TGCAGCACGTCGCTTATATT	58
		RP	TCATTCAGCAGCTTGATGGT	
TM2D3	NM_078474.3	FP	AATAAAGGATCCGGGCCCAA	58
		RP	TTTCAGTACTTTCTGCTGCCC	
TMEM189	NM_145538.2	FP	TTGCTGACTTCTTGTCTGGC	58
		RP	TGAAAGCCTTCCCCACAATGG	
TNFRSF1A	NM_001065.4	FP	CTGCCACTGGAACCTACTTG	58
		RP	CCTGACCCATTTCCTTTCGG	
TNFRSF8	NM_001243.5	FP	TTATGGCTCTCCTAATTCCTGC	58
		RP	ACAAGCACTATATGAGCACCG	
TNFα	NM_000594.4	FP	GAGGCCAAGCCCTGGTATG	58
		RP	CGGGCCGATTGATCTCAGC	
TPCN1	NM_017901.6	FP	GAGCTCTTTCCCATGGTGTG	58
		RP	ATAGCTGCCGCCATAAAGC	
TPH1	NM_004179.3	FP	TAGGTCATGTCCCGCTTTTG	58
		RP	AGTAGCACGTTGCCAGTTTT	
TRUB2	NM_015679.3	FP	AAGGATTACACAGTGCGTGG	58
		RP	GGTCACGTGGTCATAGGTTG	
UBR2	NM_015255.3	FP	TAGATCGAGATGGGCGTAGG	58
		RP	GTGCGACAATAGACGAATGC	
UBTD1	NM_024954.5	FP	AAGCGAGCAGGACGCAA	58

		RP	CAGAACTCATCCCGTTTGCT	
UBXN4	NM_014607.4	FP	AGCCTGCCTACAGTTTTCAC	58
		RP	AATGCATCTGTCGGACCTTG	
VEGF	NM_003376.6	FP	AGGGCAGAATCATCACGAAGT	58
		RP	GGTCTCGATTGGATGGCAGTA	
VIM	NM_003380.5	FP	ACAAATCCAAGTTTGCTGACC	58
		RP	TACTCAGTGGACTCCTGCTT	
WARS	NM_011710.3	FP	AGCTCATTGTTCGGTTTGGA	58
		RP	CGGCCCGTGTACAGATAAAA	
ZC3H13	NM_015070.6	FP	AGTCTGGAAGCAGGAGATGA	58
		RP	TGCATCACCTGCCAGAATTT	
ZMAT1	NM_001394560.1	FP	TGACCTTACTCTACAAACACGA	58
		RP	GTTCTCATACTAAATGCTGTGGG	
ZNF222	NM_013360.3	FP	TTTCCACATCTTGCGAGTCC	58
		RP	TTTAGAAAGGTCGGGCTCTG	
ZNF37A	NM_003421.4	FP	GAACAGACAGAGTCGCTTGA	58
		RP	ACTGTGAGGGTGTAGTCTGT	
ZNF581	NM_016535.4	FP	CTGCTGCACTGGGCCT	58
		RP	AACGGAGGAAAATGCCAGAG	

Table 6 of primers used for quantitative real time PCR (Mus musculus)

Gene	Accession number	Primer Sequence (5'-3')		Annealing temperature
Alox15	NM_009660.3	FP	TTCCGTGCACCCTGTTTTTA	58
		RP	CTGTGCTCATCACCTTGTCA	
Arginase	NM_007482.3	FP	TACAAGACAGGGCTCCTTTCAG	59
		RP	GCAAGCCAAGGTTAAAGCCA	
Chitinase	NM_023186.3	FP	GAGTGCTGATCTCAATGTGGATT	59
		RP	GGGTCACTCAGGGTAAAGGT	
Hprt	NM_013556.2	FP	GCTGACCTGCTGGATTACAT	58
		RP	TTGGGGCTGTACTGCTTAAC	
Il10	NM_010548.2	FP	ACATACTGCTAACCGACTCCT	58
		RP	AAATCGATGACAGCGCCTC	
Il12b	NM_002187.3	FP	AGCACGGCAGCAGAATAAAT	58
		RP	GTCTGGTTTGATGATGTCCCT	
Il1b	NM_008361.4	FP	TGCCACCTTTTGACAGTGATG	59
		RP	TGCTGCGAGATTTGAAGCTG	
iNOS	NM_010927.4	FP	ACTACTACCAGATCGAGCCC	58
		RP	GCTAGTGCTTCAGACTTCCC	
Tnfα	NM_013693.3	FP	CATCTTCTCAAAATTCGAGTGACAA	60
		RP	TGGGAGTAGACAAGGTACAACCC	

Human specimens

Tumor tissue specimens, which from TC and IM as well as the adjacent non-tumor based on the histopathologic review, were collected from patients with lung squamous cell carcinoma at the time of surgery before chemotherapy after obtaining informed consent

at the University Hospital Giessen in Germany (reference AZ 58/15). The three specimens used for RNA sequencing (RNA-seq) analysis were obtained from male patients, aged 76, 75, and 60 years, with tumor stages II, IV, and IV, respectively. The four specimens used for quantitative real-time polymerase chain reaction (qRT-PCR detection) were obtained from two males and two females, aged 60, 67, 73, and 74 years, with tumor stages IV, II, II, and II, respectively. Of note, IM is defined as a region centered on the border separating the host tissue from malignant areas, with an extent of 1 mm [73,150,151]. The specimens were placed immediately in ice-cold RPMI 1640 medium (Gibco) containing 100 μg/mL cycloheximide. Single-cell suspensions were prepared using the Human Tumor Dissociation kit (Miltenyi Biotec). Briefly, tissues were mechanically dissociated in the gentleMACS Dissociator for 30 seconds and incubated in digestion buffer at 37°C for 15 minutes. The samples were dissociated a second time for 30 seconds, and the resulting single-cell suspensions were filtered through 70-μm cell strainers (BD Biosciences), followed by erythrocyte depletion and centrifugation at 500 *g* for 5 minutes at 4 °C.

Flow cytometry and cell sorting

The cell pellets were resuspended in phosphate-buffered saline (PBS) and filtered through 40-μm cell strainers (BD Biosciences). After blocking FcγR using diluted serum for 15 minutes, the human single cells were stained for 15 minutes at 4 °C with the following antibodies: CD1c-PE/Dazzle594 (Biolegend, 331531), CD15-FITC (BD, 560997), CD33-BV510 (BD, 563257), CD45-AF700 (Biolegend, 368514), CD326-FITC (Biolegend, 324203), HLA-DR-APC/Fire750 (Biolegend, 307658), MerTK-BV421 (Biolegend, 367603), CD14 PerCP-Cy5.5 (BD, 561116), and CD64 BV605 (BD, 740406) [61]. All antibodies and secondary reagents were titrated to determine optimal concentrations. Comp-Beads (BD Biosciences) were used for single-color compensation to create multicolor compensation matrices. Isotype control was used to determine the level of background surface staining and fluorescence minus one control (FMO) was used for gating. We controlled instrument calibration daily using Cytometer Setup and Tracking beads (BD Biosciences). Flow cytometry-based cell sorting was performed using a BD FACSAria™ III fluorescence-activated cell sorter. The sorting strategy involved the exclusion of debris and cell doublets based on light scattering, and cell viability was assessed using 7-aminoactinomycin D (BD Biosciences).

RNA sequencing

RNA-seq library preparation and sequencing were conducted at the Max Planck Institute for Heart and Lung Research. Libraries were constructed using approximately 2 ng total RNA as input for the SMARTer® Stranded Total RNA-Seq kit (Pico Input Mammalian; Takara Clontech). Sequencing was performed using an Illumina NextSeq500 instrument using v2 chemistry, resulting in a minimum of 36 million reads per library with a 75-bp single-end setup. High-quality reads were aligned to Ensembl human genome version hg38 (GRCh38) using the RNA-seq aligner STAR 2.4.0a with the parameter "outFilterMismatchNoverLmax 0.1" to maximize the ratio of mismatches to the mapped length to 10% [152]. The number of reads aligning to genes was counted with featureCounts 1.4.5-p1 using the Subread package [153]. Only reads mapping at least partially inside exons were retained and aggregated per gene, while reads overlapping multiple genes or aligning to multiple regions were excluded. DESeq2 was used to estimate fold changes in expression and dispersion of mRNAs identified in the RNA-seq data [154]. The resulting *P* values were adjusted for multiple testing with the Benjamini-Hochberg method to yield adjusted *P* values. The RNA-seq data were deposited in the Gene Expression Omnibus archive (accession number GSE137343). For preparation of heatmaps, a count matrix representing all transcripts identified by RNA-seq was prepared for the macrophage samples from paired adjacent non-tumor tissues and TC and IM samples. The mean log2 fold change was calculated for each transcript, and the false discovery rate (FDR, probability of incorrectly accepting a difference among the macrophages from the non-tumor, TC, and IM tissues) for each transcript was calculated according to Storey's method. Genes with a FDR less than 0.05 were considered to be differentially expressed.

Western blot

Cells were lysed in RIPA buffer (Santa Cruz Biotechnology) with complete protease inhibitors (Sigma-Aldrich) and phosphatase inhibitors (PMSF as 1 mM final concentration and sodium orthovanadate as 0.2 mM final concentration). Cell suspension or homogenized tissue were incubated for 10 minutes at 4 °C then centrifuged at 12000 g for 30 minutes at 4 °C. And protein concentrations were determined by BCA assay (Thermo Fisher Scientific). Protein samples were mixed with 5x SDS sample application

buffer and boiled for 5 minutes and were separated by SDS-PAGE (percentage of Polyacrylamide gels depends upon target protein molecular weight: >80 kDa: 8%; 50-80 KDa: 10%; 20-50 KDa: 12%; 10-20 KDa: 15%). Samples were loaded into wells in the gel. One lane was reserved for a ladder. Running condition was as below: at constant 80 volts until dye line runs off the stacking gel and change to 100 volts until dye line runs off the solution gel. Proteins were transferred to PVDF membrane (Millipore) in a tank blot (200 mA for 2h) under cold condition. Membranes were blocked for 60 minutes at room temperature with 5% nonfat milk in Tris-buffered saline (TBS (10 mM Tris, 150 mM NaCl, pH 7.5)) followed by probed with primary antibodies (diluted in blocking buffer) (**Table 7**) overnight at 4 °C. For detection, secondary antibodies conjugated with HRP were used for 1 hour at room temperature (the rabbit secondary antibody was purchased from Promega (W4018), the mouse secondary antibody was from Promega (W4028), and the goat secondary antibodies were provided by Santa Cruz (sc-2378). 1:5000 diluted in blocking buffer for all secondary antibodies) followed by intensive washing with 1x TBST. The SuperSignal™ West Femto Chemiluminescent Substrate (Thermo Fisher Scientific) was added after washing the membranes and development was done using ImageQuant™ LAS 4000 Version 1.2 (GE healthcare Life Sciences, Germany) (Buffers used are listed in **Table 8**).

Table 7 Antibodies applied to western blot

Antibody	Company	Cat.	Host	Molecular Weight	Dilution
ALOX15	Santa Cruz	sc-32940	Rabbit	75kDa	1:200
CCR7	R&D	MAB197	Mouse	48 kDa	1:200
IL12	Abcam	ab9992	Goat	70, 40, 35 kDa	1:250
IL10	Santa Cruz	sc-8438	Mouse	Monomer:20 kDa Dimer: 37 kDa	1:200
CD206	Biolegend	321102	Mouse	162-17 5kDa	1:200
Beta-Actin	Abcam	ab8227	Mouse	42 kDa	1:5000
DRAM1	Santa Cruz	sc-81713	Mouse	26 kDa	1:500
Ki67	Abcam	Ab15580	Rabbit	345 kDa	1:500
Cleaved Caspase-3	Cell signaling	D175	Rabbit	36/19/17 kDa	1:500
Iba1	Abcam	Ab5076	Goat	17 kDa	1:500
MFSD12	Sigma-Aldrich	HPA042149	Rabbit	52 kDa	1:250
ACTR6	Sigma-Aldrich	HPA038588	Rabbit	45 kDa	1:250
HIF-1α	Abcam	ab2185	Rabbit	93 kDa	1:1000
CD74	Santa Cruz	sc-6262	Mouse	31-45 kDa	1:500
CA9	Novusbio	NB100-417	Rabbit	55 kDa	1:2000
UBXN4	Sigma-Aldrich	HPA036325	Rabbit	57 kDa	0.2 μg/mL

Table 8 Buffers used for SDS-PAGE & immunoblotting	
Buffer	Composition
10x SDS PAGE running buffer (pH 8)	35mM SDS 250mM Tris 0.86M glycine
Blotting buffer	25mM Tris 192mM glycine 20% methanol
5x SDS PAGE sample application buffer	1.5M Tris-HCl pH 6.8 10% SDS 50% glycerol 25% ß-mercaptoethanol 0.01% bromophenol blue

Cell and tissue morphological techniques

Immunocytochemistry (ICC)

A549 cells were seeded in 8-well chamber slides (BD BioSciences) at a density of 5000 cells/well. And macrophages were cultured in 12-well plate with Poly-d-Lysine-coated coverslips (18 mm diameter, neuVitro) in the well. Cells were washed with PBS for 5 minutes. Then cells were fixed with 4% Formaldehyde Fixative Solution for 10 minutes at room temperature. After fixation cells were washed three times with PBS and permeabilized with PBS containing 0.2% Triton X-100 for 10 minutes at room temperature, and then blocked with 5% BSA for 1 hour at room temperature. For each ICC staining, an isotype-specific immunoglobulins at the same protein concentration as the primary antibody was set as a negative control to demonstrate that the reaction visualized was due to the interaction of the epitope of the target molecule and the paratope of the antibody reagent, rather than nonspecific binding of the secondary antibody. Primary antibodies (**Table 9**) were diluted in the blocking solution and incubated with cells at 4 °C overnight. After incubation, cells were washed 3 times with PBS and incubated with the fluorescently conjugated secondary antibodies (anti rabbit IgG-AlexaFluor®488, AlexaFluor®555 and AlexaFluor®594, Invitrogen) at a dilution of 1:1000 for 1 hour protected from the light. Cells were washed 4 times with PBS and nuclei were counterstained with 4', 6-diamidino-2-phenylindole (DAPI, Life Technologies) diluted 1:100 for 10 minutes at room temperature. After a final rinse with PBS, cells slides were mounted with Dako fluorescent mounting medium and examined under LSM 710 confocal microscope.

Table 9 Antibodies applied to ICC				
Antibodies	Company	Cat. No.	Source	Dilution
ALOX15	Santa Cruz	sc-32940	Rabbit	1:100
IL12	Abcam	Ab9992	Goat	10 µg/mL (1:50)
CCR7	R&D	150503	Mouse	1:100
CD163	Abcam	Ab182422	Rabbit	1:300
CD68	Abcam	Ab955	Mouse	1:300
Ki67	Abcam	Ab15580	Rabbit	1:500
Cleaved Caspase-3	Cell signaling	D175	Rabbit	1:500

Haematoxylin & Eosin staining (H&E staining)

Lung tissues were dissected and fixed with 4% paraformaldehyde in PBS overnight at 4 °C. The tissue samples were rinsed in PBS, dehydrated, and then embedded in paraffin blocks. Paraffin sections were cut with 3 µm thickness and stained with haematoxylin and eosin (H&E) using standard protocols. Sections were deparaffinized and hydrated by heating at 60 °C for 1h and then by passing the slide through a series of three times of xylol, followed by a decreasing concentration of ethanol from 99.6% till 70%. After washing shortly in water, sections were incubated in Mayer's hematoxylin (AppliChem) for 20 minutes, washed under running water to get rid of excess dye and then incubated with Eosin Y (AppliChem). Slides were then washed briefly in water then dehydrated in a series of increasing ethanol concentration and then 3 times in xylol each for 10 minutes. Finally slides were mounted with Pertex (Medite GmbH) and sections were scanned with Nanozoomer 2.0HT digital slide scanner C9600.

Immunofluorescence staining (IFC)

Three-micrometer tissue sections were deparaffinized and rehydrated in graded series of alcohol. For antigen retrieval, sections were cooked in 10mM citrate buffer (10 mM Sodium citrate, 0.05% Tween 20, pH 6.0) or EDTA (10 mM Tris base, 1 mM EDTA solution, 0.05% Tween 20, pH 9.0) according to the antibody for 20 minutes, and then kept warm for further 10 minutes. Then, tissues were blocked in 5% BSA for 1 hour at room temperature, to avoid unspecific binding of the antibodies. For each IFC staining, an isotype-specific immunoglobulins at the same protein concentration as the primary antibody was set as a negative control. The following primary antibodies are listed in **Table 10**. After incubation with the primary antibodies at 4 °C overnight, slides were incubated with the corresponding Alexa Fluor®-labelled secondary antibodies (Invitrogen, Molecular Probes) at a dilution of 1:1000, counterstained with 4,6-diamidino-2-

phenylindole (DAPI, Life Technologies) and mounted with Dako fluorescent mounting media and examined under LSM 710 confocal microscope.

Table 10 Antibodies applied to IFC

Antibodies	Company	Cat. No.	Host	Dilution	Antigen Retrieval
ALOX15	Santa Cruz	sc-32940	Rabbit	1:100	EDTA
IL12	Abcam	Ab9992	Goat	10 µg/mL (1:50)	EDTA
CD68	Abcam	Ab955	Mouse	1:300	Citrate
CD163	Abcam	Ab182422	Rabbit	1:250	Citrate
Cytokeratin	DAKO	Z0622	Rabbit	1:250	Citrate
CA9	Novusbio	NB100-417	Rabbit	1:1000	Citrate
HIF-1α	Abcam	ab2185	Rabbit	1:500	Citrate
Ki67	Abcam	ab16667	Rabbit	1:100	Citrate
Cleaved Caspase-3	Cell signaling	9664	Rabbit	1:1000	Citrate
MFSD12	Sigma-Aldrich	HPA04214	Rabbit	1:150	Citrate
ACTR6	Sigma-Aldrich	HPA038588	Rabbit	1:100	Citrate
UBXN4	Sigma-Aldrich	HPA036325	Rabbit	1:100	Citrate

Opal multiplex staining and multispectral imaging

A cohort of 104 patients with stage I–IV lung cancer was included in the study of spatial distribution of TAMs. The Ethical Committee of the University Hospital Munich in Germany approved the collection and analysis of all samples, in accordance with the national law and the Good Clinical Practice/International Conference on Harmonization guidelines. Informed consent was obtained from all patients (reference AZ 58/15). Tissue microarrays (TMAs) were constructed for TC and IM of lung cancer samples. In standard paraffin sections, TC and IM regions were histomorphologically analyzed. TMAs were prepared using 1-mm tissue cores with 5-µm thickness using standard procedures. To evaluate tumor heterogeneity, three representative cores from IM and TC were used to construct TMAs for each patient.

Seven-color multiplex fluorescence staining was performed using the Opal kit (PerkinElmer). Opal multiplex staining is based on tyramide signal amplification strategy. Tyramide is a phenolic compound that covalently binds to electron rich moieties of adjacent proteins when activated by enzyme HRP. The primary and secondary antibodies can then be stripped away by heating, while the TSA fluorophore is largely unaffected by heating because it is covalently bound. This makes similar species of antibodies amenable for multiplex staining on the same tissue section without cross-reactivity. According to

manufacturer's recommendation, a negative control with omitted primary antibody was applied to optimize the primary antibody; and a negative control omitting both the Opal fluorophore and DAPI was used to control library establishment. The TMA slides were dewaxed with xylene, rehydrated through a graded ethanol series, and fixed with 10% neutral-buffered formalin (50 mL 37% Formaldehyde, 450 mL distilled water, 3.25 g Na_2HPO4, 2 g NaH_2PO4 were mixed to make 50 mL solution) prior to antigen retrieval that was performed with Opal AR6 buffer (from Opal kit, PerkinElmer) using microwave incubation. After blocking with 1% bovine serum albumin in PBS for 20 minutes at room temperature, the sections were incubated with the primary anti-Cytokeratin antibody in a humidified chamber overnight at 4 °C, followed by a horseradish peroxidase-conjugated secondary antibody in a humidified chamber for 1 hour at room temperature. Cytokeratin staining was visualized using Opal fluorophore 520 (1:50) with tyramide signal amplification. The slides were next incubated in AR6 buffer and heated in microwave. In a serial fashion, the slides were blocked with 1% bovine serum albumin in PBS, and incubated with the primary antibody and then with the corresponding horseradish peroxidase-conjugated secondary antibody as well as the Opal fluorophore (1:50). This process was performed sequentially five more times to stain for all targets using different fluorophores (**Table 11**). Finally, the nuclei were counterstained with DAPI for 5 minutes at room temperature. The sections were coverslipped using Vectashield HardSet Antifade fluorescence mounting medium [155].

The seven-color Opal slides were visualized using the Vectra quantitative pathology imaging system (PerkinElmer). The monoplex spectral library slides and the unstained samples were used to extract the spectrum of each fluorophore and the tissue autofluorescence, respectively. A spectral library for multispectral unmixing was established using the InForm image analysis software (PerkinElmer). Whole-slide scans for TMA core annotation were acquired at 10× magnification, followed by the acquisition of multispectral images at 20× magnification. Spectral unmixing was applied to distinguish the seven different fluorescent signals. The unmixed images were processed using the InForm image analysis with tissue segmentation, cell segmentation, and phenotyping. Tissue segmentation based on the epithelial cell marker Cytokeratin was used to differentiate the parenchyma from the stroma, and the DAPI-based cell segmentation was used to improve phenotyping. The cells were phenotyped into the following subsets: M1 TAMs, $CD68^{+}IL12^{hi}CCR7^{hi}CD163^{low}ALOX15^{low}$; M2 TAMs,

$CD68^{+}CD163^{hi}ALOX15^{hi}IL12^{low}CCR7^{low}$; and tumor cells, $Cytokeratin^{+}CD68^{-}$. Median intensities were used to set cut-off values for the stained markers. Sequentially, the counts of M1 and M2 TAMs were normalized to the total cell counts for the total TC and IM areas to generate the density of TAMs per 1000 cells. The proximity distance between the tumor cells and TAMs was measured using HALO software. The proximity distance was defined as the average number of tumor cells distributed within a 30-µm radius from the nuclear center of any given M1 or M2 [156].

Table 11 Antibodies used for Opal multiplex staining

Order	Antigen	Primary antibody				TSA fluorophore
		Provider	Catalog number	Host	Working concentration	
1	Cytokeratin	DAKO	Z0622	Rabbit	1:500	Opal520
2	ALOX15	Santa Cruz	sc-32940	Rabbit	1:200	Opal540
3	CD163	Abcam	ab182422	Rabbit	1:250	Opal570
4	IL12	Abcam	ab9992	Goat	1 µg/mL	Opal690
5	CCR7	R&D	MAB197	Mouse	1:100	Opal650
6	CD68	Abcam	Ab955	Mouse	1:300	Opal620
7	DAPI	-	-	-	-	Spectral DAPI

Animal experiments

Wild type C57Bl/6J mice were purchased from The Jackson Laboratory (Bar Harbor, ME, USA). Animals were kept in individually ventilated cages (IVC) in a pathogen-free environment and were handled in accordance with the European Union commission on Laboratory animals. Animal study proposals were approved by the Regierungspräsidium Giessen, the local regulatory authorities for animal research in Hessen, Germany (Animal proposals B2/288).

Routine veterinary assessment was performed to animal, including health observations and body condition scoring to maintain mice properly and define appropriate experimental endpoint. Inhalant anesthetic Isoflurane was applied to anesthesia in mice: 4 - 5% for induction and 1 - 2% for maintenance with calibrated vaporizer. Mice were visibly observed and monitored every 15 minutes during recovery from anesthesia until the animal was fully ambulatory. Overdose of chemical anesthetics (2-3 times the anesthetic dose) were used for euthanasia: 240 mg/kg Ketamine + 20 mg/kg Xylazine

through intraperitoneal injection. Death was verified prior to organ harvest or disposal: the mouse no longer responds to painful stimuli, such as paw pinch before proceeding. To perform perfusion to mice, 30 g needle from the tubing with PBS was inserted into the apex of the left ventricle, followed by cutting the right ventricle using standard scissors. Perfusion was sequentially conducted with PBS to mice to allow the blood to flow out. Then, tissues were collected for further imaging and analyzes.

Regardng subcutaneous lung tumor model, seven-week-old mice were injected subcutaneously with 10^6 LLC1 cells in 0.1 mL 0.9% saline solution into their hind flank (24 g needle, 0.55 × 25 mm, Neolus, Terumo Europe). Tumors were measured every 4 days using an external digital caliper to measure the greatest longitudinal diameter (length) and the greatest transverse diameter (width). The tumor volume was calculated by the modified ellipsoidal formula [112,149,157]: $Tumour\ Volume\ (mm^3) = 0.5\times$ length × width^2. Mice were sacrificed on the 20th day after tumor cell implantation and lungs and subcutaneous tumors were collected for further analysis.

Statistical analysis

Statistical analyzes were performed with SPSS ver. 17.0 (SPSS, Chicago, IL, USA), Prism ver. 6.0 (GraphPad Software), and R. Wilcoxon signed-rank test for two-paired samples was used for the analyzes of TAM density and proximity distance. Spearman's rank correlation coefficient was calculated to assess the correlations between the TAM-related variables and tumor size. The Mann-Whitney *U* and the Kruskal-Wallis tests were used for two and multiple independent samples, respectively. The Kaplan-Meier method was used to estimate overall survival, and differences were assessed using the log-rank test. The independent prognostic value was estimated using univariate and multivariate Cox proportional hazard regression models. Data are expressed mean (SD) [158]; and *P* values <0.05 were considered statistically significant unless otherwise specified. Significance level was noted as follows: * $P \leq 0.05$, ** $P \leq 0.01$, *** $P \leq 0.001$, **** $P \leq 0.0001$. For two-group comparisons among multiple independent samples, adjusted significance levels ($P = 0.01$ for six-group comparisons and $P = 0.17$ for four-group comparisons) were used to avoid increasing the type I error.

Results

Macrophages consist of antitumoral M1- and protumoral M2-subtypes

Mouse naive macrophages (M0) were isolated from murine bone marrow and polarized into M1 by stimulation with Lipopolysaccharide and Interferon-γ (LPS + rmIfnγ) and M2 by rmIl4 (**Figure 8A**). Successful polarization to M1 macrophages was confirmed by upregulation of M1 markers *Il1b*, *Tnfα*, *iNOS* and downregulation of M2 markers *Il10*, *Chitinase* and *Arginase*. Downregulated of M1 markers and upregulated of M2 markers confirmed the polarization to M2 macrophages (**Figure 8B**). Co-injection of M1 macrophages with murine lung carcinoma cells LLC1 significantly reduced tumor size (**Figure 8C**), while co-injection of M2 macrophages with LLC1 increased tumor growth (**Figure 8D**).

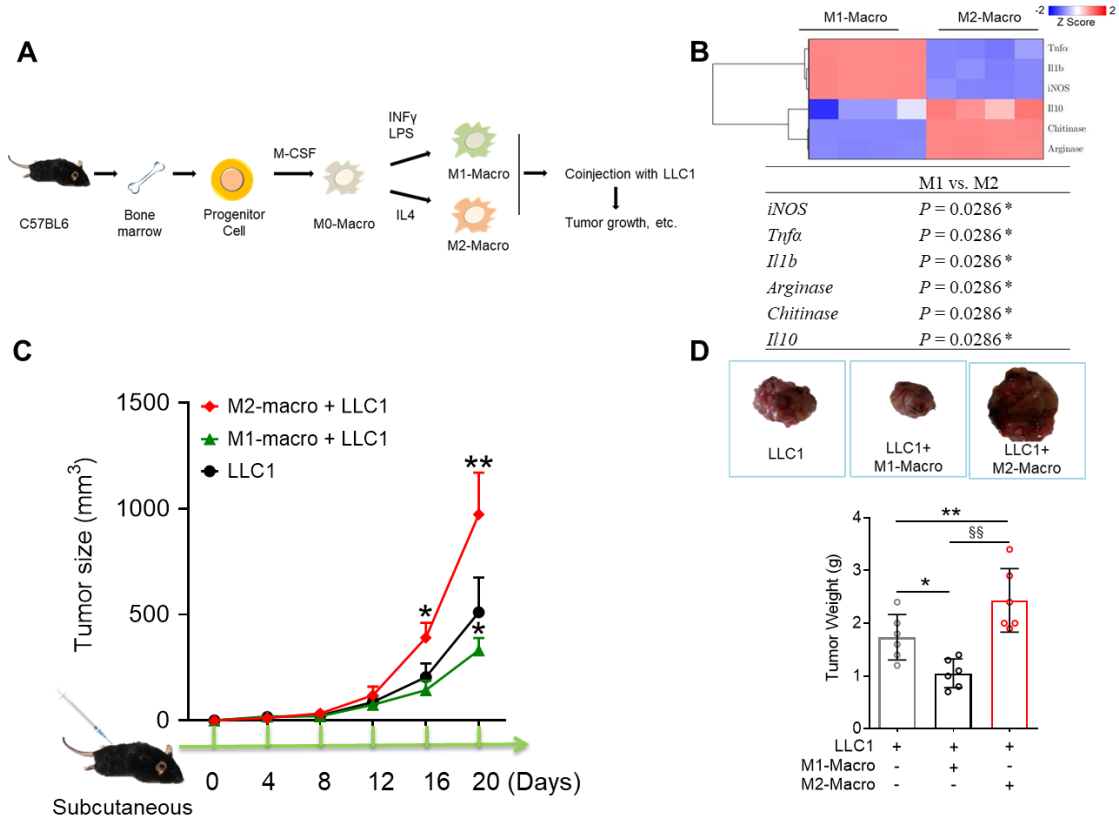

Figure 8 Co-injection of M1/M2 macrophages with lung tumor cells LLC1 alters tumor growth. (A) Experimental setup for the generation of bone-marrow derived mouse macrophages. (B) Heatmap showing relative mRNA expression of activation markers (M1 marker *Il1b*, *Tnfα* and *iNOS*; M2 marker *Il10*, *Chitinase* and *Arginase*) from mouse bone marrow-derived and cytokine-polarized macrophages. Z score represents the deviation from the mean by standard deviation units. Significance testing determined by the Mann-Whitney U test is listed in a table. n=4. (C-D) Mouse lung cancer cells LLC1 were subcutaneously co-injected with M1/M2 macrophages into C57BL/6 mice. Mice were sacrificed on the 21st day post-injection. Tumor size (C) and tumor weight (D) are shown. n=6. Significance was determined by the Kruskal-Wallis test. Data are presented

as the Mean (SD). ** P<0.01, * P<0.05.

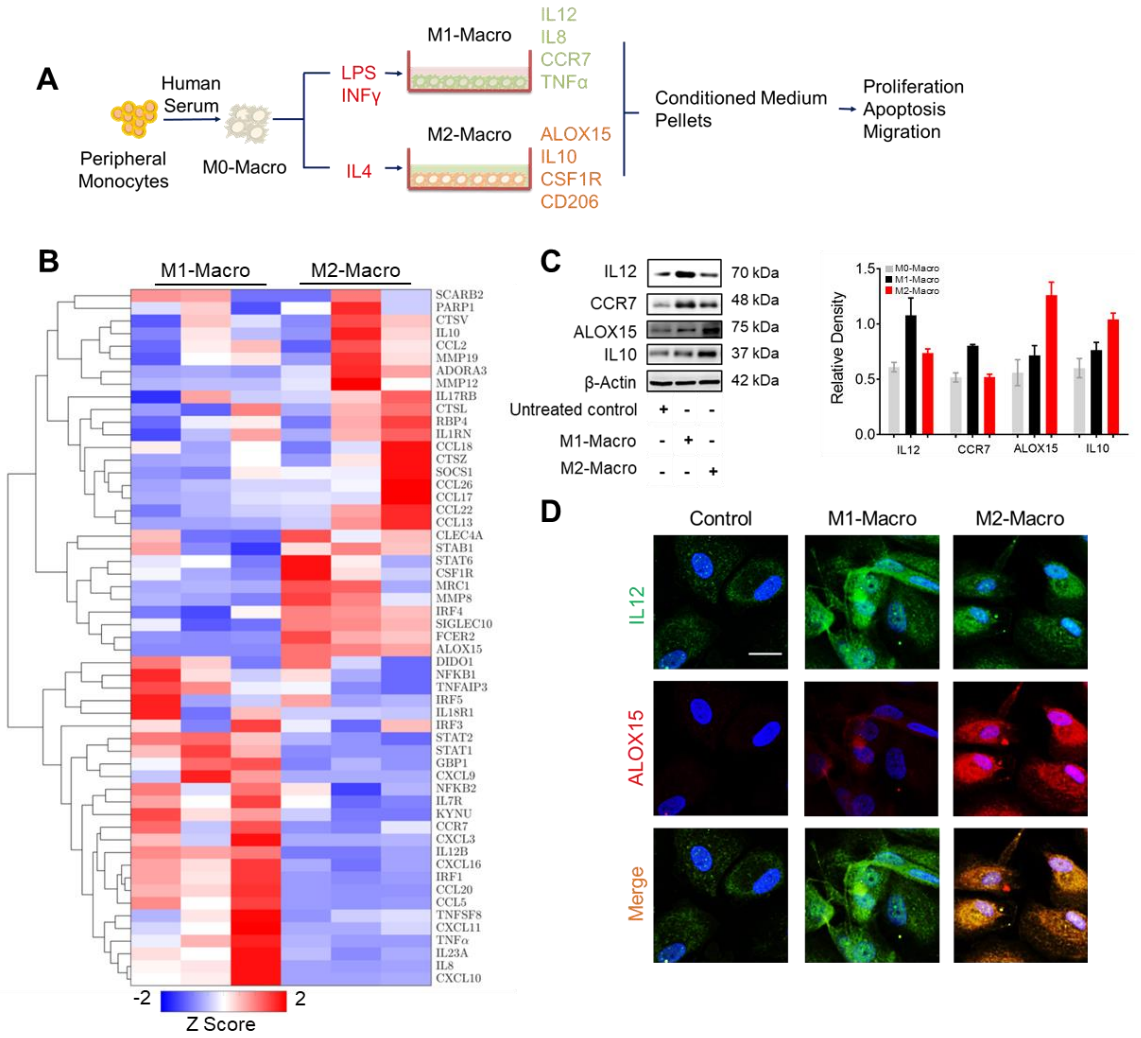

Figure 9 Macrophage marker alteration after polarization for 24 hours. (A) Schematic diagram for generation of human PBMC-derived and cytokine-polarized M1/M2 macrophage. (B) Heatmap showing expression of macrophage marker genes from triplicate sample RNA-seq experiments in PBMC-derived M1/M2 macrophages. Z score represents the deviation from the mean by standard deviation units. Hierarchical clustering analysis of marker genes is indicated on the left side. Red indicates high expression and blue indicates low expression relative to the row mean. (C) Representative western blot analysis of macrophage markers in control or polarized-macrophages. Quantification of three independent experiments is shown. (D) Representative images of ICC staining of IL12 and ALOX15 among M1, M2 and SAHA or VPA-treated M2 macrophages. Scale bar, 20 μm.

Human M0 macrophages were generated from peripheral blood mononuclear cells (PBMCs). M0 macrophages were cultured for 10 days in culture medium containing human serum followed by being polarized to M1 by LPS and rhIFNγ and M2 by rhIL4 (**Figure 9A**). M1 and M2 polarization was verified via checking a pool of macrophage

markers. Specifically, the heatmap generated from triplicate sample RNA-seq experiments revealed significant alterations of macrophage marker gene expression between M1 and M2 macrophages (**Figure 9B**). M1-markers IL12 and CCR7 were highly expressed in M1-polarized macrophages, while M2-markers ALOX15 and IL10 were expressed more at protein level in M2-polarized macrophages (**Figure 9C**). ICC staining further confirmed upregulation of M2-marker ALOX15 in M2-polarized macrophage and upregulation of M1-marker IL12 in M1-polarized macrophages (**Figure 9D**).

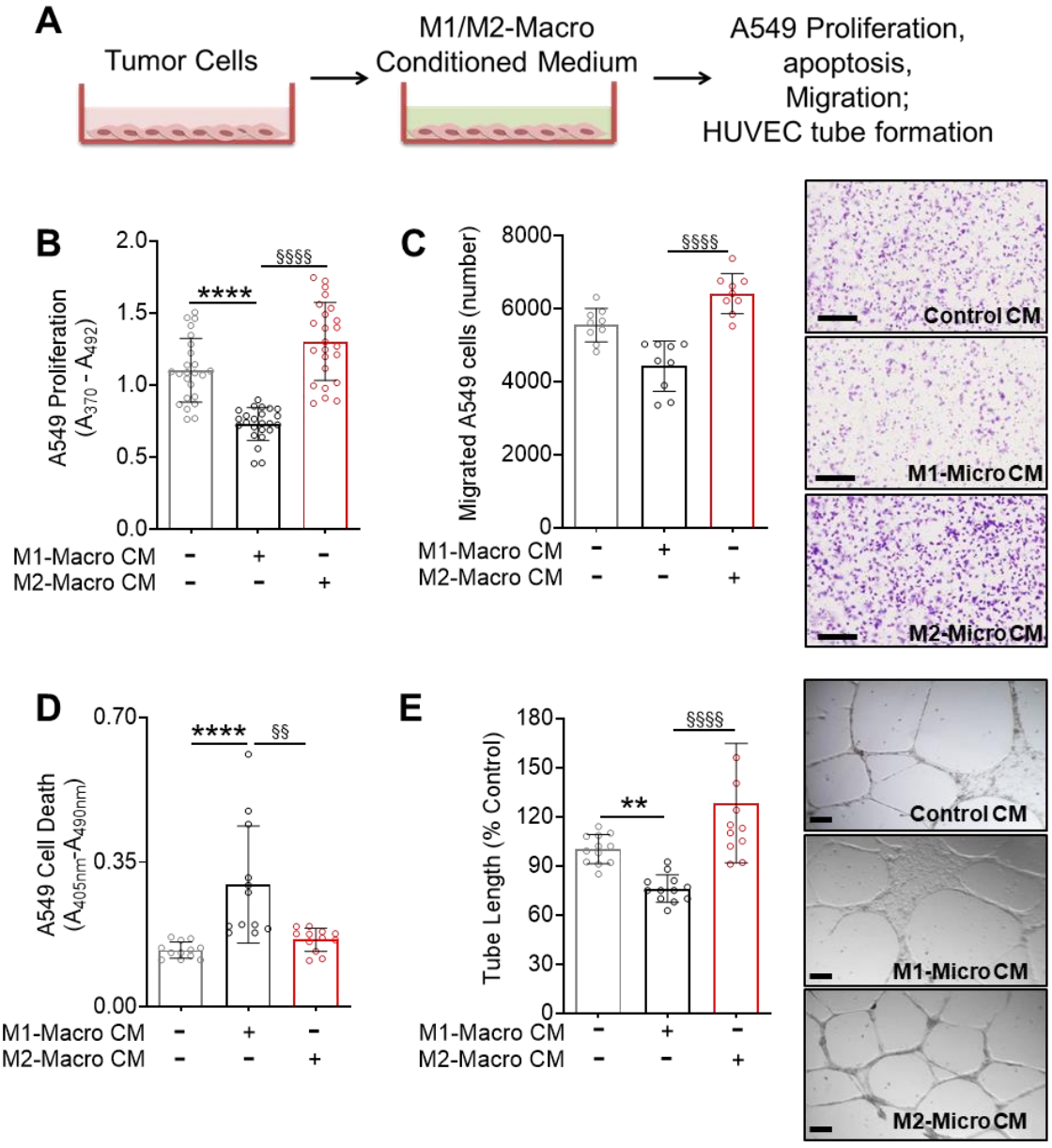

Figure 10 M2 Macrophages enhance the tumorigenicity of lung cancer cells. (A) Schematic diagram for the collection of conditioned medium (CM). (B-E) Functional alteration of lung cancer cells A549 in response to macrophage CM was determined using proliferation (D), transwell (E) and apoptosis (F) assays (Scale bar, 500 μm). (G) Tube

formation in the HUVEC culture was detected after incubation with macrophage CM. Mean tube length was normalized to control group with unpolarized-macrophage CM treatment. Scale bar, 10 μm. Significance determined by the Kruskal-Wallis test. Data are presented as the Mean (SD) of three independent experiments. ****/§§§§ P<0.0001, **/§§ P<0.01.

Functional analyzes were performed by treating lung cancer cells or HUVEC cells with macrophage conditioned medium (CM) (**Figure 10A**). M1 macrophage conditioned medium (M1-Macro CM) treatment significantly inhibited proliferation and migration of lung cancer cells A549 and reduced HUVEC tube formation, while dramatically increasing apoptosis in A549 cells. In contrast, M2 macrophage conditioned medium (M2-Macro CM) considerably enhanced A549 proliferation (**Figure 10B**) and migration (**Figure 10C**), while decreasing apoptosis of A549 (**Figure 10D**). M2 macrophage conditioned medium also significantly promoted HUVEC tube formation (**Figure 10E**). Taken together, these data show antitumoral capability of M1 macrophages and protumoral feature of M2 macrophages.

Gene expression profiling indicates heterogeneity among macrophage populations at the tumor center, invasive margin and non-tumor regions

RNA-seq analysis identified differentially expressed genes among TC (TC-TAMs), IM (IM-TAMs), and adjacent non-tumor tissue-derived macrophages (NMs). The Tumor epithelial cell marker CD326 [159], the neutrophil marker CD15 [160] and the common leukocyte marker CD45 [161] were used to exclude tumor cells; CD33 [162] and HLA-DR [163] were used to gate myeloid cells. Additionally, dendritic cells were excluded based on CD1c expression [164], and the macrophage markers MerTK [165], CD14 and CD64 [166] were used to purify macrophages using fluorescence-activated cell sorting (**Figure 11A**). The four-way plot determined differences in gene expression for IM-TAMs and TC-TAMs relative to NMs revealed 835 and 651 genes that were exclusively highly expressed in IM-TAMs and TC-TAMs, respectively. A total of 357 genes were expressed at comparable levels between TC-TAMs and IM-TAMs (**Figure 11B**). The top 50 differentially expressed protein-coding genes were shown in **Figure 11C**. Furthermore, distinct cellular signaling pathways were differentially activated among NMs, TC-TAMs and IM-TAMs. For instance, the expression levels of genes that govern the Cadherin and Wnt signaling pathways were significantly different between TC-TAMs and IM-TAMs

(**Figure 12A**). These findings revealed a substantial heterogeneity between the TAMs residing at TC versus those at IM, even in the same lung cancer sample. Therefore, in addition to comparing gene expression patterns in macrophages between tumor and adjacent non-tumor tissues, differences in the spatial distribution of TAMs between TC and IM may also require assessment. We also compared our data set with recently data reported by Lavin et al. [76] whose study described differentially regulated transcripts in lung adenocarcinoma-derived TAMs compared with NMs, including the downregulation of *LILRB2*, *LMNA*, *FCGR3A*, *VIM*, *LST1*, *HLA-DRA* and *FCN1*, and the upregulation of *TNFRSF1A*, *GPX1*, *CTSD*, *IER3, SPP1*, *CEBPB*, *CD163* and *TREME2* (**Figure 12B**) [76]. These data sets were highly comparable and confirmed the gene expression tendencies between NMs and lung squamous cell carcinoma-derived TC/IM-TAMs. Hence, the transcriptional signature of lung adenocarcinoma-derived TAMs is comparable to the transcriptional signature of lung squamous cell carcinoma-derived TAMs.

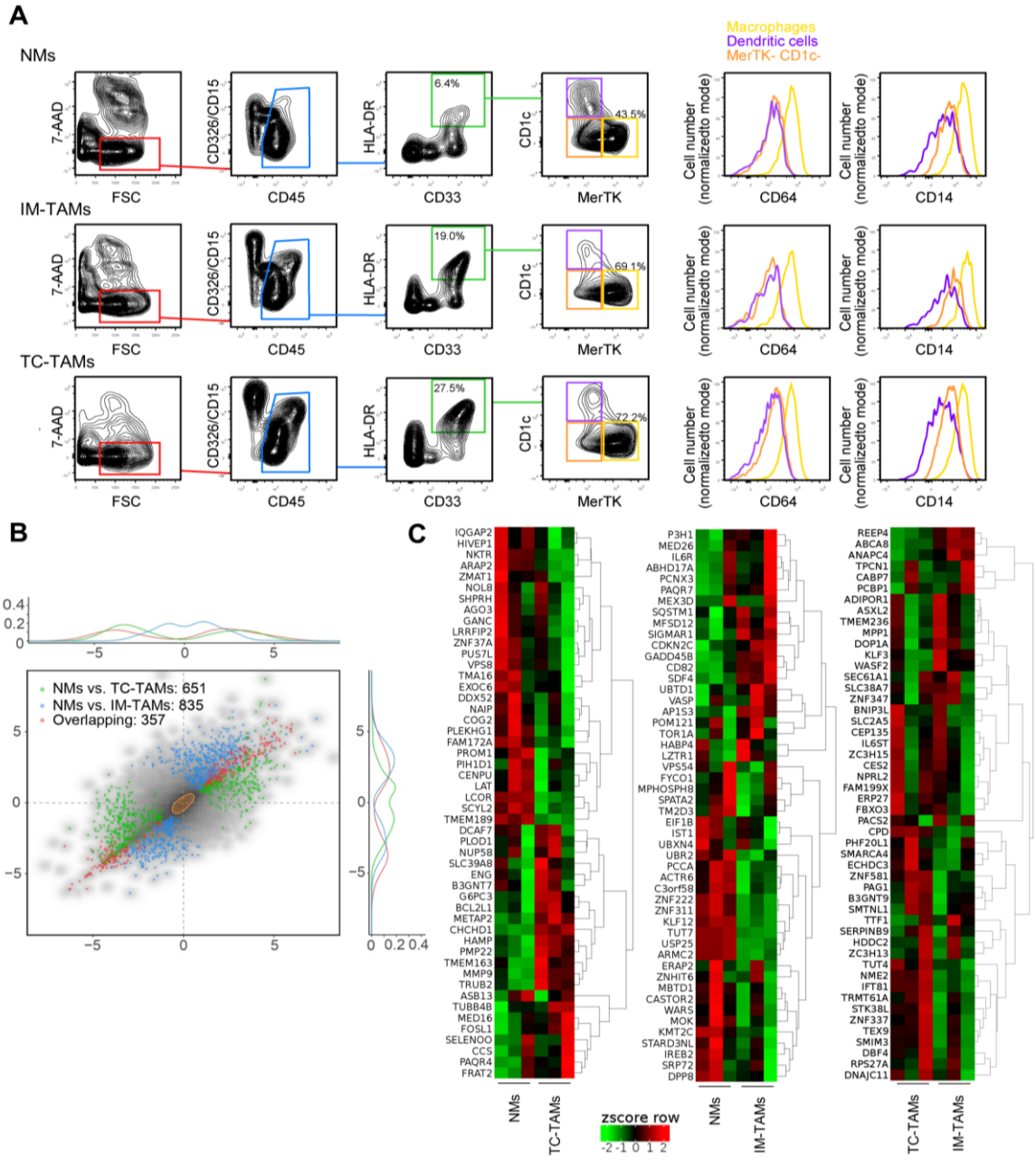

Figure 11 Gene expression profiling of macrophages from non-tumor tissues, TC, and the IM of lung cancer tissue specimens. (A) Representative FACS plots showing sorted macrophages (7-AAD$^-$, CD326$^-$, CD45$^+$, CD33$^+$, HLA-DR$^+$, CD1c$^-$, MerTK$^+$) from TC and IM of non-small-cell lung cancer tissue specimens and adjacent non-tumor tissues (IM, invasive margin; NM, non-tumor tissue; TC, tumor center; TAM, tumor-associated macrophage) (yellow gates). n = 3. (B) Four-way plot illustrating significantly differentially expressed genes and the overlapping genes between TC-TAMs and IM-TAMs, relative to NMs. (C) Heatmaps for the top 50 significantly differentially expressed protein-coding genes. Pairwise comparison was performed with DESeq2, in triplicate. The differentially expressed genes were selected based on a log FC > 0.58 or a log FC < −0.58, with a false discovery rate < 0.05 for the indicated comparisons. Adapted from Zheng et al., 2020 [61]. License details and the terms and conditions provided by American Association for Cancer Research and Copyright Clearance Center. License Number: 4941411272697.

Five specific markers are sufficient for distinguishing M1 and M2 TAM subtypes in lung cancer

To evaluate cell markers that might be appropriate for distinguishing TAMs, the mRNA expression levels of twelve M1 and M2 macrophage marker genes were evaluated in NMs, IM-, and TC-TAMs [166,167]. Compared with NMs, the expression levels of *IL12B*, *CCR7*, *ALOX15* and *CD163* were significantly altered in TAMs (**Figure 12C**). Therefore, the expression patterns of IL12B, CCR7, ALOX15, and CD163 were selected for examination by multiplex staining. Additionally, immunocytochemistry was performed to visualize Cytokeratin, CD68, IL12, CCR7, CD163, and ALOX15 in A549 lung cancer cells and M1 versus M2 peripheral blood monocyte-derived macrophages. Cytokeratin was exclusively expressed in A549 cells, whereas CD68 was solely expressed in macrophages (**Figure 12D**). Moreover, IL12 and CCR7 were highly expressed in M1 macrophages, whereas CD163 and ALOX15 were preferentially expressed in M2 macrophages (**Figure 12D**). Taken together, these observations indicate Cytokeratin and CD68 are sufficient for distinguishing cancer cells from macrophages, and the remaining examined marker set is capable of distinguishing M1 and M2 macrophage subtypes.

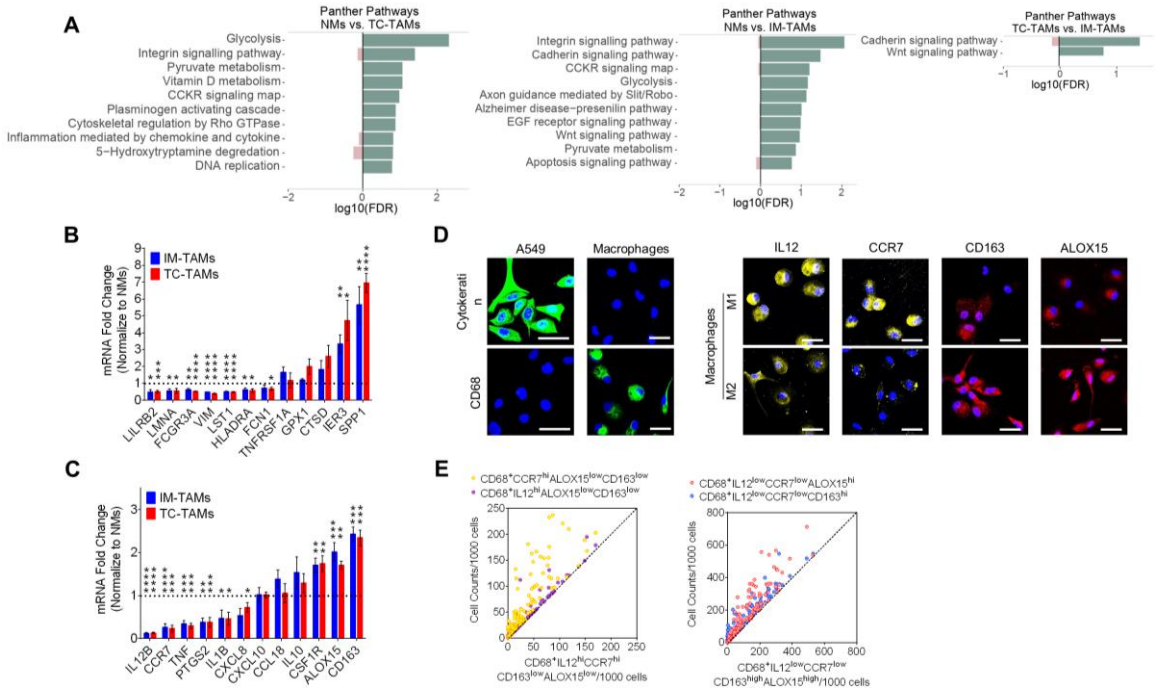

Figure 12 Pathway analysis and transcriptional signature in macrophages from different lung cancer regions and marker selection for Opal seven-color multiplex staining. (A) Gene set enrichment analysis demonstrating significant enrichment of gene set signatures in the PANTHER database for the indicated comparisons. The *x* axes

indicating the statistical significance (log10 false discovery rate, FDR) in enrichment for the indicated comparisons. (B) mRNA expression levels of differentially regulated transcripts, which were reported by Yonit Lavin et al. using single cell transcriptomic analysis of lung adenocarcinoma-derived TAMs [76], in lung squamous cell carcinoma. mRNA expression was detected using qRT-PCR and changes were determined relative to the respective expression in NMs from the same patients. Statistical significance was determined with *The Kruskal-Wallis test* and all data represent Mean (SD). * $P < 0.05$, ** $P < 0.01$; *** $P < 0.001$; **** $P < 0.0001$, n=4. (C) mRNA expression of 12 macrophage marker genes among NMs, TC- and IM-TAMs. mRNA expression was detected using qRT-PCR and changes were determined relative to the respective expression in NMs from the same patients. Statistical significance was determined with *The Kruskal-Wallis test* and all data represent Mean (SD). * $P < 0.05$, ** $P < 0.01$; *** $P < 0.001$; **** $P < 0.0001$, n=4. (D) Fluorescence microscopy of Cytokeratin (green) and CD68 (green) in A549 lung cancer cells and peripheral blood monocyte-derived macrophages. And expression of macrophage markers IL12 (yellow), CCR7 (yellow), CD163 (red) and ALOX15 (red) in M1/M2 macrophages determined by fluorescence immunocytochemistry. Cells were stained with DAPI for the nuclei (blue). Scale bar, 20 μm. (E) Comparison between four marker-defined and the five marker-defined TAMs. Five marker-defined TAMs include $CD68^{+}IL12^{hi}CCR7^{hi}CD163^{low}ALOX15^{low}$ M1 TAMs and $CD68^{+}IL12^{low}CCR7^{low}CD163^{hi}ALOX15^{hi}$ M2 TAMs. Each data point is located on the y-axis for the indicated four markers and the x-axis for the indicated five markers ($P < 0.001$). Statistical significance ($P < 0.05$) was determined with the Wilcoxon signed-rank test. Adapted from Zheng et al., 2020 [61]. License details and the terms and conditions provided by American Association for Cancer Research and Copyright Clearance Center. License Number: 4941411272697.

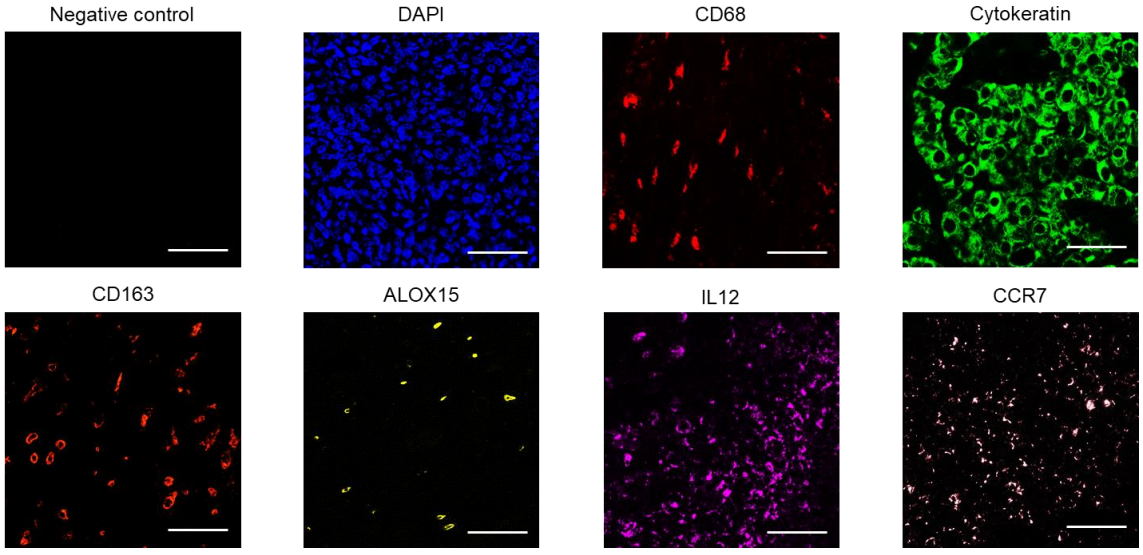

Figure 13 Optimization of primary antibody conditions for monoplex opal detection. Unstained slides, DAPI-only and optimized Opal single-stain lung cancer slides are required for library development. Scale bar, 100 μm.

Monoplex Opal staining was required for multiplex staining library development. Firstly,

the primary antibody conditions, including the working concentration and incubation time and antigen retrieval strategies, were optimized. The optimized condition was list in **Table 11**. Then, the optimized Opal single-stain slides, DAPI-only and unstained slides will be required for library development (**Figure 13**). After evaluating intensity and specificity of Opal monoplex slides, we combined verified monoplex Opal assays into multiplex panel with optimizing the staining sequence. Eventually, optimized multiplex panel was performed to TMAs (**Figure 13**).

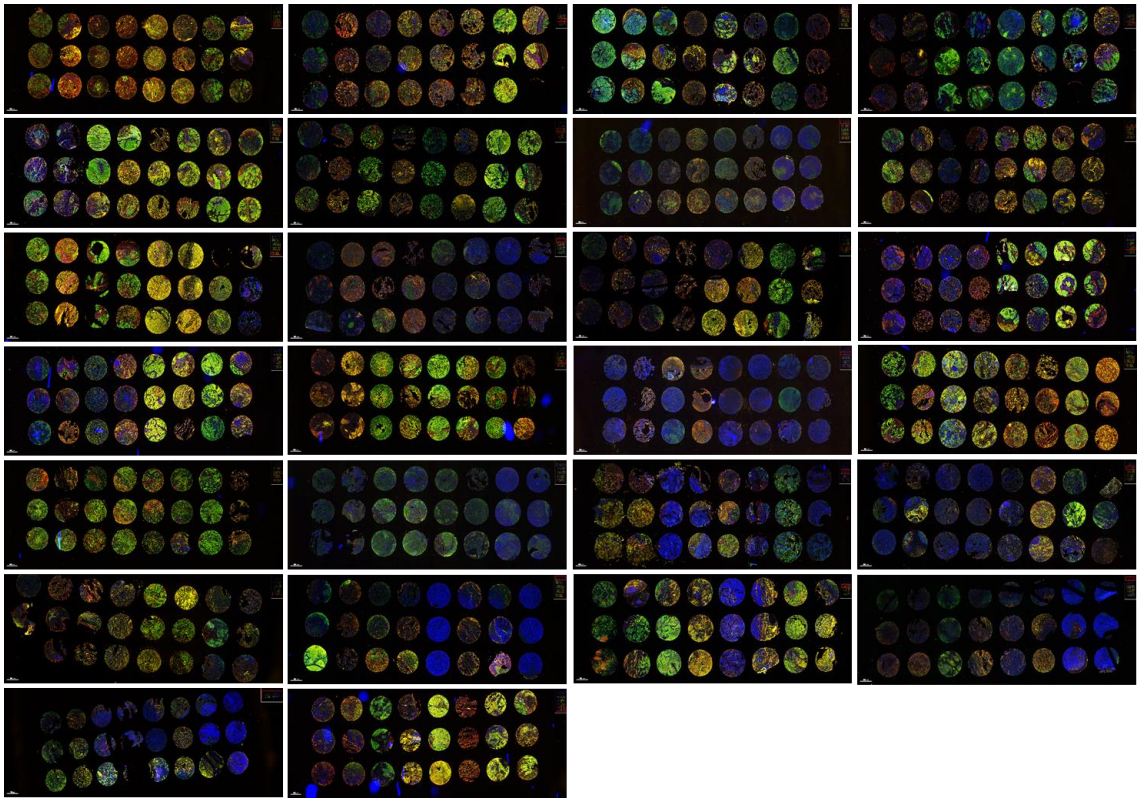

Figure 14 Multiplex staining of TMAs used in this study. Displayed images are from raw, whole-slide scans.

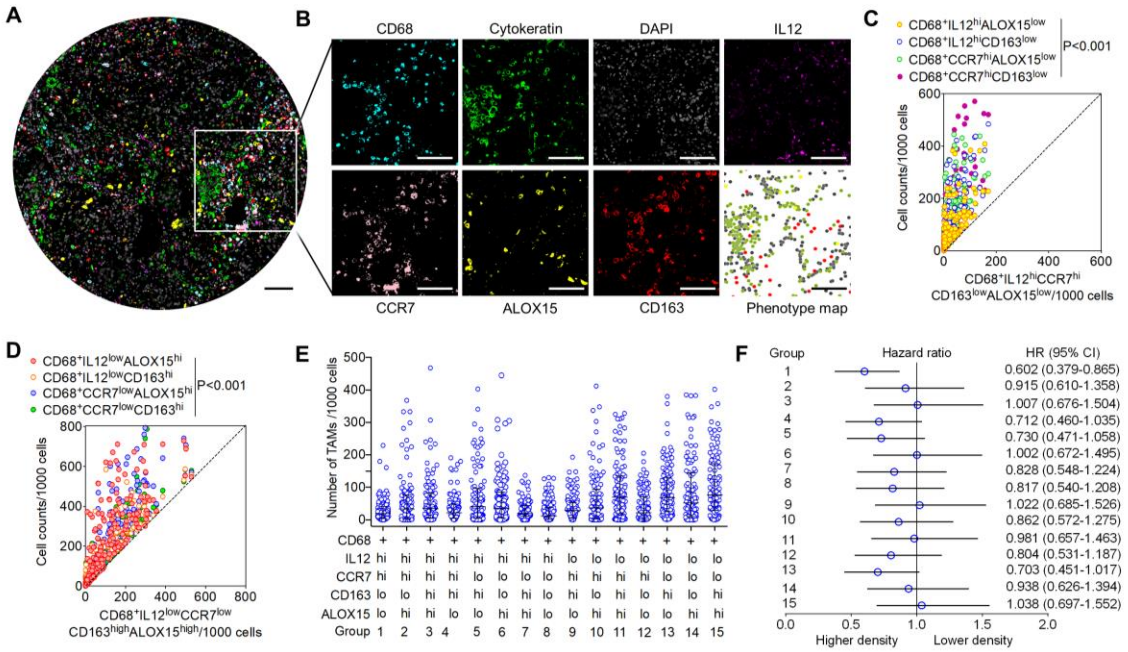

Figure 15 Opal seven-color multiplex staining identifies M1 and M2 TAMs in human lung cancer samples. (A) Representative composite image of a TMA core with Opal seven-color multiplex staining. Scale bar, 100 μm. (B) Individual markers in the framed area of composite images similar to that presented in panel (A), were used to generate phenotype maps using Inform software to determine cellular subpopulations including M1 TAMs (yellow dots), M2 TAMs (red dots), tumor cells (green dots), and other cells (gray dots). Pseudocolor illustrating CD68 (cyan), Cytokeratin (green), IL12 (magenta), CCR7 (pink), CD163 (red), ALOX15 (yellow), and DAPI (gray) staining. Scale bar, 100 μm. (C, D) Comparison between three- marker-defined and the five marker-defined macrophages, namely, $CD68^{+}IL12^{hi}CCR7^{hi}CD163^{low}ALOX15^{low}$ M1 TAMs (C) and $CD68^{+}IL12l^{ow}CCR7l^{ow}CD163^{hi}ALOX15^{hi}$ M2 TAMs (D). Each data point is located on the y-axis for the indicated three markers and the x-axis for the indicated five markers. Significance ($P < 0.05$) was determined with the Wilcoxon signed-rank test. (E) The densities of intermediate TAM subpopulations, defined as CD68+IL12/CCR7/ALOX15/CD163. The indicated expression levels of markers are displayed under the x-axis: lo, low-expression; hi: high-expression. Data are represented as medians, with interquartile ranges. (F) Survival analyzes of TAM subpopulation density-related parameters in tissue samples from lung cancer patients. The hazard ratios (HR) for death, associated with a higher density vs. a lower density of individual intermediate TAM subpopulations, are shown with 95% confidence intervals (CIs). Adapted from Zheng et al., 2020 [61]. License details and the terms and conditions provided by American Association for Cancer Research and Copyright Clearance Center. License Number: 4941411272697.

In line with the wide use of CD68 to identify monocyte lineage, the combination of CD68 and a single M1- or M2-related marker has been applied to distinguish TAM subtypes [60,168,169] (**Figure 14**; **Figure 15A**). To examine whether multiple staining for five macrophage markers (**Figure 15B**) is more effective than using three markers, scatter plots and Wilcoxon signed-rank test were used to compare M1 and M2 TAM densities

(TAM counts per 1,000 total cells). The axes in the plots represented the cell densities for the respective categories, and the data points located along the diagonal indicated similar cell densities between these two groups, suggesting a higher specificity if those data points were more distant from the diagonal. Compared with the TAMs defined by three markers (CD68, with a single marker for M1 and M2), the densities of TAMs defined by five markers were substantially lower (**Figure 15C**). More precisely, considering five markers as 100% specific, the specificity was decreased between 52-62% by three markers (**Figure 15D**) and 13-46% by four markers (**Figure 15E**). Furthermore, other than $CD68^{+}IL12^{hi}CCR7^{hi}CD163^{low}ALOX15^{low}$-defined M1 TAMs and $CD68^{+}CD163^{hi}ALOX15^{hi}IL12^{low}CCR7^{low}$-defined M2 TAMs, intermediate macrophage subpopulations were identified (**Figure 15E**). A significant benefit ($P = 0.010$) for overall survival was observed for patients with higher densities of $CD68^{+}IL12^{hi}CCR7^{hi}CD163^{low}ALOX15^{low}$-defined TAMs, which corresponded to a 40% reduction in the risk of death (**Figure 15F**). Of note, in addition to fluorescent composite images, inForm provides simulated brightfield monoplex IHC from the same data for improved visual interpretation (**Figure 16**). Together, these findings indicate that M1/M2 TAMs could be sufficiently distinguished from the non-M1/M2 populations using five markers.

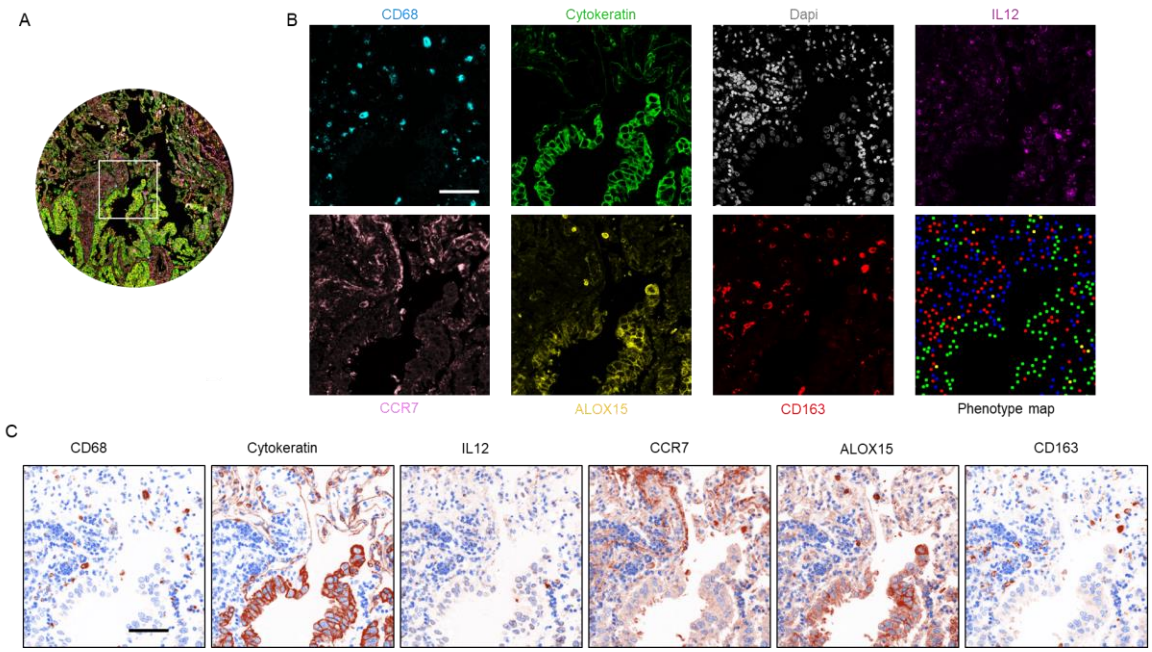

Figure 16 Simulated brightfield monoplex IHC. (A) Representative composite image of a TMA core with Opal seven-color multiplex staining. (B) Individual markers in the framed area of composite images similar to that presented in panel (A), were used to

generate phenotype maps using Inform software to determine cellular subpopulations including M1 TAMs (yellow dots), M2 TAMs (red dots), and other cells (green dots). Pseudocolor illustrating CD68 (cyan), Cytokeratin (green), IL12 (magenta), CCR7 (pink), CD163 (red), ALOX15 (yellow), and DAPI (gray) staining. (C) Simulated brightfield monoplex IHC from the same IFC staining. Scale bar, 100 μm.

Higher spatial density of M1 TAMs is associated with significantly longer overall survival of patients with lung cancer

Table 12 Characteristics of the lung cancer patient samples subjected to multiplex staining

Number of patients	104
Median age at the time of surgery, years	65 (38–83)
Median age at death (range), years	67 (46–87)
Median tumor size (range), cm	3 (0.7–13)
Median overall survival (range), months	37 (0–162)
Gender	
Male	72
Female	32
Subtype	
Adenocarcinoma	54
Squamous cell carcinoma	36
Large-cell carcinoma	10
Unidentified	4
Stage	
I	46
II	14
III	32
IV	11
Unidentified	1
Recurrence	
Yes	20
No	67
Unknown	17
Metastasis	
Yes	42
No	55
Unknown	7

Table 12 lists the baseline clinicopathological characteristics of the 104 patients with NSCLC that were enrolled in this study. The median age was 65 years (range, 38–83), and the median overall survival time was 37 months (range, 0–162). None of the patients underwent preoperative chemotherapy or radiotherapy. The histological grades assessed using the World Health Organization classification were adenocarcinoma, squamous cell carcinoma and large-cell carcinoma in 50% (n = 53), 37% (n = 36), and 10% (n = 10) of patients, respectively.

The heterogeneity of TAM density and distribution between TC and IM regions of lung adenocarcinoma, squamous cell carcinoma and large-cell carcinoma were assessed using seven-color multiplex fluorescence staining (**Figure 17A**). To visualize the distribution of TAMs and cancer cells, phenotype maps were generated based on previously described cell markers (**Figure 15B; Figure 17B**). For both TC and IM regions of all involved cancer subtypes, M2 TAMs showed a dominant density compared with M1 TAMs. The density of M2 IM-TAMs was significantly increased compared with that of M2 TC-TAMs, whereas the M1-TAM density did not differ significantly between TC and IM regions (**Figure 17C**). Moreover, M1 and M2 TAMs infiltrated significantly more in the stroma than in the parenchyma (**Figure 17D**). The M1 TC-TAM density of adenocarcinoma tended to be greater than that in squamous cell carcinoma (**Figure 17E**), whereas the M2-TAM density was comparable among all examined lung cancer subtypes (**Figure 17F**).

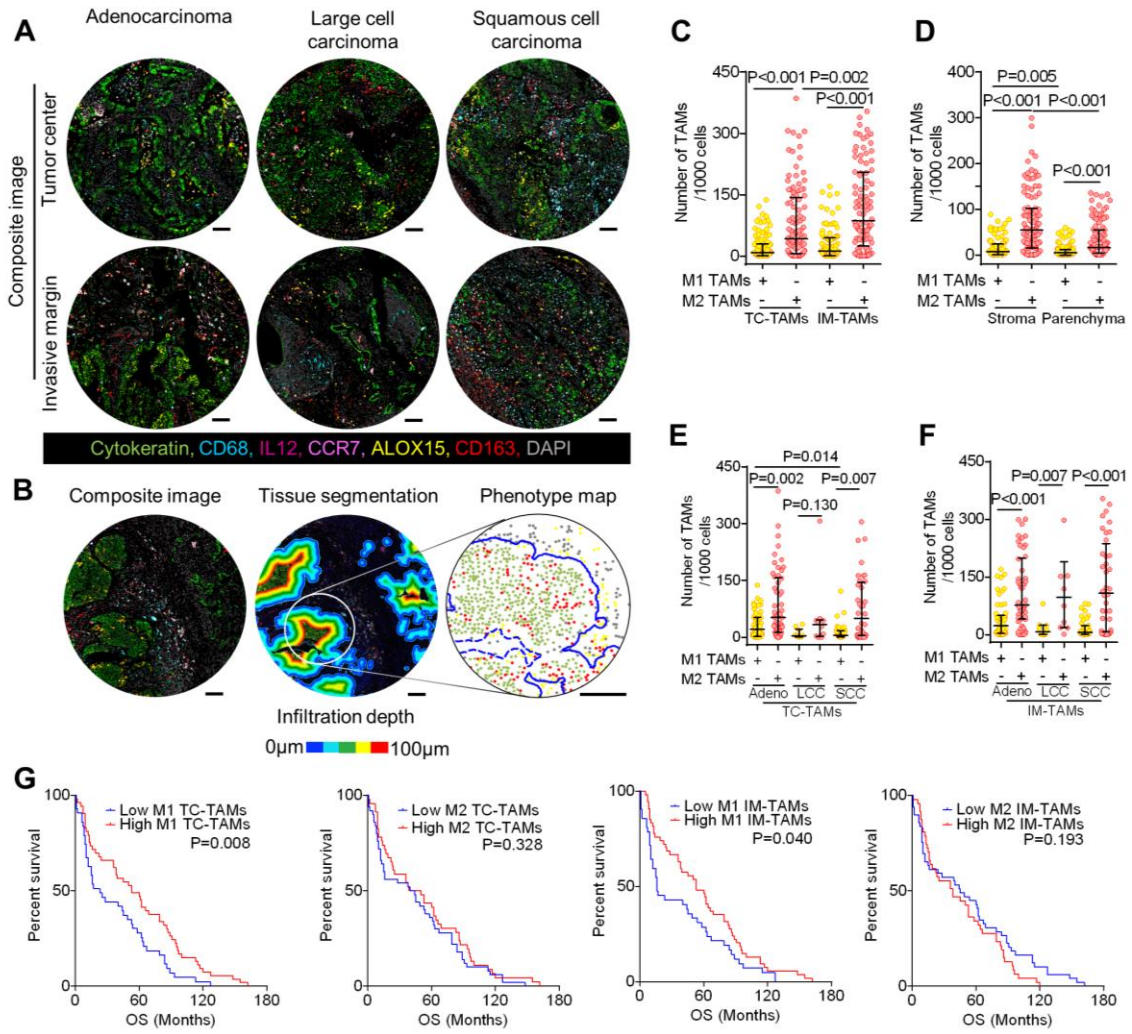

Figure 17 Spatial density of M1/M2 TAMs in human lung cancer samples and its correlations with survival and clinicopathological characteristics. (A) Representative composite images of tissue microarray (TMA) cores for adenocarcinoma (adeno), large-cell carcinoma (LCC) and squamous cell carcinoma (SCC). Pseudocolor illustration of CD68 (cyan), Cytokeratin (green), IL12 (magenta), CCR7 (pink), CD163 (red), ALOX15 (yellow), and DAPI (gray) staining. Scale bar, 100 μm. (B) Representative image showing the segmentation of the parenchyma from the stroma based on Cytokeratin staining. Colored areas show the parenchyma, and the color gradient of colors denotes the edge of the parenchyma (blue), to an infiltration depth of 100 μm (red). Representative phenotype map (right, enlarged area denoted by the white circle), generated using HALO software to illustrate M1 TAMs (yellow dots), M2 TAMs (red dots), tumor cells (green dots), and other cell types (gray dots), from subsections of the segmented tissue. In the phenotype map, a blue line encircles the parenchyma. (C, D) Comparisons of the M1 and M2 TAM densities between TC and IM (C) and between the stroma and parenchyma (D), in segmented tissues. The data are presented as the median and interquartile ranges, and statistical significance ($P < 0.017$) was determined with the Kruskal-Wallis test. (E, F) Comparisons of the M1 and M2 TAM densities at TC (E) and IM (F) of the TMA cores among the various lung cancer subtypes. The data are presented as the median and interquartile ranges, and statistical significance ($P < 0.010$) was determined with the Kruskal-Wallis test. (G) Kaplan-Meier survival analyzes of M1/M2 TAM density-related parameters in tissue samples from lung-cancer patients. Patients were divided into the

high and low groups, based on TAM densities above and below the median values, respectively. The calculations were based on all patients who reached the overall survival endpoint. *P*-values reflect the comparisons between two groups by univariate analysis using the log-rank test. Adapted from Zheng et al., 2020 [61]. License details and the terms and conditions provided by American Association for Cancer Research and Copyright Clearance Center. License Number: 4941411272697.

To evaluate whether the spatial TAM density differences could predict prognosis, all patients in the entire cohort were dichotomized based on the median TAM density. The Kaplan-Meier estimates revealed significant differences in overall survival according to the M1 TAM density. Patients with a high M1 TC- and IM-TAM densities had a significant overall survival benefit compared with those with a low M1 TC- and IM-TAM densities. However, there were no significant associations between the M2-TAM densities and overall survival (**Figure 17G**). We also investigated the relationship between the spatial TAM density and overall survival among the different cancer subtypes and found that adenocarcinoma patients with increased M2 IM-TAM densities had a poorer prognosis, whereas higher M1 TC-TAM densities were associated with longer survival in patients with squamous cell carcinoma (**Figure 18A**). However, the TAM density was neither significantly correlated with overall survival in patients with large-cell carcinoma nor with the aforementioned clinicopathological characteristics (**Figure 18A**; **Table 13**). Furthermore, when measured at an infiltration depth of 100 μm, there were more M2 TAMs than M1 TAMs were identified infiltrating the parenchyma, indicating that the tumor cells in the analyzed samples were closer to the M2 TAMs than to the M1 TAMs (**Figure 17B; Figure 18B**).

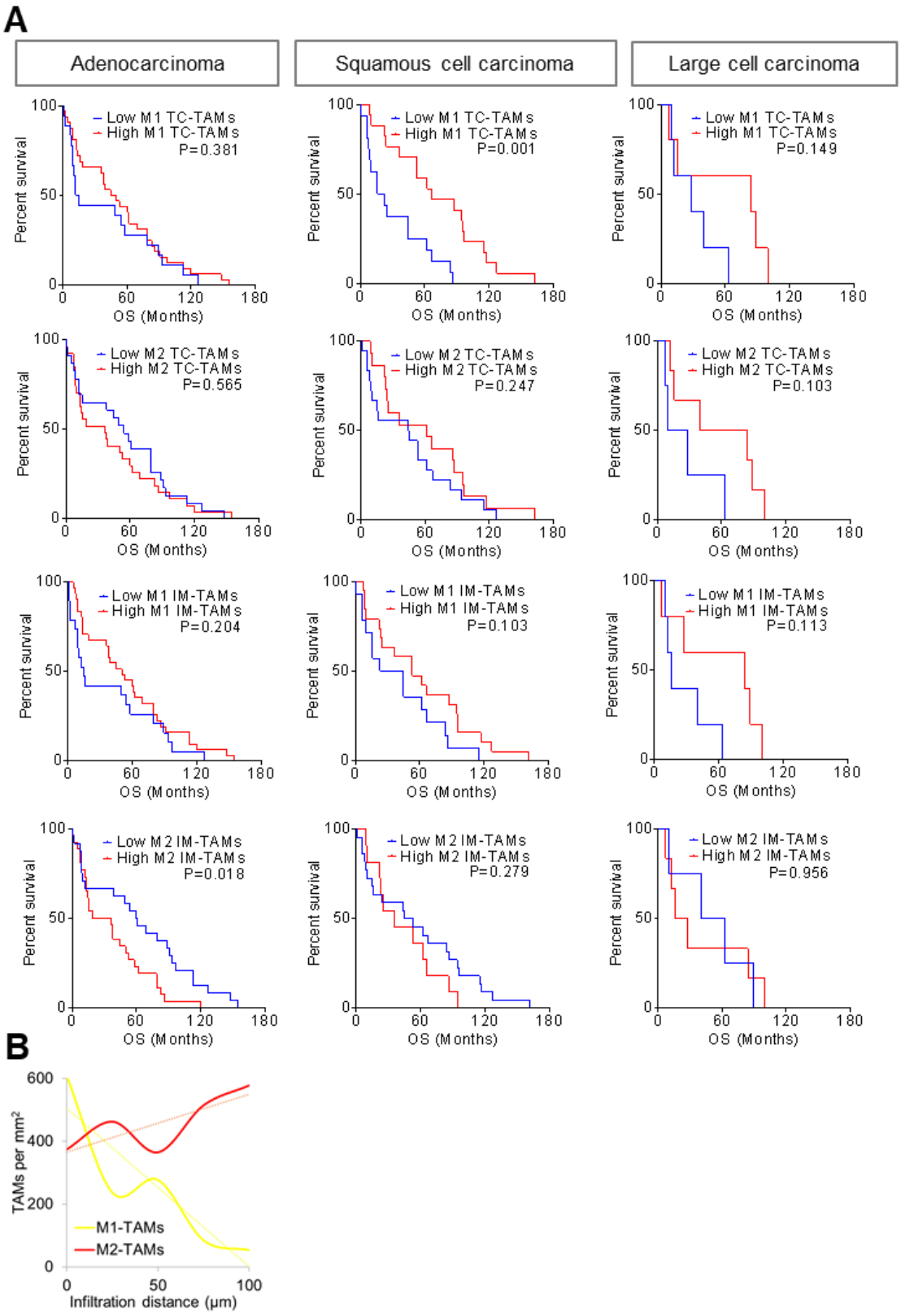

Figure 18 Kaplan-Meier survival analyzes of the TAM density-related parameters in different lung cancer types. (A) Correlation of the TAM density at either TC or IM with overall survival of patients with adenocarcinoma (n = 41), squamous cell carcinoma (n = 26), and large-cell carcinoma (n = 9). *P* values reflect comparisons of two groups by univariate analysis using the log-rank test. (B) Infiltration distance curve for evaluating

TAM density in the parenchyma of the segmented tissues shown in Figure 17B. Adapted from Zheng et al., 2020 [61]. License details and the terms and conditions provided by American Association for Cancer Research and Copyright Clearance Center. License Number: 4941411272697.

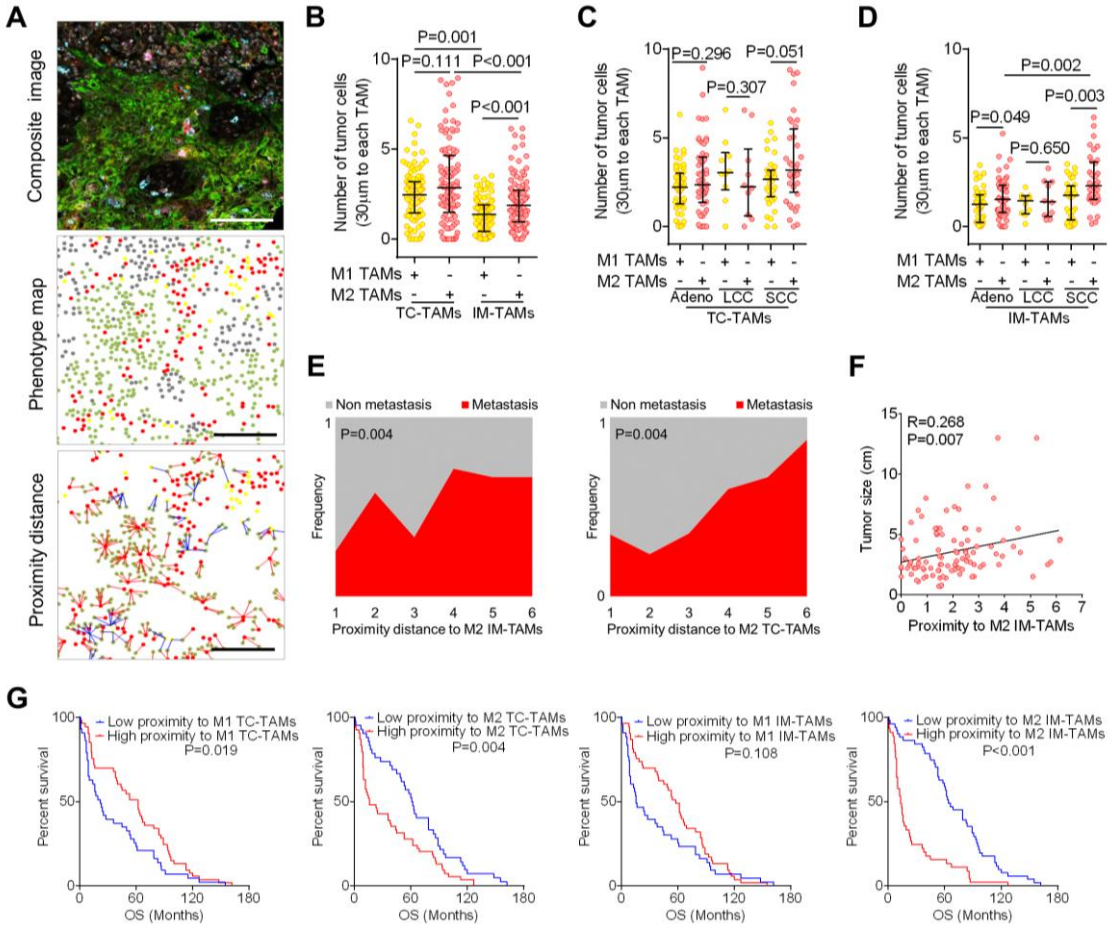

Figure 19 Spatial distribution of the M1/M2 TAMs in human lung cancer samples and its correlations with survival and clinicopathological characteristics. (A) Representative composite image with pseudocolors showing staining for CD68 (cyan), Cytokeratin (green), IL12 (magenta), CCR7 (pink), CD163 (red), ALOX15 (yellow), and DAPI (gray). Representative phenotype map for M1 TAMs (yellow dots), M2 TAMs (red dots), tumor cells (green dots), and other cell types (gray dots). Representative proximity distance map showing tumor cells within a radius of 30 μm from the nuclear center of each M1 and M2 TAMs. Scale bar, 100 μm. (B) Comparisons of the average proximity distances between the tumor cells and the M1/M2 TAMs at TC and IM of the TMA cores. The data are presented as the median and interquartile ranges, and statistical significance ($P < 0.017$) was determined with the Kruskal-Wallis test. (C and D) Comparisons of proximity distances between the tumor cells and the M1/M2 TAMs in TC (C) and IM (D) of the TMA cores among different histological subclasses of lung cancer. The data are presented as the median and interquartile ranges, and statistical significance ($P < 0.01$) was determined with the Kruskal-Wallis test. (E) Spine plots illustrating the proximity of tumor cells to the M2 TC/IM-TAMs, based on the presence of metastasis. Significance

was determined with the Mann-Whitney *U* test. (F) Correlation between the proportion of M2 IM-TAMs and tumor size. Significance was determined using Spearman's rank correlation. (G) Kaplan-Meier survival analyzes based on the proximity between tumor cells and the M1/M2 TAMs in lung cancer samples. The high- and low-proximity values were determined based on the median percentage, and calculations were based on all patients who reached the overall survival endpoint. Significance was determined using the log-rank test. Adapted from Zheng et al., 2020 [61]. License details and the terms and conditions provided by American Association for Cancer Research and Copyright Clearance Center. License Number: 4941411272697.

Spatial distributions of M1/M2 IM-TAMs are independent survival predictors

The phenotype maps allowed us to determine the spatial proximity distance between TAMs and tumor cells (**Figure 19A**). Proximity was defined as the average number of tumor cells distributed within a 30-µm radius from the nuclear center of any given M1 or M2 [156]. Overall, the tumor cells were located more proximally to M2 IM-TAMs than to M1 IM-TAMs (**Figure 19B**). More precisely, the tumor cells were closer to M2 IM-TAMs than to M1 IM-TAMs in squamous cell carcinoma (**Figure 19C**) (**Figure 19D**). Additionally, spine plots revealed that the incidence of metastasis increased significantly with the increasing proximity of tumor cells to either M2 TC-TAMs or M2 IM-TAMs (**Figure 19E** and **Table 13**). Besides, larger tumor size differences were significantly correlated with the increased proximity of tumor cells to M2 IM-TAMs (**Figure 19F** and **Table 13**). Furthermore, among overall lung cancer cohort, the survival was significantly longer among patients with tumor cells that were closer to M1 TC-TAMs or more distant from M2 TC/IM-TAMs (**Figure 19G**). This profile was true for all histological cancer subtypes; though significance levels were only partially reached due to the low sample numbers (**Figure 20**).

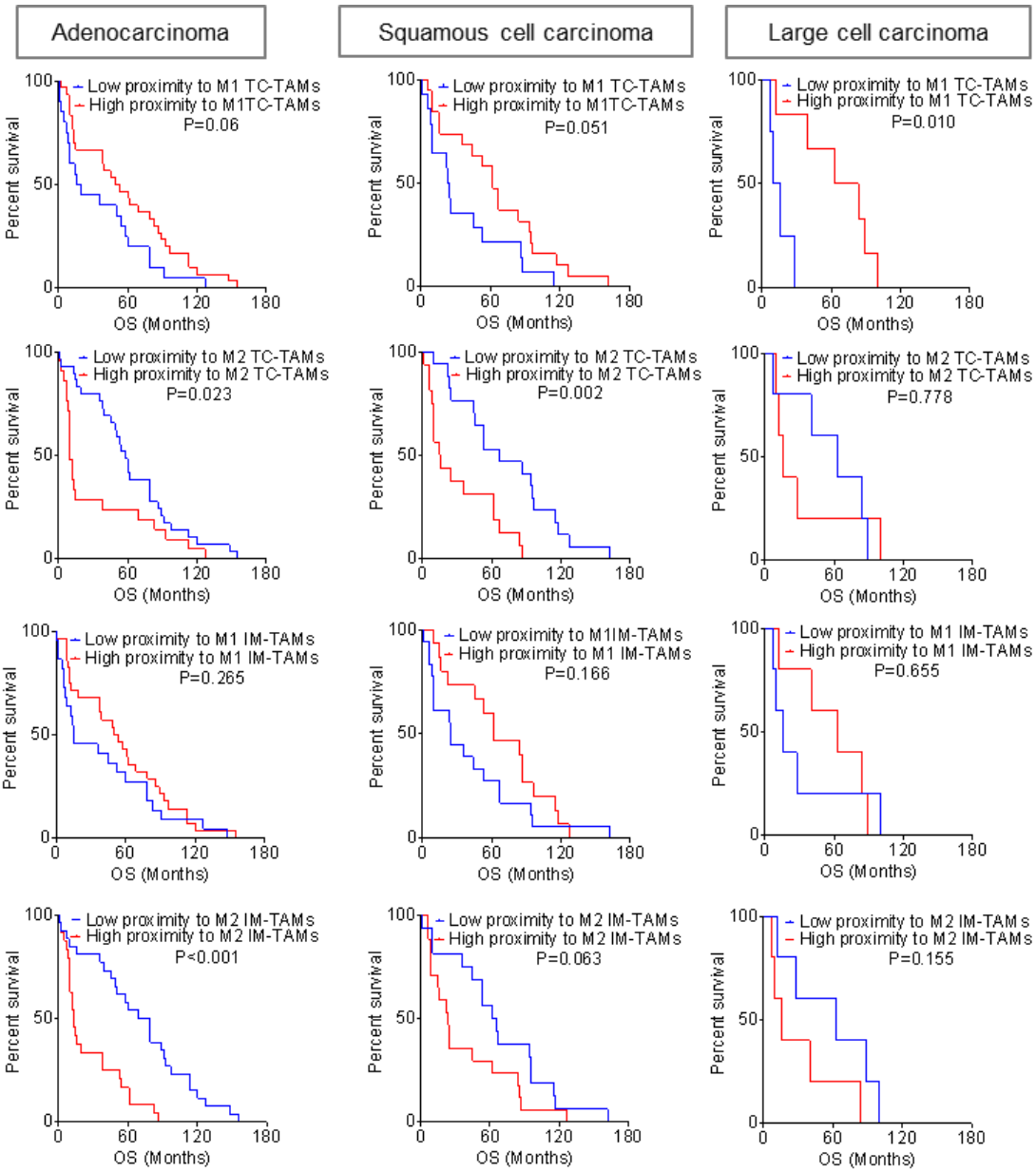

Figure 20 Kaplan-Meier survival analyzes of the TAM spatial distribution -related parameters in different lung cancer types. The correlation of TAM spatial proximity at either TC or IM with overall survival of patients with adenocarcinoma (n = 41), squamous cell carcinoma (n = 26), and large-cell carcinoma (n = 9). Statistical significance was d etermined using the log-rank test. Adapted from Zheng et al., 2020 [61]. License details and the terms and conditions provided by American Association for Cancer Research and Copyright Clearance Center. License Number: 4941411272697.

Table 13 Correlation of TAM-related variables with clinicopathological features

Clinicopathological feature		*P* values			
		Tumor size	Metastasis	Tumor stage	Recurrence
Density	M1 TC-TAMs	0.430	0.686	0.831	0.486
	M2 TC-TAMs	0.717	0.716	0.574	0.781
	M1 IM-TAMs	0.289	0.850	0.597	0.408
	M2 IM-TAMs	0.615	0.462	0.827	0.565
Proximity	M1 TC-TAMs	0.653	0.830	0.293	0.499
	M2 TC-TAMs	0.313	0.004	0.289	0.646
	M1 IM-TAMs	0.699	0.615	0.380	0.968
	M2 IM-TAMs	0.007	0.024	0.403	0.066
Statistical test		Spearman's rank correlation	Mann-Whitney U test		

Differences in TAM spatial density and proximity with respect to tumor size, metastatic status, tumor stage, and recurrence. TAMs, tumor-associated macrophages; TC, tumor center; IM, invasive margin.

Multivariate Cox proportional hazard analysis was applied to determine whether the spatial density and distribution of TAM subtypes were independently associated with overall survival time (**Table 14**). Along with the density of TAMs and the proximity of tumor cells to TAMs, age, gender, tumor stage, tumor size, metastatic and recurrent status, and histologic subtypes were included in the multivariate analysis. Univariate Cox regression analysis revealed that tumor stage, tumor size, metastasis, and the proximity of tumor cells to M1 TC-TAMs or M2 TC/IM-TAMs had significant impacts on overall survival. Multivariate analysis indicates that tumor stage (HR 1.728, $P = 0.001$), metastasis status (HR 2.304, $P = 0.040$), histologic subtype (HR 0.652, $P = 0.014$), M1 TC-TAM density (HR 0.986, $P = 0.030$), proximity of tumor cells to M1 IM-TAMs (HR 0.503, $P < 0.001$), and proximity of tumor cells to M2 IM-TAMs (HR 2.049, $P < 0.001$) were independent predictors of overall survival.

Table 14 Cox regression analysis of prognostic factors for overall survival

	Univariate		Multivariate		
	P value	EXP (B) (95% CI)	B	*P* value	EXP (B) (95% CI)
Age	0.803	0.997 (0.977–1.018)		0.661	
Gender	0.975	1.007 (0.661–1.534)		0.256	
Stage (I *vs.* II *vs.* III *vs.* IV)	<0.001	1.651 (1.355–2.011)	0.547	0.001	1.728 (1.249–2.391)
Metastasis (present *vs.* absent)	0.001	2.139 (1.387–3.301)	0.835	0.040	2.304 (1.038–5.116)
Recurrence (present *vs.* absent)	0.624	1.138 (0.678–1.912)		0.053	
Tumor size	0.026	1.105 (1.012–1.206)		0.887	
Histologic subtype (Adeno *vs.* SCC *vs.* LCC)	0.663	0.954 (0.772–1.179)	–0.428	0.014	0.652 (0.462–0.918)
M1 TC-TAM density	0.157	0.995 (0.988–1.002)	–0.014	0.030	0.986 (0.973–0.999)
M2 TC-TAM density	0.133	0.998 (0.996–1.001)		0.889	
M1 IM-TAM density	0.341	0.998 (0.993–1.003)		0.495	
M2 IM-TAM density	0.346	1.001 (0.999–1.002)		0.131	
M1 TC-TAM proximity	0.034	0.843 (0.721–0.987)		0.862	
M2 TC-TAM proximity	0.001	1.180 (1.071–1.301)		0.946	
M1 IM-TAM proximity	0.078	0.833 (0.680–1.021)	–0.687	< 0.001	0.503 (0.350–0.723)
M2 IM-TAM proximity	<0.001	1.311 (1.138–1.511)	0.717	< 0.001	2.049 (1.479–2.837)

TAMs, tumor-associated macrophages; TC, tumor center; IM, invasive margin; Adeno, adenocarcinoma; SCC, squamous cell carcinoma; LCC: large cell carcinoma; EXP (B), exponentiation of the B coefficient.

Proximity of tumor cells to TAMs is associated with tumor cell survival

The proliferation marker Ki67 and the apoptosis marker cleaved Caspase-3 were used to evaluate tumor cell turnover. However, technical limitations associated with the seven-color staining protocol confined our ability to stain additional markers. Therefore, we were forced to omit one macrophage marker to stain for either Ki67 or cleaved Caspase-3. As determined previously, the omission of IL12, CCR7, ALOX15, or CD163 would lead to 46%, 13%, 32%, and 23% reduction in specificity, respectively, indicating that CCR7 was the least important macrophage marker (**Figure 12E; Figure 15C**). Therefore, staining for CD68, IL12, ALOX15, CD163, Cytokeratin, DAPI, and either Ki67 or cleaved Caspase-3 was performed using TMAs. Cleaved Caspase-3^{+} tumor cells were more proximal to M1 TAMs than to M2 TAMs (**Figure 21A**). In contrast, $Ki67^{+}$ tumor cells were more distal to M1 TAMs than to M2 TAMs (**Figure 21B**). Therefore, the proximity of TAMs to tumor cells was associated with tumor cell survival. These results suggest M1 TAMs might promote apoptosis in proximal tumor cells, whereas M2 TAMs might establish a favorable environment that allows tumor cells to survive and proliferate.

Hypoxia contributes to the accumulation of M2 TAMs

To investigate the relationship between hypoxia and the accumulation of M2 TAMs, especially at IM, the hypoxic status of tumors was assessed by analysis of hypoxic marker expression patterns, including carbonic anhydrase 9 (CA9) and hypoxia-inducible factor 1-alpha (HIF-1α) [92,170]. The expression levels of HIF-1α (**Figure 21C**) was significantly elevated compared with those at TC (**Figure 21D**). Additionally, positive correlations between M2 TAM density at IM and the expression of HIF-1α was observed (**Figure 21E**). Likewise, the expression levels of CA9 (**Figure 21F**) was significantly increased compared with those at TC (**Figure 21G**). M2 TAM density at IM and the expression of CA9 was positively correlated (**Figure 21H**). These findings suggest that hypoxia contributes to the accumulation of M2 TAMs.

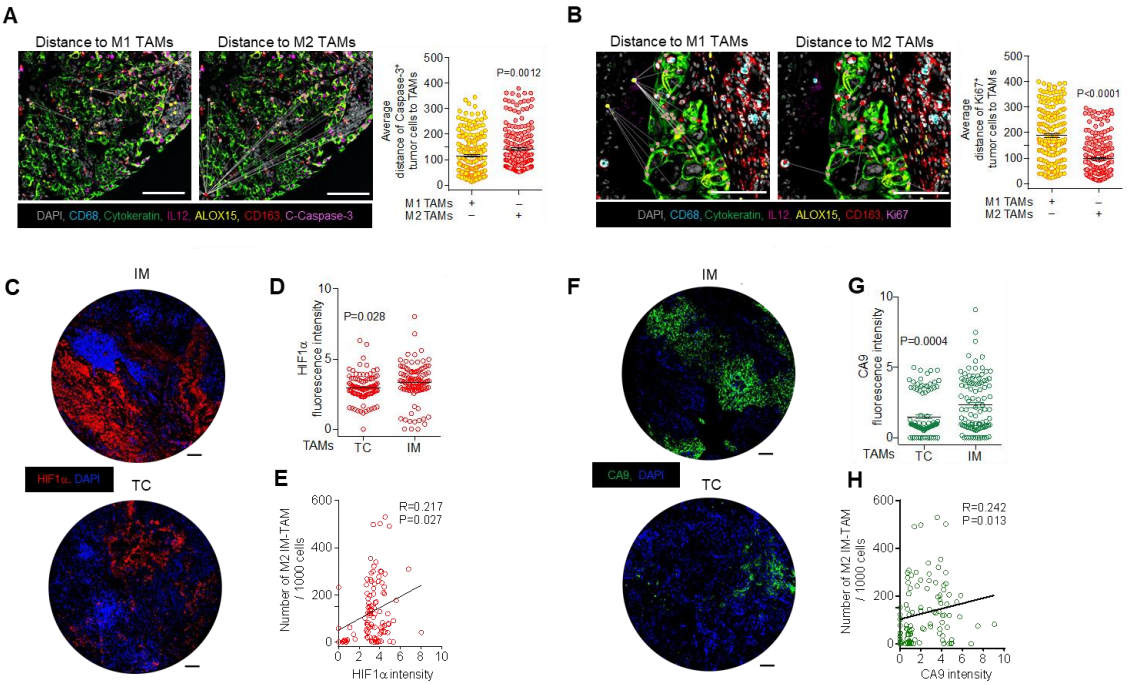

Figure 21 Proximity of tumor cells to TAMs directly affects tumor cell survival, and hypoxia contributes to the accumulation of M2 TAMs. A-B) Left panel: representative composite images, with pseudocolors showing staining against CD68 (cyan), Cytokeratin (green), IL12 (magenta), CD163 (red), ALOX15 (yellow), cleaved caspase-3 (A) / Ki67 (B) (pink), and DAPI (gray), showing the distance between caspase-3^+ (A) / $Ki67^+$ (B) tumor cells and M1/M2 TAMs. Scale bar, 100 µm. Right Panel: comparisons of the average distance between the caspase-3^+ (A)/$Ki67^+$ (B) cells and the M1 and M2 TAMs of the TMA cores. The data are presented as the mean ± standard error of the mean (SEM), and statistical significance was determined with an unpaired *t*-test; n = 104. Scale bar, 100 µm. (C) Representative immunofluorescence images of hypoxic marker HIF-1α in lung cancer tissues. Scale bar, 100 µm. (D) Bar plots showing the expression of HIF-1α in lung cancer tissues. Significance was determined with an unpaired *t*-test, and all data are presented as the mean ± SEM; n = 104. (E) Correlation between the expression pattern of HIF-1α and the density of M2-TAMs at the IM. Significance was determined with the Spearman's rank correlation; n = 104. (F) Representative immunofluorescence images of hypoxic marker CA9 in lung cancer tissues. Scale bar, 100 µm. (G) Bar plots showing the expression of CA9 in lung cancer tissues. Significance was determined with an unpaired *t*-test, and all data are presented as the mean ± SEM; n = 104. (H) Correlation between the expression pattern of CA9 and the density of M2-TAMs at the IM. Significance was determined with the Spearman's rank correlation; n = 104. Adapted from Zheng et al., 2020 [61]. License details and the terms and conditions provided by American Association for Cancer Research and Copyright Clearance Center. License Number: 4941411272697.

Discussion

This study identified four key findings. First, gene expression profiling showed marked differences among NMs, TC-TAMs and IM-TAMs. Second, M2 phenotypic predominance over M1 was observed, particularly at the IM, and hypoxia was associated with the accumulation of M2 TAMs. Third, M2 IM-TAMs were more proximal to tumor cells than M1 IM-TAMs, and the proximity of tumor cells to the different TAM phenotypes was correlated to tumor cell survival. Fourth, the reduced density of M1 TC-TAMs, increased proximity of tumor cells to M2 IM-TAMs, and reduced proximity of tumor cells to M1 IM-TAMs were independent lung cancer survival predictors.

By using human PBMC-derived and mouse bone marrow-derived macrophages, we showed antitumoral capability of M1 macrophages and protumoral feature of M2 macrophages. M1 macrophages were polarized by LPS and IFNγ, and M2 macrophages were polarized by IL4 for both human and mouse macrophages. Exploiting the differences in M1 and M2 macrophage biology using epigenetic modulators would provide strategies for targeting M2 TAMs, thereby eliminating their protumoral feature. TME is characterized by acidosis, hypoxia, elevated concentrations of IL4 and tumor-derived cytokines, suggesting IL4-induced M2 macrophages can partially mimic *in vivo* TME condition [171]. A comparable regulation of the phenotypic markers was observed in both classical cytokine-induced M1/M2 macrophages and *in vitro* coculture-generated M1/M2 TAMs [149]. In addition, compared with primary lung tissue-derived TAMs and *in vitro* coculture-generated TAMs, cytokine-induced macrophages are more easily obtained. Therefore, cytokine-induced classical M1/M2 macrophage were utilized for M1 and M2 gene expression profile and functional characterization. *In vivo*, we coinjected polarized bone marrow-derived macrophages with LLC1 cells to mice to evaluate the effect of M1 or M2 macrophages on tumor progression. We observed antitumoral role of M1 macrophages and protumoral feature of M2 macrophages. Protumoral feature of M2 macrophages was also observed in other tumor types. For instance, M2 macrophages significantly promote tumor growth compared with that of M1 macrophage in a murine xenograft colon cancer model transplanted with HCT116 cells [172].

RNA-seq is the gold standard for whole-transcriptome high-throughput data generation [173]. RNA-seq-based transcriptomics of macrophages enabled us to investigate the distribution and heterogeneity of macrophages among lung TC, IM and adjacent non-tumor tissues. A four-way plot deciphered the gene expression differences among NMs,

IM-TAMs and TC-TAMs based on the RNA-seq results. Gene expression of IM-TAMs and TC-TAMs relative to NMs revealed 835 and 651 genes that were exclusively highly expressed in IM-TAMs and TC-TAMs, respectively. The functions of some of the top differentially regulated genes are known, with respect to macrophage biology and TAM-tumor cell interaction. For instance, STK38 facilitates Smurf1-mediated MEKK2 ubiquitination and degradation, negatively regulating TLR9-mediated immune responses in macrophages [174]. HAMP is associated with TAM-regulated tumor iron homeostasis during breast cancer, supporting increased iron-targeting therapeutic approaches with regards to TAM modulation [175]. *CYP1B1* was expressed at a lower level in IM-TAMs than in TC-TAMs, and its deficiency is known to impair the phagocytic activity of macrophages [176]. Further investigation is required to determine the roles of the major spatial differential transcripts in TAM biology regarding their impact on the tumor microenvironment and cancer progression. Transcriptional signature of lung adenocarcinoma-derived TAMs is similar to that of lung squamous cell carcinoma-derived TAMs. Nevertheless, whether this observation regarding TAM spatial gene expression can be applied to additional cancer types requires further study. Despite heterogeneity of TAMs in different compartments of lung cancer, RNA-seq enables us to identify novel TAM subset-related prognostic markers. Whether some differentially regulated genes in TAMs are correlated with lung cancer survival needs sophisticated identification, including *CPD*, *SERPINB9*, *WARS*, *HIVEP1*, *PAG1*, *ERAP2*, *ACTR6*, *SPATA2*, *UBXN4*, *TMEM189*, *IQGAP2*, *SDF4*, *AP153*, *LRRFLP2*, *TM2D3*, *STK38*, *UBR2*, *IST1*, *MED16*, *METAP2*, *DBF4*, *PIHID1*, *ZNF37A*, *PUS7L*, *SEL61A*, *KMT2C*, *PLOD1*, *PACS2*, *BCL2L1*, *PAQR4*, *HAMP*, *MFSD12,* and *UBTD1*.

TAMs exhibit functional plasticity, with both antitumoral and protumoral effects, depending on a variety of external factors [177,178]. In addition to these opposing effects, the distribution of TAMs is another important factor to be considered when evaluating TAMs for the prediction of clinical outcomes [60]. To identify an association between TAM density and spatial distribution (TC and IM) and overall survival, TMAs were applied to current study. TMAs are relatively cost-effective and efficient, and are commonly used as high-throughput assays in histochemical studies, incorporating different tissues or tissue regions from different patients. However, it remains unclear whether TMA data are as reliable as whole tissue sections for clinicopathological correlations and survival. Therefore, to provide a satisfactory representation of the specimens, three punches

obtained from each TC and IM regions for individual patient sample (6 representative cores for each patient) were utilized to construct TMA in current study.

The precise identification of TAM phenotypes is challenging, because no single specific marker can distinguish M1 and M2 TAM subtypes. Previous study demonstrated that increasing tumor core $CD68^+$ cell density is significant independent predictor of the increased survival, while increasing stromal $CD68^+$ cell density is an independent predictor of the reduced survival of NSCLC patients [168]. However, CD68 is not exclusively expressed by macrophages, but also expressed by non-myeloid cell populations such as neutrophil granulocytes [179,180]. Hence, single marker CD68-based identification of TAM-related prognostic factors might be controversial. Additionally, most studies to date have used single or double immunostaining of macrophage markers, such as CD68, CD163 and HLA-DR, to identify TAMs [60,168,169,181-183]. An insufficient number of markers increases the possibility of misidentifying non-TAM populations as TAMs. Considering five markers as 100% specific, the specificity was decreased between 52-62% in three markers and 13-46% in four markers More precisely, five markers elevated the specificity of TAM identifications by approximately 57%, 52%, 62%, and 53% in comparison with CD68+IL12+ALOX15, CD68+IL12+CD163, CD68+CCR7+ALOX15, and CD68+CCR7+CD163-defined TAMs, respectively. Compared with four-marker defined M1/M2 TAMs, including CD68+CCR7+ALOX15+CD163, CD68+IL12+ALOX15+CD163, CD68+IL12+CCR7+ALOX15, and CD68+IL12+CCR7+CD163, five markers increased the specificity of TAM identifications by 46%, 13%, 32%, and 23%, respectively. These findings indicate that M1/M2 TAMs could be sufficiently distinguished from the non-M1/M2 population using five markers. Therefore, we used a combination of five markers to maximize the accuracy of TAM phenotype identification.

Multiplex immunohistochemistry-based analysis has been shown to provide unique insight into the spatial relationships among cells within the complex TME including infiltrating immune cells, cancer cells, and stromal cells. Conventional Immunofluorescence staining requires antibodies to be raised in different species of animals, which builds a hurdle to get robust staining of multiple biomarkers within a single tissue section. The Opal mutilplex is based on TSA, which makes similar species of antibodies amenable for multiplex staining on the same tissue section without cross-reactivity. But Opal staining protocols are labor-intensive, which can introduce the human

error and lead to staining variablility. Hence, to make Opal multiplex staining a clinical feasible tool, staining and imaging protocols need to be standardized, automated and validated. An accessible clinicaldiagnostic autostainer that is called Leica Bond Max was developed to standardize the production of high-quality, seven-color staining [184]. Currently, nine-color multiplex staining using the Opal system has been developed [146]. However, overheating the tissue with eight-color panel may lead to excessive epitope retrieval and eventually loss of signal with consecutive rounds of staining [185]. Thus, if additional biomarkers need to be stained on a single slide, alternative techniques are likely more appropriate, such as metal-base immunofluorescence staining and oligonucleotide-tag based strategies. In addition to robust multiplexed analysis (high-throughput technology to detect more than 50 biomarkers simultaneously in a single tissue sample), oligonucleotide-tag based CO detection by indEXing (CODEX) techniques provide comprehensive cellular spatial information, allowing greater insight into the pathogenesis of cancer and responsiveness to immunotherapy. Metal-based techniques take advantage of MS-based methods to interrogate the expression of multiple biomarkers simultaneously. Nevertheless, MS and DNA barcoding-based approaches require specialized equipment bioinformatics support for data management and analysis. Hence, Opal multiplex staining is practical in terms of cost-effectiveness, especially 3D imaging for multiplexing remains a promisingly new approach in the foreseeable future [140].

Previous studies demonstrated that hypoxia promotes M2 TAM infiltration and stabilizes the expression of HIF-1α, vascular endothelial growth factor, glucose transporter-1, Hippel-Lindau protein, and lactate dehydrogenase-A at IM compared with TC [178,186]. These findings are consistent with our observation, which M2 TAMs displayed a greater density at IM than at TC. Tumor hypoxia occurs when uncontrolled cell proliferation predominates, limiting the supply of oxygen and nutrition. In current study, we observed that more M2 TAMs accumulated at IM, which displayed an increased hypoxic status compared with TC. The density of M2 TAMs was positively correlated with the expression of the hypoxia markers CA9 and HIF-1α. Likewise, a significantly increased hypoxic status was observed at IM compared with TC for colorectal cancer [170]. Three plausible mechanisms could explain how hypoxia contributes to M2 TAM accumulation [92]. First, the hypoxic TME is enriched in cytokines, such as CCL2 and CSF1, which attract macrophages. Second, macrophage mobility is hampered within a hypoxic niche, due to hypoxia-dependent disruptions of the macrophage expression of CCR2, CCR5, and

neuropilin-1 (NRP1). Third, hypoxia promotes macrophages to express the protumoral phenotype, through the increased production of growth factors, such as VEGF, which supports tumor cell proliferation, and different matrix metalloproteinase, such as MMP7, to enhance tumor cell migration and invasion. Finally, TAMs might also directly contribute to the induction of tumor hypoxia, induced by the activation of AMP-activated protein kinase, which enhances the oxygen consumption rate in TAM mitochondria [187,188]. Patients with higher M1 TAM densities at both TC and IM, revealed significantly better overall survival rates. Lower densities of M2 IM-TAMs were associated with better survival in adenocarcinoma patients. Additionally, our results are consistent with previous studies, which demonstrated that a high M1 TC-TAM density was positively associated with better survival and that the infiltration of M2 TAMs was associated with reduced overall survival in lung cancer [60,169,181]. Besides, the lack of significance for TAM density as a predictor of survival in patients with large-cell carcinoma can be attributed to the limited number of samples of this tumor subtype in present study.

A detailed understanding of the TME landscape is needed in order to characterize the antitumoral immune response in lung cancer. The consideration of spatial proximity between tumor and immune cells is an essential step to delve into novel prognostic indicators. The proximity measurements performed in the current study shed light on the spatial TAM distribution. Patients with tumor cells that were more proximal to M1 TC-TAMs or more distant to M2 TC/IM-TAMs had higher overall survival rates. The multivariate analysis identified both M1 TC-TAM density and the proximity of tumor cells to M1/M2 IM-TAMs as independent predictors of survival. These results also indicate the reprogramming protumoral M2 TAMs to yield an antitumoral phenotype, or specifically depleting M2 TAMs could represent potentially effective therapeutic strategies for lung cancer [178]. A study assessed the intracellular metabolic configuration of different human immune cell populations at a single-cell resolution within TME [189]. This would enable characterization of the spatial distribution of immune cells with regards to metabolic signatures, contributing to further understanding of spatial metabolic configuration and additional prognostic factor identification. Aside from proximal distance between TAMs and tumor cells, the proximity between regulatory T cells and tumor cells is an independent predictor of a worse overall survival in lung cancer [190]. This suggests that precise analysis of cell-cell distances is essential for studying immune mediated responses. Therefore, further investigation on spatial proximity between tumor

and other immune cell types, such as dendritic cells and NK cells, and their potential as a prognostic factor is required. The analyzes of spatial context at single-cell proteome level among complex cellular phenotypes might require more robust techniques, such as mass spectrometry imaging (MSI). In MSI, a sample is physically scanned to produce a 3D image, in which each pixel is a MS signal with at least 1000 values and possibly more than 10^5 values. For instance, deep visual proteomics (DVP) combines high-resolution imaging, artificial intelligence (AI)-based image analysis for single-cell phenotyping based on multiplex staining and imaging with automated single cell laser microdissection, and ultrasensitive mass spectrometry workflow [191]. Analyses of normal vs. cancer regions using DVP will provide a spatial variability of cancer-related proteome, which will facilitate diagnostic biomarker identification. DVP will allow identify variations of protein abundance and spatial context among complex cellular phenotypes involved in the tumor response to treatments, which will strongly provide potential predictive biomarkers for personalized therapy. Even though multiplex staining does not cover proteome per se, it can facilitate more precise phenotyping and segmentation for MS analysis, which will allow unbiased characterization of proteome analyzes to be performed with retaining spatial information. In this case of scenario, spatial proteomic profiling of recurrent vs. non-recurrent lung cancer patient tissues will enable us to shed light on recurrence-related signature. This combination of multiplex staining with MS will also allow us to identify diagnostic biomarkers, subtypes of cancer (such as based on the patient phosphoproteome) and even rare populations of cells.

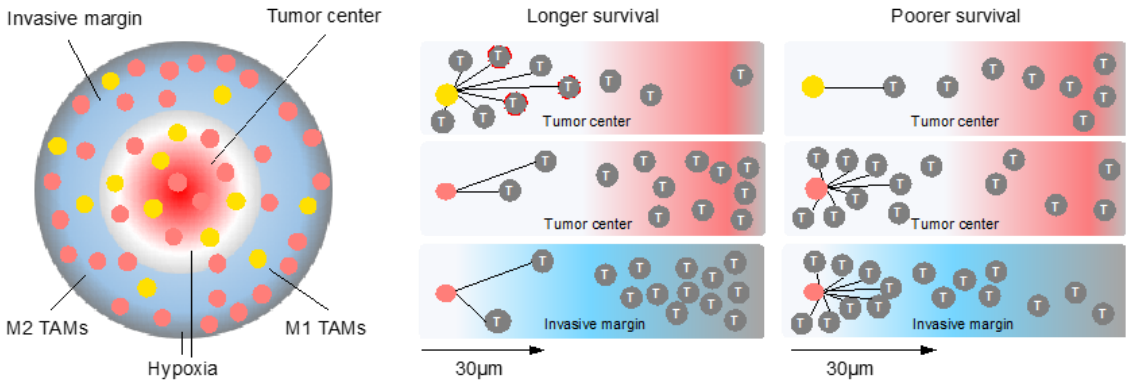

Figure 22 Schematic diagram of correlation of TAM spatial distribution with lung cancer survival. M2 IM-TAMs were more proximal to tumor cells than M1 IM-TAMs, and the proximity of tumor cells to the different TAM phenotypes directly influenced tumor cell survival. Hypoxia contributed to the accumulation of M2 TAMs. And the reduced M1 TC-TAMs, the increased proximity of tumor cells to M2 IM-TAMs, and the

reduced proximity of tumor cells to M1 IM-TAMs were independent lung cancer survival predictors.

In summary, the study underlines the significance of the density, spatial distribution and gene expression of TAM phenotypes as prognostic factors for overall survival in lung cancer. The multiplex profiling of macrophages in combination with other immune cells may facilitate the stratification of lung cancer patients (**Figure 22**). In addition, RNA-seq-based transcriptomics of macrophages may provide an effective tool for novel lung cancer prognostic marker identification. Focusing on the roles played by TAMs in TME may offer novel treatment strategies for lung cancer.

Outlook

Can we use RNA-seq-based transcriptomics of macrophages to identify novel lung cancer prognostic markers?

Having established the relevance of spatial TAM subset distribution in tumors, we wondered whether new prognostic markers would emerge from spatial RNA-seq-based transcriptomics of macrophages. To this end, we identified the top differentially expressed genes (DEGs; 50 from each group, in total 150 DEGs) from the RNA-seq analysis for IM-TAMs and TC-TAMs compared with those in NMs. Furthermore, we selected 48 out of the 150 DEGs using *in silico* analysis for relevance to cancer, microenvironment and cancer biology (**Figure 23A**).

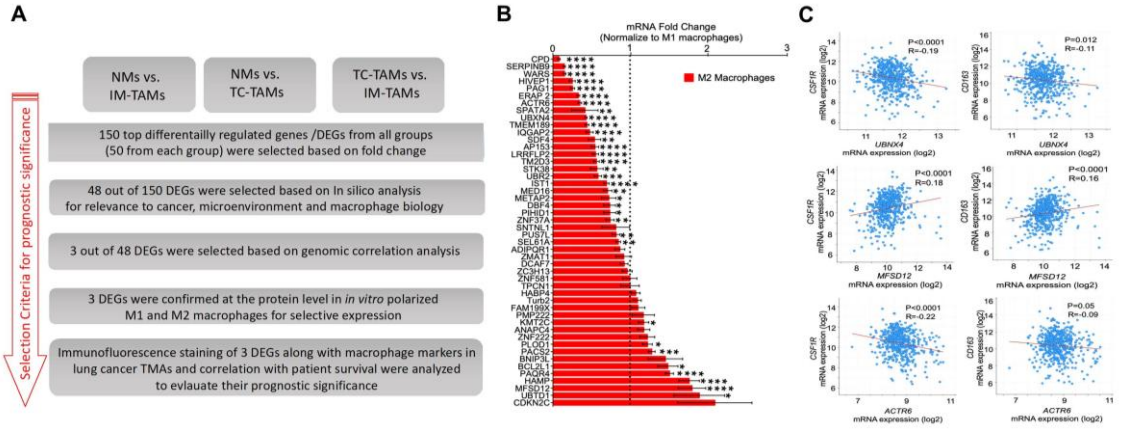

Figure 23 Selection criteria and expression of the top significantly differentially expressed genes in M1/M2 macrophages. (A) Flow chart shows selection criteria of targets from RNA-seq for prognostic significance. (B) qRT-PCR detection of the top 48 differentially expressed genes among NMs, TC-, and IM-TAMs, in PBMC-derived M1/M2 macrophages. Significance was determined with an the Mann-Whitney U test, and data are presented as the Mean (SD). *P < 0.05, ** P < 0.01; *** P < 0.001, n = 4. (C) The genomic correlation was performed using cBioPortal for Cancer Genomics. Normalized mRNA expression levels of the *CSF1R or CD163* genes from the Illumina HiSeq_RNASeqV2 of Lung Adenocarcinoma (TCGA, PanCancer Atlas), which includes 566 patient samples. Significance was determined using Pearson's correlation coefficient analysis.

In silico resources, such as The Human Protein Atlas and The Cancer Genome Atlas, and single-immune-cell transcriptomes in lung cancer [192] were analyzed for this selection. As a next step, we evaluated the mRNA expression of these top 48 DEGs in human peripheral blood monocyte-generated M1 and M2 macrophages. Compared with M1 macrophages, *CPD*, *SERPINB9*, *WARS*, *HIVEP1*, *PAG1*, *ERAP2*, *ACTR6*, *SPATA2*, *UBXN4*, *TMEM189*, *IQGAP2*, *SDF4*, *AP153*, *LRRFLP2*, *TM2D3*, *STK38*, *UBR2*, *IST1*, *MED16*, *METAP2*, *DBF4*, *PIHID1*, *ZNF37A*, *PUS7L*, and *SEL61A* were significantly downregulated in M2

macrophages, whereas *KMT2C*, *PLOD1*, *PACS2*, *BCL2L1*, *PAQR4*, *HAMP*, *MFSD12,* and *UBTD1* were significantly upregulated in M2 macrophages (**Figure 23B**). After confirming their expression in M1 and M2 macrophages, we determined the strength of correlations between each validated gene and TAM-related markers (*CSF1R* and *CD163*), using cBioPortal for Cancer Genomics (http://cbioportal.org) and Illumina HiSeq_RNASeqV2 of Lung Adenocarcinoma (TCGA, PanCancer Atlas) (**Figure 23C**) [193,194].

We identified that among the 48 DEGs, three displayed a strong correlation with TAM-related markers, namely, ACTR6, UBXN4 and MFSD12. ACTR6 (actin-related protein 6) and UBXN4 (UBX domain protein 4) were negatively correlated, whereas MFSD12 (major facilitator superfamily domain containing 12) was positively correlated with either CSF1R or CD163 (**Figure 23C**). However, the roles of ACTR6, UBXN4, and MFSD12 in cancer cell development and progression, and in macrophage biology, as well as their influences on the tumor microenvironment are not yet well-unknown. ACTR6 possesses an evolutionarily conserved role in heterochromatin formation, and high MFSD12 expression has been positively associated with shorter survival and lung metastasis in melanoma patients [195,196]. Moreover, immunocytochemistry confirmed that ACTR6 and UBXN4 were preferentially expressed in M1 macrophages, and MFSD12 was highly expressed in M2 macrophages at the protein level (**Figure 24A-C**). Therefore, Aside from spatial density and proximity of TAMs, we identified UBXN4, MFSD12, and ACTR6 as novel biomarkers that may serve as potential prognostic indicators for lung cancer patient survival. Sophisticated validation with larger cohort is required to ascertain UBXN4, MFSD12, and ACTR6 are lung cancer prognostic markers.

How UBXN4/ACTR6/MSFD12 expression influence on lung cancer progression and TAM biology?

To investigate UBXN4, ACTR6, and MFSD12 as potential lung cancer prognostic biomarkers, fluorescence staining was performed on the TMAs (**Figure 24D-F**). In a Kaplan–Meier analysis, high expression levels of UBXN4 at IM, high expression levels of ACTR6 at TC, and reduced expression levels of MSFD12 at TC were significantly associated with increased overall survival time among lung cancer patients (**Figure 24D-F**). Additionally, lung cancer patients with high expression levels of UBXN4 in $CD68^+$ cells at IM, and the increased production of ACTR6 in $CD68^+$ cells at either TC or IM

presented with significant overall survival benefits (**Figure 24D-F**). However, no significant association between the expression of MSFD12 in $CD68^+$ cells and overall survival was observed (**Figure 24E**). These findings indicate that the general expression of UBXN4 at IM, the expression of ACTR6/ MSFD12 at TC, and the $CD68^+$ cell expression of UBXN4 at IM and ACTR6 at either TC or IM are potential prognostic indicators for lung cancer patient survival. However, the mechanisms through which UBXN4/ACTR6/MSFD12 expression influence on lung cancer progression and TAM biology is in need of further investigation.

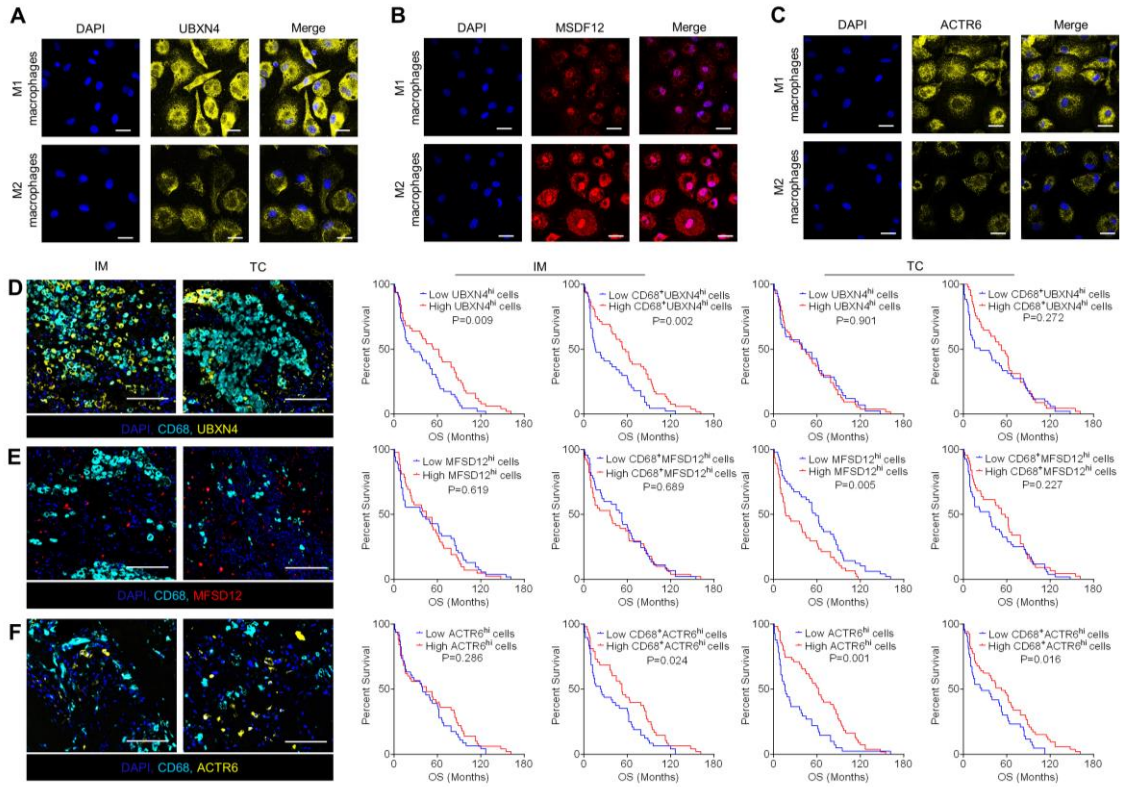

Figure 24 Kaplan-Meier survival analyzes of UBXN4, MFSD12 and ACTR6 expression-related parameters in lung cancer patients. (A-C) Fluorescence microscopy of in peripheral blood monocyte-derived macrophages. The expression of UBXN4 (yellow) (A), MFSD12 (Red) (B), and ACTR6 (yellow) (C) in M1/M2 macrophages were determined by fluorescence immunocytochemistry. Cell nuclei were stained with DAPI (blue). Scale bar, 20 μm. (D-F) representative composite images of the TMA showing the expression of UBXN4 (yellow) (D), MFSD12 (Red) (E), and ACTR6 (yellow) (F). CD68 is illustrated in cyan, and nuclei were stained with DAPI (blue). Scale bar, 100 μm. Survival curves are illustrated according to the expression status of UBXN4 (D), MFSD12 (E) and ACTR6 (F) either in all cell populations or only in CD68+ cells (low density vs. high density), at IM (middle panel of each subfigure) or TC (right panel of each subfigure) of lung cancer specimens. P-values reflect comparisons between two groups by univariate analysis, using the log-rank test, n = 104.

Can proximity distance between lung cancer cells and other immune cell types predict lung cancer survival?

We showed proximity of tumor cells to TAMs directly affected tumor cell survival. Proximity of tumor cells to M1/M2 IM-TAMs was an independent predictor of overall survival of lung cancer. Additionally, high infiltration of cytotoxic T cells in the vicinity of cancer cells significantly correlated with prolonged patient survival in pancreatic ductal adenocarcinoma [197]. Proximal distance between regulatory T cells and tumor cells is an independent predictor of worse overall survival in lung cancer [190]. In a breast cancer 3D co-culture model, proximal distance between cancer cells and CAFs tended to have better response to neoadjuvant lapatinib therapy as assessed by a reduction in tumor size [198]. To understand TME landscape further, we need to figure out the spatial proximity of tumor cells and other immune cells such as dendritic cells, neutrophil and NK cells and their association with lung cancer survival.

Can we elevate M1 TAM proportion by some clinically feasible approaches?

Antitumoral therapeutic strategies targeting TAMs include lowering TAM survival, reducing macrophage recruitment and switching M2 TAMs into M1-like phenotype. Among these strategies, reverting M2 TAMs to the antitumoral phenotype by modulating the TME is most promising because phenotypes of macrophages are highly sensitive to stimuli within the TME. Of note, promoting the generation of M1 macrophages from monocytes also can be a feasible method for accumulating of tumoricidal effectors at tumor sites to slow progression of the cancer. Although increasing the circulating level of monocyte chemoattractant protein-1 (MCP-1) to a threshold level enhances the antitumoral effects of suicide gene therapy against hepatocellular carcinoma via M1 macrophage activation, it is unclear whether M1 activation is due to M2 TAM repolarization or promotion of monocytes to differentiate to M1 macrophages because monocyte recruitment depends on the level of MCP-1 secreted by tumor cells [199]. Therefore, further investigations would be worthwhile to identify more effective approaches to elevate ratio of M1 to M2 TAMs to prevent tumor progression and recurrence. Several therapeutic drugs targeting TAMs are currently available for clinical use. For instance, the agent trabectedin lowers TAM survival [103] and alemtuzumab eliminates TAMs by targeting a TAM surface protein [119]. However, the efficacy of such

cancer therapy must be improved via the development of additional agents that are more specific to TAMs and less cytotoxic.

Can we specifically target activated TAMs *in vivo*?

It has been an ongoing challenge to transport drugs to specific cell types during cancer treatment. Systems to deliver liposomes, micelles and microspheres have been developed to enhance drug efficacy. Micelles are in the 1- to 100-nm size range, whereas liposome diameters vary from 400 to 2500 nm [200]. Macrophages are professional phagocytes and thus have superior capacity to engulf micelles and liposomes. Consequently, nanoparticle and liposome formulations have been developed to transport antitumoral drugs by TAMs with high specificity and low toxicity to the organism. Micelles are used in different formulations ranging from solid lipid micelles (SLNs) to polymer-, gold- or albumin-based micelles. To date, several nanoparticle formulations have shown clinical feasibility, including solid lipid micelles loaded with the topoisomerase inhibitor mitoxantrone, polymer micelles loaded with the antitumoral agents cisplatin and cyclodextrin and the albumin nanoparticle–based Abraxane [200,201]. Since folate receptor beta (FRβ) is specifically expressed by the activated macrophages and binds to folic acid (FA) and folate-linked molecules with high affinity, FA coupled poly(L-lactide)-b-poly(ethylene glycol) (FA-PEG-PLLA) micelles which encapsulate nucleic acids in their core while they are shielded with PEG on their surface were applied in order to deliver drugs more selectively to activated macrophages[202,203]. Furthermore, FRβ also transports these molecules into cells by receptor-mediated endocytosis.

Liposomes contain a phospholipid bilayer to which additional molecules can easily be added, and small liposomes (50–100 nm) that have been negatively charged by introducing negatively charged lipids such as phosphatidylserine and phosphatidylglycerol are preferably engulfed by macrophages [204]. In addition, it has been observed that ligand-containing liposomes are more efficiently engulfed than those without ligand [205]. Specifically, liposomes conjugated with a peptide (GGPNLTGRW or RGD) selectively target integrin receptors of monocytes [206]. Liposomes coated with antibodies (immunoliposomes) are able to bind to the Fc receptors of macrophages. For example, CD163 antibody–coated liposomes can be used to target M2 macrophages [207]. Moreover, mannosylated liposomes, which target lectin receptors of macrophages and DCs, have been developed to transport antitumoral agents such as CpG-ODN and DNA

[208]. Liposomal Doxil and abovementioned liposomal clodronate are successful examples of a liposome-based cancer treatment with low toxicity and high specificity [104,200]. Although liposome-mediated depletion of TAMs has been demonstrated, whether liposome-encapsulated agents can effectively facilitate M2 TAM repolarization still requires further investigation.

Although a 100% efficient receptor blockade, as could be achieved with a genetic knockout in mice, is unlikely to achieve the general pharmacodynamic and kinetic properties of xenobiotics, it would be useful for identifying key differentiators of the M2 macrophage lineage. To target TAMs more effectively, we must identify key differentiators of the M2 macrophage lineage or monocyte to M1 macrophage lineage. Besides, more *in vivo* studies are required to evaluate the toxicity and efficacy of micells and liposome-based cancer treatment. Selective targeting of TAM metabolism *in vivo* is an ongoing challenge. As mentioned previously, cichloroacetate exhibits potential in TAM M2-to-M1 reprogramming. However, dichloroacetate also inhibits aerobic glycolysis and induces differentiation of Tregs, which might result in decreased immunosurveillance in cancer therapy [209]. Hence, the therapeutic potential of dichloroacetate might be hampered in the absence of a specific TAM-targeting strategy. Although nanoparticle and liposome-based systems aid in efficient drug delivery to TAMs the dynamic ability of TAMs to adapt to a specific microenvironment increases the difficulty for *in vivo* metabolic targeting. Therefore, investigations into the metabolic features of TAMs at a spatial and temporal resolution using specialized experimental technologies such as *in vivo* tracer analysis and single-cell technologies would offer more precise guidance for metabolic regulation [210]. Furthermore, depletion of TAMs generates a less hypoxic TME and reduces tumor glycolysis, leading to increased PD-L1 expression in tumors. As some patients with lung cancer acquire resistance to immune checkpoint therapies and some groups do not respond [211], a combination of immunotherapeutic agents such as PD-L1 inhibitors and TAM metabolic interventions could be beneficial for cancer therapy. Investigations of genetic and epigenetic mechanisms of macrophage heterogeneity and polarization will establish a foundation for macrophage phenotype reversion strategies. Owing to the diversity of macrophages within the TME, more macrophage markers (especially function-related) that are specific to individual macrophage subsets need to be identified to facilitate a better elucidating of the mechanisms of spatiotemporal modulation of macrophage polarization and repolarization.

In addition, because TAM infiltration is associated with poor patient outcomes, systematic and well-defined criteria for the evaluation of macrophage populations are required for practical TAM-targeting diagnostic and therapeutic strategies.

How can we apply multiplex staining to improve personalized cancer therapy?

Personalized therapy is conducive to treatment of lung cancer which is with a high mutational burden that is reported to be associated with increased immunogenic neoantigen generation and better response rates to immune checkpoint inhibitors (ICIs). Multiplex staining linked with proteome profiling will allow us to better screen drug and identify patients who will respond to proposed therapies. Firstly, analyses of human normal vs. lung cancer sections using multiplex staining-linked proteome profiling will provide a spatial variability of lung cancer-related proteome, which will facilitate diagnostic, prognostic and therapeutic biomarker identification. Secondly, to understand the mechanism underlying lung cancer patients respond to ICIs, lung cancer cases with ICI treatment can be classified to response vs. nonresponse groups. Multiplex staining-combined proteomic analysis will enable us to identify variations of protein abundance and spatial context among complex cellular phenotypes involved in the tumor response to ICIs from different perspectives (response vs. nonresponse, pretreatment vs. posttreatment). This study will strongly provide potential predictive biomarkers for personalized therapy. Thirdly, recent studies have demonstrated DNA damage response inhibitors (DDRi) and histone deacetylase inhibitors (HDACi) displayed suppressive effects on small cell lung cancer progression. Whether ICIs in combination with DDRi or HDACi will exhibit a synergistic effect can be screened in humanized murine models. Multiplex staining-combined proteomic analysis will allow us to understand how the DDRi/HDACi treatments change the status of immune activity for drug screening in SCLC patients with identification of therapeutically relevant proteins and pathways at single-cell resolution. Last but not least, multi-omics characterizations, such as RNA-seq and ATAC-seq, in combination with multiplex staining-linked proteome profiling, will facilitate comprehension of not only spatial proteome variations which include post-translational modifications, but also transcriptome and epigenetic landscape alterations. Hence, we will be able to investigate more fully the mechanisms underlying drug (i.e. ICIs) response and screening as well as biomarker identification to propose potential

personalized strategies to improve therapy efficacy for poor responders in lung cancer as well as other cancer types.

Summary

Lung cancer is one of the most common cancers in terms of incidence and mortality around the world. Recent researches highlighted the importance of the tumor microenvironment for progression and metastasis of most known cancer types. Macrophages play complex roles in cancer, including the antitumoral and protumoral roles of M1 and M2 tumor-associated macrophages (TAMs), respectively. However, density and topology of distinct TAM phenotypes at tumor center (TC) versus invasive margin (IM) and epigenetic mechanisms of macrophage polarization and repolarization require further investigation in lung cancer. Here we investigated TAM-subtype density and distribution between the TC and IM in human lung cancer and TAMs associations with overall survival. We isolated macrophages from adjacent non-tumor tissue (NM), the TC (TC-TAMs) and the IM (IM-TAMs) and analyzed with RNA sequencing (RNA-seq). Lung-tumor tissue microarrays, including IM and TC, from 104 patient samples were constructed. M1 and M2 TAMs were identified using multiplex immunofluorescence staining, and a tumor cell-TAM proximity analysis was performed. Gene expression profiling demonstrated marked differences among NMs, TC-TAMs and IM-TAMs. Significantly differentially regulated genes included *CPD*, *SERPINB9*, *WARS*, *HIVEP1*, *PAG1*, *ERAP2*, *ACTR6*, *SPATA2*, *UBXN4*, *TMEM189*, *IQGAP2*, *SDF4*, *AP153*, *LRRFLP2*, *TM2D3*, *STK38*, *UBR2*, *IST1*, *MED16*, *METAP2*, *DBF4*, *PIHID1*, *ZNF37A*, *PUS7L*, *SEL61A*, *KMT2C*, *PLOD1*, *PACS2*, *BCL2L1*, *PAQR4*, *HAMP*, *MFSD12,* and *UBTD1*. Based on a panel of five selected markers (CD68, IL12, CCR7, CD163, and ALOX15), M2 predominance over M1 and M2 proximity to tumor cells was observed, especially at the IM. Mechanistically, the tumor cell proximity to TAMs was linked with tumor cell survival, and hypoxia contributed to M2 TAM accumulation. Notably, lower density of M1 TC-TAMs and higher proximity of tumor cells to M2 IM-TAMs or lower proximity to M1 IM-TAMs were linked with poor survival. Together, our results revealed the marked heterogeneity of TAM populations in different tumor regions. M2 predominance and juxtaposition of M2 TAMs near tumor cells were associated with poor survival.

Zusammenfassung

Lungenkrebs ist eine der häufigsten Krebsarten in Bezug auf Inzidenz und Sterblichkeit weltweit. In den letzten Jahrzehnten wurde die Bedeutung der Tumormikroumgebung für die Progression und Metastasierung der meisten bekannten Krebsarten immer deutlicher. Dabei nehmen Makrophagen eine komplexe Rolle bei Krebserkrankungen ein. Dies beinhaltet die antitumorale Rolle von M1- und die protumorale Rolle von M2-tumorassoziierten Makrophagen (TAMs). Die Dichte und die Topologie verschiedener TAM-Phänotypen im Tumorzentrum (Tumor Center, TC) gegenüber invasiver Randlagen (Invasive Margin, IM), sowie epigenetische Mechanismen der Polarisation und Repolarisation erfordern jedoch weitere Untersuchungen bei Lungenkrebs. Hier verglichen wir die Dichte und Verteilung der TAM-Unterarten zwischen TC und IM bei humanem Lungenkrebs, sowie TAMs-Assoziationen mit dem Gesamtüberleben. Wir isolierten Makrophagen aus angrenzendem Nicht-Tumorgewebe (NM), dem TC (TC-TAMs) und dem IM (IM-TAMs) und analysierten diese mittels RNA-Sequenzierung (RNA-seq). Es wurden Mikroarrays von Lungentumorgewebe, einschließlich IM und TC, aus 104 Patientenproben erstellt. Dabei wurden M1- und M2-TAMs mittels Multiplex-Immunfluoreszenzfärbung identifiziert und eine Nachbarschaftsanalyze von Tumorzellen und TAMs durchgeführt. Die Profilerstellung für die Genexpression zeigte deutliche Unterschiede zwischen NMs, TC-TAMs und IM-TAMs. Unter den signifikant differenziell regulierten Genen waren *CPD*, *SERPINB9*, *WARS*, *HIVEP1*, *PAG1*, *ERAP2*, *ACTR6*, *SPATA2*, *UBXN4*, *TMEM189*, *IQGAP2*, *SDF4*, *AP153*, *LRRFLP2*, *TM2D3*, *STK38*, *UBR2*, *IST1*, *MED16*, *METAP2*, *DBF4*, *PIHID1*, *ZNF37A*, *PUS7L*, *SEL61A*, *KMT2C*, *PLOD1*, *PACS2*, *BCL2L1*, *PAQR4*, *HAMP*, *MFSD12* und *UBTD1*. Basierend auf einem Panel aus fünf ausgewählten Markern (CD68, IL12, CCR7, CD163 und ALOX15) wurde eine Prädominanz von M2- gegenüber M1-TAMs, sowie eine Nähe von M2-TAMs zu Tumorzellen beobachtet, insbesondere am IM. Mechanistisch war die Tumorzellnähe zu TAMs mit dem Überleben von Tumorzellen verbunden, und Hypoxie trug zu einer M2-TAM-Akkumulation bei. Insbesondere die geringere Dichte von M1 TC-TAMs und die größere Nähe von Tumorzellen zu M2 IM-TAMs oder eine geringere Nähe zu M1 IM-TAMs waren mit einem schlechten Überleben verbunden. Zusammenfassend zeigten unsere Ergebnisse die ausgeprägte Heterogenität von TAM-Populationen in den verschiedenen Tumorregionen.

References

1. Ferlay, J*., et al.* Estimating the global cancer incidence and mortality in 2018: GLOBOCAN sources and methods. *Int J Cancer* **144**, 1941-1953 (2019).
2. Brody, H. Lung cancer. *Nature* **513**, S1-S48 (2014).
3. Inamura, K. Lung Cancer: Understanding Its Molecular Pathology and the 2015 WHO Classification. *Front Oncol* **7**, 193 (2017).
4. Morgensztern, D., Ng, S.H., Gao, F. & Govindan, R. Trends in stage distribution for patients with non-small cell lung cancer: a National Cancer Database survey. *J Thorac Oncol* **5**, 29-33 (2010).
5. Rodriguez-Canales, J., Parra-Cuentas, E. & Wistuba, I.I. Diagnosis and Molecular Classification of Lung Cancer. *Cancer Treat Res* **170**, 25-46 (2016).
6. Fujimoto, J. & Wistuba, II. Current concepts on the molecular pathology of non-small cell lung carcinoma. *Semin Diagn Pathol* **31**, 306-313 (2014).
7. Bergethon, K*., et al.* ROS1 rearrangements define a unique molecular class of lung cancers. *J Clin Oncol* **30**, 863-870 (2012).
8. Vaishnavi, A*., et al.* Oncogenic and drug-sensitive NTRK1 rearrangements in lung cancer. *Nature medicine* **19**, 1469-1472 (2013).
9. Yang, Y., Xie, Y. & Xian, L. Breast cancer susceptibility gene 1 (BRCA1) predict clinical outcome in platinum- and toxal-based chemotherapy in non-small-cell lung cancer (NSCLC) patients: a system review and meta-analysis. *J Exp Clin Cancer Res* **32**, 15 (2013).
10. Gong, W*., et al.* RRM1 expression and clinical outcome of gemcitabine-containing chemotherapy for advanced non-small-cell lung cancer: a meta-analysis. *Lung Cancer* **75**, 374-380 (2012).
11. Goldstraw, P*., et al.* The IASLC Lung Cancer Staging Project: Proposals for Revision of the TNM Stage Groupings in the Forthcoming (Eighth) Edition of the TNM Classification for Lung Cancer. *J Thorac Oncol* **11**, 39-51 (2016).
12. Kuo, S.W*., et al.* Prognostic significance of histologic differentiation, carcinoembryonic antigen value, and lymphovascular invasion in stage I non-small cell lung cancer. *J Thorac Cardiovasc Surg* **148**, 1200-1207 e1203 (2014).
13. Woodard, G.A., Jones, K.D. & Jablons, D.M. Lung Cancer Staging and Prognosis. *Cancer Treat Res* **170**, 47-75 (2016).
14. Alberg, A.J., Brock, M.V., Ford, J.G., Samet, J.M. & Spivack, S.D. Epidemiology of lung cancer: Diagnosis and management of lung cancer, 3rd ed: American College of Chest Physicians evidence-based clinical practice guidelines. *Chest* **143**, e1S-e29S (2013).
15. Cote, M.L*., et al.* Increased risk of lung cancer in individuals with a family history of the disease: a pooled analysis from the International Lung Cancer Consortium. *Eur J Cancer* **48**, 1957-1968 (2012).
16. Field, R.W. & Withers, B.L. Occupational and environmental causes of lung cancer. *Clin Chest Med* **33**, 681-703 (2012).
17. Lorigan, P., Radford, J., Howell, A. & Thatcher, N. Lung cancer after treatment for Hodgkin's lymphoma: a systematic review. *Lancet Oncol* **6**, 773-779 (2005).
18. Shcherba, M., Shuter, J. & Haigentz, M., Jr. Current questions in HIV-associated lung cancer. *Curr Opin Oncol* **25**, 511-517 (2013).
19. Brenner, D.R*., et al.* Previous lung diseases and lung cancer risk: a pooled analysis from the International Lung Cancer Consortium. *Am J Epidemiol* **176**, 573-585 (2012).
20. Sequist, L.V*., et al.* Genotypic and histological evolution of lung cancers acquiring resistance to EGFR inhibitors. *Sci Transl Med* **3**, 75ra26 (2011).
21. Chen, Z., Fillmore, C.M., Hammerman, P.S., Kim, C.F. & Wong, K.K. Non-small-cell lung cancers: a heterogeneous set of diseases. *Nat Rev Cancer* **14**, 535-546 (2014).
22. Obeid, J.M., Wages, N.A., Hu, Y., Deacon, D.H. & Slingluff, C.L., Jr. Heterogeneity of CD8(+) tumor-infiltrating lymphocytes in non-small-cell lung cancer: impact on patient prognostic assessments and comparison of quantification by different sampling strategies. *Cancer Immunol Immunother* **66**, 33-43 (2017).
23. Yoshida, G.J. The heterogeneity of cancer stem-like cells at the invasive front. *Cancer Cell Int* **17**, 23 (2017).
24. Hanahan, D. & Weinberg, R.A. Hallmarks of cancer: the next generation. *Cell* **144**, 646-674 (2011).
25. Hui, L. & Chen, Y. Tumor microenvironment: Sanctuary of the devil. *Cancer letters* **368**, 7-13 (2015).
26. Orimo, A*., et al.* Stromal fibroblasts present in invasive human breast carcinomas promote tumor

growth and angiogenesis through elevated SDF-1/CXCL12 secretion. *Cell* **121**, 335-348 (2005).
27. Silzle, T*., et al.* Tumor-associated fibroblasts recruit blood monocytes into tumor tissue. *European journal of immunology* **33**, 1311-1320 (2003).
28. Comito, G*., et al.* Cancer-associated fibroblasts and M2-polarized macrophages synergize during prostate carcinoma progression. *Oncogene* **33**, 2423-2431 (2014).
29. Kobayashi, N*., et al.* Hyaluronan deficiency in tumor stroma impairs macrophage trafficking and tumor neovascularization. *Cancer research* **70**, 7073-7083 (2010).
30. Martinez-Outschoorn, U.E*., et al.* Autophagy in cancer associated fibroblasts promotes tumor cell survival: Role of hypoxia, HIF1 induction and NFkappaB activation in the tumor stromal microenvironment. *Cell cycle* **9**, 3515-3533 (2010).
31. Katz, S.G. & Rabinovich, P.M. T Cell Reprogramming Against Cancer. *Methods in molecular biology* **2097**, 3-44 (2020).
32. Xia, A., Zhang, Y., Xu, J., Yin, T. & Lu, X.J. T Cell Dysfunction in Cancer Immunity and Immunotherapy. *Frontiers in immunology* **10**, 1719 (2019).
33. Lanier, L.L. NK cell recognition. *Annu Rev Immunol* **23**, 225-274 (2005).
34. Moretta, L*., et al.* Human NK cells and their receptors. *Microbes Infect* **4**, 1539-1544 (2002).
35. Hallner, A*., et al.* The HLA-B-21 dimorphism impacts on NK cell education and clinical outcome of immunotherapy in acute myeloid leukemia. *Blood* **133**, 1479-1488 (2019).
36. Lv, M., Wang, K. & Huang, X.J. Myeloid-derived suppressor cells in hematological malignancies: friends or foes. *Journal of hematology & oncology* **12**, 105 (2019).
37. Umemura, N*., et al.* Tumor-infiltrating myeloid-derived suppressor cells are pleiotropic-inflamed monocytes/macrophages that bear M1- and M2-type characteristics. *Journal of leukocyte biology* **83**, 1136-1144 (2008).
38. Lindau, D., Gielen, P., Kroesen, M., Wesseling, P. & Adema, G.J. The immunosuppressive tumour network: myeloid-derived suppressor cells, regulatory T cells and natural killer T cells. *Immunology* **138**, 105-115 (2013).
39. Sinha, P., Clements, V.K., Bunt, S.K., Albelda, S.M. & Ostrand-Rosenberg, S. Cross-Talk between Myeloid-Derived Suppressor Cells and Macrophages Subverts Tumor Immunity toward a Type 2 Response. *The Journal of Immunology* **179**, 977-983 (2007).
40. Fridlender, Z.G. & Albelda, S.M. Tumor-associated neutrophils: friend or foe? *Carcinogenesis* **33**, 949-955 (2012).
41. Fridlender, Z.G*., et al.* Polarization of tumor-associated neutrophil phenotype by TGF-beta: "N1" versus "N2" TAN. *Cancer cell* **16**, 183-194 (2009).
42. Queen, M.M., Ryan, R.E., Holzer, R.G., Keller-Peck, C.R. & Jorcyk, C.L. Breast cancer cells stimulate neutrophils to produce oncostatin M: potential implications for tumor progression. *Cancer research* **65**, 8896-8904 (2005).
43. Rigoni, A., Colombo, M.P. & Pucillo, C. The Role of Mast Cells in Molding the Tumor Microenvironment. *Cancer microenvironment : official journal of the International Cancer Microenvironment Society* **8**, 167-176 (2015).
44. Khan, M.W*., et al.* PI3K/AKT signaling is essential for communication between tissue-infiltrating mast cells, macrophages, and epithelial cells in colitis-induced cancer. *Clinical cancer research : an official journal of the American Association for Cancer Research* **19**, 2342-2354 (2013).
45. Zheng, X*., et al.* Redirecting tumor-associated macrophages to become tumoricidal effectors as a novel strategy for cancer therapy. *Oncotarget* (2017).
46. Mimura, K., Kono, K., Takahashi, A., Kawaguchi, Y. & Fujii, H. Vascular endothelial growth factor inhibits the function of human mature dendritic cells mediated by VEGF receptor-2. *Cancer Immunology Immunotherapy* **56**, 761-770 (2007).
47. Ruffell, B*., et al.* Macrophage IL-10 blocks CD8+ T cell-dependent responses to chemotherapy by suppressing IL-12 expression in intratumoral dendritic cells. *Cancer cell* **26**, 623-637 (2014).
48. Wynn, T.A., Chawla, A. & Pollard, J.W. Macrophage biology in development, homeostasis and disease. *Nature* **496**, 445-455 (2013).
49. Mass, E*., et al.* Specification of tissue-resident macrophages during organogenesis. *Science* **353**(2016).
50. Gordon, S. & Taylor, P.R. Monocyte and macrophage heterogeneity. *Nature Reviews Immunology* **5**, 953-964 (2005).
51. Franklin, R.A*., et al.* The cellular and molecular origin of tumor-associated macrophages. *Science* **344**, 921-925 (2014).

52. Tymoszuk, P*., et al.* In situ proliferation contributes to accumulation of tumor-associated macrophages in spontaneous mammary tumors. *European journal of immunology* **44**, 2247-2262 (2014).
53. Shand, F.H*., et al.* Tracking of intertissue migration reveals the origins of tumor-infiltrating monocytes. *Proceedings of the National Academy of Sciences of the United States of America* **111**, 7771-7776 (2014).
54. Stout, R.D*., et al.* Macrophages Sequentially Change Their Functional Phenotype in Response to Changes in Microenvironmental Influences. *Journal of Immunology* **175**, 342-349 (2005).
55. Lavin, Y*., et al.* Tissue-resident macrophage enhancer landscapes are shaped by the local microenvironment. *Cell* **159**, 1312-1326 (2014).
56. Xue, J*., et al.* Transcriptome-based network analysis reveals a spectrum model of human macrophage activation. *Immunity* **40**, 274-288 (2014).
57. Biswas, S.K. & Mantovani, A. Macrophage plasticity and interaction with lymphocyte subsets: cancer as a paradigm. *Nature Immunology* **11**, 889-896 (2010).
58. Duluc, D*., et al.* Interferon-gamma reverses the immunosuppressive and protumoral properties and prevents the generation of human tumor-associated macrophages. *International journal of cancer* **125**, 367-373 (2009).
59. Murray, P.J*., et al.* Macrophage activation and polarization: nomenclature and experimental guidelines. *Immunity* **41**, 14-20 (2014).
60. Ma, J*., et al.* The M1 form of tumor-associated macrophages in non-small cell lung cancer is positively associated with survival time. *BMC cancer* **10**, 112 (2010).
61. Zheng, X*., et al.* Spatial Density and Distribution of Tumor-Associated Macrophages Predict Survival in Non–Small Cell Lung Carcinoma. *Cancer research* **80**, 4414–4425 (2020).
62. Laoui, D*., et al.* Tumor-associated macrophages in breast cancer: distinct subsets, distinct functions. *International Journal of Developmental Biology* **55**, 861-867 (2011).
63. Olesch, C*., et al.* MPGES-1-derived PGE2 suppresses CD80 expression on tumor-associated phagocytes to inhibit anti-tumor immune responses in breast cancer. *Oncotarget* **6**, 10284-10296 (2015).
64. Van Overmeire, E*., et al.* M-CSF and GM-CSF Receptor Signaling Differentially Regulate Monocyte Maturation and Macrophage Polarization in the Tumor Microenvironment. *Cancer research* **76**, 35-42 (2016).
65. Helm, O*., et al.* Tumor-associated macrophages exhibit pro- and anti-inflammatory properties by which they impact on pancreatic tumorigenesis. *International journal of cancer* **135**, 843-861 (2014).
66. Reinartz, S*., et al.* Mixed-polarization phenotype of ascites-associated macrophages in human ovarian carcinoma: correlation of CD163 expression, cytokine levels and early relapse. *International journal of cancer* **134**, 32-42 (2014).
67. Williams, C.N., Hodges, D.B., Reynolds, J.M. & Bhat, A. Tumor-associated macrophages: CD206 and CD68 expression and patient outcomes in locally advanced breast cancer. **36**, e24130-e24130 (2018).
68. E, S*., et al.* Identification of tumor-associated macrophage subsets that are associated with breast cancer prognosis. *Clin Transl Med* **10**, e239 (2020).
69. Movahedi, K*., et al.* Different tumor microenvironments contain functionally distinct subsets of macrophages derived from Ly6C(high) monocytes. *Cancer research* **70**, 5728-5739 (2010).
70. Joshi, S., Singh, A.R., Zulcic, M. & Durden, D.L. A macrophage-dominant PI3K isoform controls hypoxia-induced HIF1alpha and HIF2alpha stability and tumor growth, angiogenesis, and metastasis. *Molecular Cancer Research* **12**, 1520-1531 (2014).
71. Casazza, A*., et al.* Impeding macrophage entry into hypoxic tumor areas by Sema3A/Nrp1 signaling blockade inhibits angiogenesis and restores antitumor immunity. *Cancer Cell* **24**, 695-709 (2013).
72. Zhang, J*., et al.* Tumor hypoxia enhances Non-Small Cell Lung Cancer metastasis by selectively promoting macrophage M2 polarization through the activation of ERK signaling. *Oncotarget* **5**, 9664-9677 (2014).
73. Donnem, T*., et al.* Stromal CD8(+) T-cell Density-A Promising Supplement to TNM Staging in Non-Small Cell Lung Cancer. *Clinical Cancer Research* **21**, 2635-2643 (2015).
74. Yang, M., McKay, D., Pollard, J.W. & Lewis, C.E. Diverse Functions of Macrophages in Different Tumor Microenvironments. *Cancer research* **78**, 5492-5503 (2018).

75. Huang, Y.K., *et al.* Macrophage spatial heterogeneity in gastric cancer defined by multiplex immunohistochemistry. *Nat Commun* **10**, 3928 (2019).
76. Lavin, Y., *et al.* Innate Immune Landscape in Early Lung Adenocarcinoma by Paired Single-Cell Analyses. *Cell* **169**, 750-765 e717 (2017).
77. Gentles, A.J., *et al.* The prognostic landscape of genes and infiltrating immune cells across human cancers. *Nat Med* **21**, 938-945 (2015).
78. Fridman, W.H., Pages, F., Sautes-Fridman, C. & Galon, J. The immune contexture in human tumours: impact on clinical outcome. *Nat Rev Cancer* **12**, 298-306 (2012).
79. Cortese, N., Carriero, R., Laghi, L., Mantovani, A. & Marchesi, F. Prognostic significance of tumor-associated macrophages: past, present and future. *Semin Immunol* **48**, 101408 (2020).
80. Deng, L., *et al.* A Novel Mouse Model of Inflammatory Bowel Disease Links Mammalian Target of Rapamycin-Dependent Hyperproliferation of Colonic Epithelium to Inflammation-Associated Tumorigenesis. *American Journal of Pathology* **176**, 952-967 (2010).
81. Vlaicu, P., *et al.* Monocytes/macrophages support mammary tumor invasivity by co-secreting lineage-specific EGFR ligands and a STAT3 activator. *BMC cancer* **13**, 197 (2013).
82. Lizotte, P.H., *et al.* Attenuated reprograms M2-polarized tumor-associated macrophages in ovarian cancer leading to iNOS-mediated tumor cell lysis. *Oncoimmunology* **3**, e28926 (2014).
83. Wyckoff, J.B., *et al.* Direct visualization of macrophage-assisted tumor cell intravasation in mammary tumors. *Cancer research* **67**, 2649-2656 (2007).
84. Qian, B.Z., *et al.* CCL2 recruits inflammatory monocytes to facilitate breast-tumour metastasis. *Nature* **475**, 222-225 (2011).
85. Gazzaniga, S., *et al.* Targeting tumor-associated macrophages and inhibition of MCP-1 reduce angiogenesis and tumor growth in a human melanoma xenograft. *Journal of Investigative Dermatology* **127**, 2031-2041 (2007).
86. Loberg, R.D., *et al.* Targeting CCL2 with systemic delivery of neutralizing antibodies induces prostate cancer tumor regression in vivo. *Cancer research* **67**, 9417-9424 (2007).
87. Sanford, D.E., *et al.* Inflammatory monocyte mobilization decreases patient survival in pancreatic cancer: a role for targeting the CCL2/CCR2 axis. *Clinical Cancer Research* **19**, 3404-3415 (2013).
88. Pyonteck, S.M., *et al.* CSF-1R inhibition alters macrophage polarization and blocks glioma progression. *Nature medicine* **19**, 1264-1272 (2013).
89. Hiratsuka, S., *et al.* The S100A8-serum amyloid A3-TLR4 paracrine cascade establishes a pre-metastatic phase. *Nature cell biology* **10**, 1349-1355 (2008).
90. Liu, C.Y., *et al.* M2-polarized tumor-associated macrophages promoted epithelial-mesenchymal transition in pancreatic cancer cells, partially through TLR4/IL-10 signaling pathway. *Laboratory Investigation* **93**, 844-854 (2013).
91. Ravi, J., Elbaz, M., Wani, N.A., Nasser, M.W. & Ganju, R.K. Cannabinoid receptor-2 agonist inhibits macrophage induced EMT in non-small cell lung cancer by downregulation of EGFR pathway. *Molecular Carcinogenesis* **55**, 2063-2076 (2016).
92. Henze, A.T. & Mazzone, M. The impact of hypoxia on tumor-associated macrophages. *The Journal of clinical investigation* **126**, 3672-3679 (2016).
93. Gatenby, R.A. & Gillies, R.J. Why do cancers have high aerobic glycolysis? *Nat Rev Cancer* **4**, 891-899 (2004).
94. Rodriguez, P.C., *et al.* Arginase I production in the tumor microenvironment by mature myeloid cells inhibits T-cell receptor expression and antigen-specific T-cell responses. *Cancer Res* **64**, 5839-5849 (2004).
95. Geiger, R., *et al.* L-Arginine Modulates T Cell Metabolism and Enhances Survival and Anti-tumor Activity. *Cell* **167**, 829-842 e813 (2016).
96. Zhao, Q., *et al.* Activated CD69+ T cells foster immune privilege by regulating IDO expression in tumor-associated macrophages. *J Immunol* **188**, 1117-1124 (2012).
97. Zheng, X., *et al.* Metabolism in tumour-associated macrophages: a quid pro quo with the tumour microenvironment. *Eur Respir Rev* **29**(2020).
98. Farkona, S., Diamandis, E.P. & Blasutig, I.M. Cancer immunotherapy: the beginning of the end of cancer? *BMC Medicine* **14**, 73 (2016).
99. Kryczek, I., *et al.* B7-H4 expression identifies a novel suppressive macrophage population in human ovarian carcinoma. *Journal of Experimental Medicine* **203**, 871-881 (2006).
100. Aalipour, A., *et al.* Engineered immune cells as highly sensitive cancer diagnostics. *Nature Biotechnology* **37**, 531-+ (2019).

101. Klichinsky, M.*, et al.* Human chimeric antigen receptor macrophages for cancer immunotherapy. *Nat Biotechnol* (2020).
102. Figueiredo, C.R.*, et al.* Blockade of MIF-CD74 Signalling on Macrophages and Dendritic Cells Restores the Antitumour Immune Response Against Metastatic Melanoma. *Frontiers in immunology* **9**, 1132 (2018).
103. Germano, G.*, et al.* Role of macrophage targeting in the antitumor activity of trabectedin. *Cancer cell* **23**, 249-262 (2013).
104. Zeisberger, S.M.*, et al.* Clodronate-liposome-mediated depletion of tumour-associated macrophages: a new and highly effective antiangiogenic therapy approach. *British journal of cancer* **95**, 272-281 (2006).
105. Cieslewicz, M.*, et al.* Targeted delivery of proapoptotic peptides to tumor-associated macrophages improves survival. *Proceedings of the National Academy of Sciences of the United States of America* **110**, 15919-15924 (2013).
106. Luo, Y.*, et al.* Targeting tumor-associated macrophages as a novel strategy against breast cancer. *Journal of Clinical Investigation* **116**, 2132-2141 (2006).
107. Bak, S.P., Walters, J.J., Takeya, M., Conejo-Garcia, J.R. & Berwin, B.L. Scavenger receptor-A-targeted leukocyte depletion inhibits peritoneal ovarian tumor progression. *Cancer research* **67**, 4783-4789 (2007).
108. Roth, F.*, et al.* Aptamer-mediated blockade of IL4Ralpha triggers apoptosis of MDSCs and limits tumor progression. *Cancer research* **72**, 1373-1383 (2012).
109. Puig-Kroger, A.*, et al.* Folate receptor beta is expressed by tumor-associated macrophages and constitutes a marker for M2 anti-inflammatory/regulatory macrophages. *Cancer research* **69**, 9395-9403 (2009).
110. Nagai, T.*, et al.* Targeting tumor-associated macrophages in an experimental glioma model with a recombinant immunotoxin to folate receptor beta. *Cancer Immunology Immunotherapy* **58**, 1577-1586 (2009).
111. Mitchem, J.B.*, et al.* Targeting tumor-infiltrating macrophages decreases tumor-initiating cells, relieves immunosuppression, and improves chemotherapeutic responses. *Cancer research* **73**, 1128-1141 (2013).
112. Schmall, A.*, et al.* Macrophage and Cancer Cell Cross-talk via CCR2 and CX3CR1 Is a Fundamental Mechanism Driving Lung Cancer. *Am J Resp Crit Care* **191**, 437-447 (2015).
113. Paulus, P., Stanley, E.R., Schafer, R., Abraham, D. & Aharinejad, S. Colony-stimulating factor-1 antibody reverses chemoresistance in human MCF-7 breast cancer xenografts. *Cancer research* **66**, 4349-4356 (2006).
114. Aharinejad, S.*, et al.* Colony-stimulating factor-1 blockade by antisense oligonucleotides and small interfering RNAs suppresses growth of human mammary tumor xenografts in mice. *Cancer research* **64**, 5378-5384 (2004).
115. Ries, C.H.*, et al.* Targeting tumor-associated macrophages with anti-CSF-1R antibody reveals a strategy for cancer therapy. *Cancer cell* **25**, 846-859 (2014).
116. Chai, Z.T.*, et al.* microRNA-26a suppresses recruitment of macrophages by down-regulating macrophage colony-stimulating factor expression through the PI3K/Akt pathway in hepatocellular carcinoma. *Journal of hematology & oncology* **8**, 56 (2015).
117. Choi, H.J., Choi, H.J., Chung, T.W. & Ha, K.T. Luteolin inhibits recruitment of monocytes and migration of Lewis lung carcinoma cells by suppressing chemokine (C-C motif) ligand 2 expression in tumor-associated macrophage. *Biochemical and biophysical research communications* **470**, 101-106 (2016).
118. Wang, J. & Kubes, P. A Reservoir of Mature Cavity Macrophages that Can Rapidly Invade Visceral Organs to Affect Tissue Repair. *Cell* **165**, 668-678 (2016).
119. Pulaski, H.L.*, et al.* Identifying alemtuzumab as an anti-myeloid cell antiangiogenic therapy for the treatment of ovarian cancer. *Journal of translational medicine* **7**, 49 (2009).
120. Shime, H.*, et al.* Toll-like receptor 3 signaling converts tumor-supporting myeloid cells to tumoricidal effectors. *Proceedings of the National Academy of Sciences of the United States of America* **109**, 2066-2071 (2012).
121. Felgner, S., Kocijancic, D., Frahm, M. & Weiss, S. Bacteria in Cancer Therapy: Renaissance of an Old Concept. *International journal of microbiology* **2016**, 8451728 (2016).
122. Begnini, K.R., Buss, J.H., Collares, T. & Seixas, F.K. Recombinant Mycobacterium bovis BCG for immunotherapy in nonmuscle invasive bladder cancer. *Applied Microbiology Biotechnology* **99**,

3741-3754 (2015).
123. Banerjee, S., Halder, K., Ghosh, S., Bose, A. & Majumdar, S. The combination of a novel immunomodulator with a regulatory T cell suppressing antibody (DTA-1) regress advanced stage B16F10 solid tumor by repolarizing tumor associated macrophages. *Oncoimmunology* **4**, e995559 (2015).
124. Wang, Q.*, et al.* Interleukin-12 inhibits the hepatocellular carcinoma growth by inducing macrophage polarization to the M1-like phenotype through downregulation of Stat-3. *Molecular and cellular biochemistry* **415**, 157-168 (2016).
125. Coscia, M.*, et al.* Zoledronic acid repolarizes tumour-associated macrophages and inhibits mammary carcinogenesis by targeting the mevalonate pathway. *Journal of cellular and molecular medicine* **14**, 2803-2815 (2010).
126. Rolny, C.*, et al.* HRG inhibits tumor growth and metastasis by inducing macrophage polarization and vessel normalization through downregulation of PlGF. *Cancer cell* **19**, 31-44 (2011).
127. Downey, C.M., Mehrnoosh Aghaei, Schwendener, R.A. & Jirik, F.R. DMXAA causes tumor site-specific vascular disruption in murine non-small cell lung cancer, and like the endogenous non-canonical cyclic dinucleotide STING agonist, 2'3'-cGAMP, induces M2 macrophage repolarization. *PLoS One* **9**, e99988 (2014).
128. Zhang, X.*, et al.* Hydrazinocurcumin Encapsuled nanoparticles "re-educate" tumor-associated macrophages and exhibit anti-tumor effects on breast cancer following STAT3 suppression. *PLoS One* **8**, e65896 (2013).
129. Guiducci, C., Vicari, A., Sangaletti, S., Trinchieri, G. & Colombo, M. Redirecting in vivo elicited tumor infiltrating macrophages and dendritic cells towards tumor rejection. *Cancer research* **65**, 3437-3446 (2005).
130. Beatty, G.L.*, et al.* CD40 agonists alter tumor stroma and show efficacy against pancreatic carcinoma in mice and humans. *Science* **331**, 1612-1616 (2011).
131. Fujiwara, Y., Komohara, Y., Ikeda, T. & Takeya, M. Corosolic acid inhibits glioblastoma cell proliferation by suppressing the activation of signal transducer and activator of transcription-3 and nuclear factor-kappa B in tumor cells and tumor-associated macrophages. *Cancer science* **102**, 206-211 (2011).
132. Horlad, H.*, et al.* Corosolic acid impairs tumor development and lung metastasis by inhibiting the immunosuppressive activity of myeloid-derived suppressor cells. *Molecular nutrition & food research* **57**, 1046-1054 (2013).
133. Wang, C.*, et al.* The MSHA strain of Pseudomonas aeruginosa (PA-MSHA) inhibits gastric carcinoma progression by inducing M1 macrophage polarization. *Tumor Biology* **37**, 6913-6921 (2016).
134. Tan, H.Y.*, et al.* Autophagy-induced RelB/p52 activation mediates tumour-associated macrophage repolarisation and suppression of hepatocellular carcinoma by natural compound baicalin. *Cell Death & Disease* **6**, e1942 (2015).
135. Chakraborty, P.*, et al.* Reprogramming of TAM toward proimmunogenic type through regulation of MAP kinases using a redox-active copper chelate. *Journal of leukocyte biology* **91**, 609-619 (2012).
136. Cai, X.*, et al.* Re-polarization of tumor-associated macrophages to pro-inflammatory M1 macrophages by microRNA-155. *Journal of molecular cell biology* **4**, 341-343 (2012).
137. Squadrito, M.L.*, et al.* miR-511-3p modulates genetic programs of tumor-associated macrophages. *Cell reports* **1**, 141-154 (2012).
138. Boldin, M.P.*, et al.* miR-146a is a significant brake on autoimmunity, myeloproliferation, and cancer in mice. *Journal of Experimental Medicine* **208**, 1189-1201 (2011).
139. Gao, J.*, et al.* Tumor necrosis factor-related apoptosis-inducing ligand induces the expression of proinflammatory cytokines in macrophages and re-educates tumor-associated macrophages to an antitumor phenotype. *Molecular Biology of the Cell* **26**, 3178-3189 (2015).
140. Tan, W.C.C.*, et al.* Overview of multiplex immunohistochemistry/immunofluorescence techniques in the era of cancer immunotherapy. *Cancer Commun (Lond)* **40**, 135-153 (2020).
141. Pinto, M.P.*, et al.* Patient inflammatory status and CD4+/CD8+ intraepithelial tumor lymphocyte infiltration are predictors of outcomes in high-grade serous ovarian cancer. *Gynecol Oncol* **151**, 10-17 (2018).
142. Murakami, T.*, et al.* Multiplexed single-cell pathology reveals the association of CD8 T-cell heterogeneity with prognostic outcomes in renal cell carcinoma. *Cancer Immunol Immunother*

(2021).
143. Nagasawa, S., Kashima, Y., Suzuki, A. & Suzuki, Y. Single-cell and spatial analyses of cancer cells: toward elucidating the molecular mechanisms of clonal evolution and drug resistance acquisition. *Inflamm Regen* **41**, 22 (2021).
144. Chojnacki, A.*, et al.* Intravital imaging allows real-time characterization of tissue resident eosinophils. *Commun Biol* **2**, 181 (2019).
145. Li, W., Germain, R.N. & Gerner, M.Y. High-dimensional cell-level analysis of tissues with Ce3D multiplex volume imaging. *Nat Protoc* **14**, 1708-1733 (2019).
146. Parra, E.R.*, et al.* Identification of distinct immune landscapes using an automated nine-color multiplex immunofluorescence staining panel and image analysis in paraffin tumor tissues. *Scientific Reports* **11**(2021).
147. Mukherjee, S., Sundfeldt, K., Borrebaeck, C.A.K. & Jakobsson, M.E. Comprehending the Proteomic Landscape of Ovarian Cancer: A Road to the Discovery of Disease Biomarkers. *Proteomes* **9**(2021).
148. Yuan, Y. Spatial Heterogeneity in the Tumor Microenvironment. *Cold Spring Harb Perspect Med* **6**(2016).
149. Sarode, P.*, et al.* Reprogramming of tumor-associated macrophages by targeting beta-catenin/FOSL2/ARID5A signaling: A potential treatment of lung cancer. *Sci Adv* **6**, eaaz6105 (2020).
150. Hendry, S.*, et al.* Assessing Tumor-Infiltrating Lymphocytes in Solid Tumors: A Practical Review for Pathologists and Proposal for a Standardized Method from the International Immuno-Oncology Biomarkers Working Group: Part 2: TILs in Melanoma, Gastrointestinal Tract Carcinomas, Non-Small Cell Lung Carcinoma and Mesothelioma, Endometrial and Ovarian Carcinomas, Squamous Cell Carcinoma of the Head and Neck, Genitourinary Carcinomas, and Primary Brain Tumors. *Adv Anat Pathol* **24**, 311-335 (2017).
151. Gorris, M.A.J.*, et al.* Eight-Color Multiplex Immunohistochemistry for Simultaneous Detection of Multiple Immune Checkpoint Molecules within the Tumor Microenvironment. *Journal of Immunology* **200**, 347-354 (2018).
152. Dobin, A.*, et al.* STAR: ultrafast universal RNA-seq aligner. *Bioinformatics* **29**, 15-21 (2013).
153. Liao, Y., Smyth, G.K. & Shi, W. featureCounts: an efficient general purpose program for assigning sequence reads to genomic features. *Bioinformatics* **30**, 923-930 (2014).
154. Love, M.I., Huber, W. & Anders, S. Moderated estimation of fold change and dispersion for RNA-seq data with DESeq2. *Genome Biol* **15**(2014).
155. Weichand, B.*, et al.* S1PR1 on tumor-associated macrophages promotes lymphangiogenesis and metastasis via NLRP3/IL-1beta. *J Exp Med* **214**, 2695-2713 (2017).
156. Feng, Z.P.*, et al.* Multiparametric immune profiling in HPV-oral squamous cell cancer. *Jci Insight* **2**(2017).
157. Salazar, Y.*, et al.* Microenvironmental Th9 and Th17 lymphocytes induce metastatic spreading in lung cancer. *J Clin Invest* **130**, 3560-3575 (2020).
158. Jaykaran. “Mean ± SEM” or “Mean (SD)”? *Indian J Pharmacol* **42**, 329 (2010).
159. Patriarca, C., Macchi, R.M., Marschner, A.K. & Mellstedt, H. Epithelial cell adhesion molecule expression (CD326) in cancer: a short review. *Cancer Treat Rev* **38**, 68-75 (2012).
160. Amsalem, H.*, et al.* Identification of a Novel Neutrophil Population: Proangiogenic Granulocytes in Second-Trimester Human Decidua. *Journal of Immunology* **193**, 3070-3079 (2014).
161. Nakano, A., Harada, T., Morikawa, S. & Kato, Y. Expression of leukocyte common antigen (CD45) on various human leukemia/lymphoma cell lines. *Acta Pathol Jpn* **40**, 107-115 (1990).
162. Lajaunias, F., Dayer, J.M. & Chizzolini, C. Constitutive repressor activity of CD33 on human monocytes requires sialic acid recognition and phosphoinositide 3-kinase-mediated intracellular signaling. *European journal of immunology* **35**, 243-251 (2005).
163. Gowda, M., Payne, K.K., Godder, K. & Manjili, M.H. HLA-DR expression on myeloid cells is a potential prognostic factor in patients with high-risk neuroblastoma. *Oncoimmunology* **2**, e26616 (2013).
164. Collin, M., McGovern, N. & Haniffa, M. Human dendritic cell subsets. *Immunology* **140**, 22-30 (2013).
165. Crittenden, M.R.*, et al.* Mertk on tumor macrophages is a therapeutic target to prevent tumor recurrence following radiation therapy. *Oncotarget* **7**, 78653-78666 (2016).
166. Gautier, E.L.*, et al.* Gene-expression profiles and transcriptional regulatory pathways that underlie the identity and diversity of mouse tissue macrophages. *Nature Immunology* **13**, 1118-1128 (2012).

167. Giroux, M. & Descoteaux, A. Cyclooxygenase-2 expression in macrophages: modulation by protein kinase C-alpha. *J Immunol* **165**, 3985-3991 (2000).
168. Dai, F.*, et al.* The number and microlocalization of tumor-associated immune cells are associated with patient's survival time in non-small cell lung cancer. *BMC Cancer* **10**, 220 (2010).
169. Jackute, J.*, et al.* Distribution of M1 and M2 macrophages in tumor islets and stroma in relation to prognosis of non-small cell lung cancer. *BMC Immunol* **19**, 3 (2018).
170. Rajaganeshan, R.*, et al.* Expression patterns of hypoxic markers at the invasive margin of colorectal cancers and liver metastases. *Ejso-Eur J Surg Onc* **35**, 1286-1294 (2009).
171. Balkwill, F.R., Capasso, M. & Hagemann, T. The tumor microenvironment at a glance. *J Cell Sci* **125**, 5591-5596 (2012).
172. Lee, Y.S.*, et al.* The FBW7-MCL-1 axis is key in M1 and M2 macrophage-related colon cancer cell progression: validating the immunotherapeutic value of targeting PI3K gamma. *Exp Mol Med* **52**, 815-831 (2020).
173. Burgess, D.J. Transcriptomics: Finding structure in gene expression. *Nat Rev Genet* **19**, 249 (2018).
174. Wen, M.*, et al.* Stk38 protein kinase preferentially inhibits TLR9-activated inflammatory responses by promoting MEKK2 ubiquitination in macrophages. *Nat Commun* **6**, 7167 (2015).
175. Mertens, C.*, et al.* Macrophage-derived lipocalin-2 transports iron in the tumor microenvironment. *Oncoimmunology* **7**, e1408751 (2018).
176. Ward, J.M.*, et al.* Progressive glomerulonephritis and histiocytic sarcoma associated with macrophage functional defects in CYP1B1-deficient mice. *Toxicol Pathol* **32**, 710-718 (2004).
177. Yuan, A.*, et al.* Opposite Effects of M1 and M2 Macrophage Subtypes on Lung Cancer Progression. *Sci Rep* **5**, 14273 (2015).
178. Zheng, X.*, et al.* Redirecting tumor-associated macrophages to become tumoricidal effectors as a novel strategy for cancer therapy. *Oncotarget* **8**, 48436-48452 (2017).
179. Amanzada, A.*, et al.* Identification of CD68(+) neutrophil granulocytes in in vitro model of acute inflammation and inflammatory bowel disease. *Int J Clin Exp Pathol* **6**, 561-570 (2013).
180. Gottfried, E.*, et al.* Expression of CD68 in non-myeloid cell types. *Scand J Immunol* **67**, 453-463 (2008).
181. Ohri, C.M., Shikotra, A., Green, R.H., Waller, D.A. & Bradding, P. Macrophages within NSCLC tumour islets are predominantly of a cytotoxic M1 phenotype associated with extended survival. *Eur Respir J* **33**, 118-126 (2009).
182. Li, Z.*, et al.* The intratumoral distribution influences the prognostic impact of CD68- and CD204-positive macrophages in non-small cell lung cancer. *Lung Cancer* **123**, 127-135 (2018).
183. Rakaee, M.*, et al.* Prognostic Value of Macrophage Phenotypes in Resectable Non-Small Cell Lung Cancer Assessed by Multiplex Immunohistochemistry. *Neoplasia* **21**, 282-293 (2019).
184. Lim, J.C.T.*, et al.* An automated staining protocol for seven-colour immunofluorescence of human tissue sections for diagnostic and prognostic use. *Pathology* **50**, 333-341 (2018).
185. Taube, J.M.*, et al.* The Society for Immunotherapy of Cancer statement on best practices for multiplex immunohistochemistry (IHC) and immunofluorescence (IF) staining and validation. *J Immunother Cancer* **8**(2020).
186. Rajaganeshan, R.*, et al.* Expression patterns of hypoxic markers at the invasive margin of colorectal cancers and liver metastases. *Eur J Surg Oncol* **35**, 1286-1294 (2009).
187. Jeong, H.*, et al.* Tumor-Associated Macrophages Enhance Tumor Hypoxia and Aerobic Glycolysis. *Cancer research* **79**, 795-806 (2019).
188. Herzig, S. & Shaw, R.J. AMPK: guardian of metabolism and mitochondrial homeostasis. *Nat Rev Mol Cell Biol* **19**, 121-135 (2018).
189. Miller, A.*, et al.* Exploring Metabolic Configurations of Single Cells within Complex Tissue Microenvironments. *Cell Metab* **26**, 788-+ (2017).
190. Barua, S.*, et al.* Spatial interaction of tumor cells and regulatory T cells correlates with survival in non-small cell lung cancer. *Lung Cancer* **117**, 73-79 (2018).
191. Mund, A., Coscia, F. & Mann, M. AI-driven Deep Visual Proteomics defines cell identity and heterogeneity. *bioRxiv* **doi: https://doi.org/10.1101/2021.01.25.427969**(2021).
192. Zilionis, R.*, et al.* Single-Cell Transcriptomics of Human and Mouse Lung Cancers Reveals Conserved Myeloid Populations across Individuals and Species. *Immunity* **50**, 1317-+ (2019).
193. Gao, J.J.*, et al.* Integrative Analysis of Complex Cancer Genomics and Clinical Profiles Using the cBioPortal. *Sci Signal* **6**(2013).
194. Cancer Genome Atlas Research, N.*, et al.* The Cancer Genome Atlas Pan-Cancer analysis project.

Nat Genet **45**, 1113-1120 (2013).
195. Ohfuchi, E.*, et al.* Vertebrate Arp6, a novel nuclear actin-related protein, interacts with heterochromatin protein 1. *Eur J Cell Biol* **85**, 411-421 (2006).
196. Wei, C.Y.*, et al.* Bioinformatics-based analysis reveals elevated MFSD12 as a key promoter of cell proliferation and a potential therapeutic target in melanoma. *Oncogene* **38**, 1876-1891 (2019).
197. Carstens, J.L.*, et al.* Spatial computation of intratumoral T cells correlates with survival of patients with pancreatic cancer. *Nat Commun* **8**, 15095 (2017).
198. Marusyk, A.*, et al.* Spatial Proximity to Fibroblasts Impacts Molecular Features and Therapeutic Sensitivity of Breast Cancer Cells Influencing Clinical Outcomes. *Cancer research* **76**, 6495-6506 (2016).
199. Tsuchiyama, T., Nakamoto, Y., Sakai, Y., Mukaida, N. & Kaneko, S. Optimal amount of monocyte chemoattractant protein-1 enhances antitumor effects of suicide gene therapy against hepatocellular carcinoma by M1 macrophage activation. *Cancer science* **99**, 2075-2082 (2008).
200. Malam, Y., Loizidou, M. & Seifalian, A.M. Liposomes and nanoparticles: nanosized vehicles for drug delivery in cancer. *Trends in pharmacological sciences* **30**, 592-599 (2009).
201. Alizadeh, D., Zhang, L., Hwang, J., Schluep, T. & Badie, B. Tumor-associated macrophages are predominant carriers of cyclodextrin-based nanoparticles into gliomas. *Nanomedicine* **6**, 382-390 (2010).
202. Mohammadi, M.*, et al.* Folate receptor targeted three-layered micelles and hydrogels for gene delivery to activated macrophages. *J Control Release* **244**, 269-279 (2016).
203. Abebe, D.G.*, et al.* Three-Layered Biodegradable Micelles Prepared by Two-Step Self-Assembly of PLA-PEI-PLA and PLA-PEG-PLA Triblock Copolymers as Efficient Gene Delivery System. *Macromol Biosci* **15**, 698-711 (2015).
204. Schwendener, R.A., Lagocki, P.A. & Rahman, Y.E. The effects of charge and size on the interaction of unilamellar liposomes with macrophages. *Biochim Biophys Acta* **772**, 93-101 (1984).
205. Ahsan, F., Rivas, I.P., Khan, M.A. & Torres Suarez, A.I. Targeting to macrophages: role of physicochemical properties of particulate carriers--liposomes and microspheres--on the phagocytosis by macrophages. *Journal of controlled release : official journal of the Controlled Release Society* **79**, 29-40 (2002).
206. Kelly, C., Jefferies, C. & Cryan, S.A. Targeted liposomal drug delivery to monocytes and macrophages. *Journal of Drug Delivery* **2011**, 727241 (2011).
207. Etzerodt, A.*, et al.* Efficient intracellular drug-targeting of macrophages using stealth liposomes directed to the hemoglobin scavenger receptor CD163. *Journal of controlled release : official journal of the Controlled Release Society* **160**, 72-80 (2012).
208. Kuramoto, Y.*, et al.* Mannosylated cationic liposomes/CpG DNA complex for the treatment of hepatic metastasis after intravenous administration in mice. *Journal of Pharmaceutical Sciences* **98**, 1193-1197 (2009).
209. Eleftheriadis, T.*, et al.* Dichloroacetate at therapeutic concentration alters glucose metabolism and induces regulatory T-cell differentiation in alloreactive human lymphocytes. *J Basic Clin Physiol Pharmacol* **24**, 271-276 (2013).
210. Puchalska, P.*, et al.* Isotope Tracing Untargeted Metabolomics Reveals Macrophage Polarization-State-Specific Metabolic Coordination across Intracellular Compartments. *Iscience* **9**, 298-+ (2018).
211. Jenkins, R.W., Barbie, D.A. & Flaherty, K.T. Mechanisms of resistance to immune checkpoint inhibitors. *Br J Cancer* **118**, 9-16 (2018).

Appendix

List of abbreviation

ADC	adenocarcinoma
ALK	anaplastic lymphoma kinase
ASS	arginine-succinate synthetase
BCG	Bacillus Calmette-Guérin
BET	bromoand extraterminal
CAF	cancer-associated fibroblast
CB2	cannabinoid receptor 2
ChIP	Chromatin immunoprecipitation
Co-IP	Co-Immunoprecipitation
CpG	5′-cytosine-phosphate-guanine-3′ dinucleotide
CpG-ODN	CpG-oligodeoxynucleotide
CSC	cancer stem-like cells
CSF1	colony-stimulating factor 1
CTL	cytotoxic lymphocytes
CTLA-4	cytotoxic T lymphocyte antigen 4
CuNG	copper N-(2-hydroxy acetophenone) glycinate
DAPI	4', 6-diamidino-2-phenylindole
DC	dendritic cell
DMSO	dimethylsulfoxide
DMXAA	5,6-dimethylxanthenone-4-acetic acid
DNMT	DNA methyltransferase
DSP	digital spatial profiling
DVP	deep visual protemoics
ECM	extracellular matrix
EGF	epidermal growth factor
EGFR	epidermal growth factor receptor
ELISA	enzyme-linked immunosorbent assay
EML4	echinoderm microtubule-associated protein-like 4
EMP	erythro-myeloid progenitor
ERK	extracellular signal-regulated kinase
FA	folic acid
FADD	Fas-associated protein with death domain
FCS	fetal calf serum
FMO	fluorescence minus one control
FRβ	folate receptor beta
GM-CSF	granulocyte-macrophage colony-stimulating factor
H&E	Haematoxylin & Eosin
HAT	histone acetyltransferase
HDAC	histone deacetylase
HDM	histone demethylase

HER2	epidermal growth factor receptor 2
HIF-1α	hypoxia-inducible factor 1α
HLA	human leukocyte antigen
HME	histone-modifying enzyme
HMT	histone methyltransferase
HPRT	hypoxanthine phosphoribosyltransferase1
HRP	having horse radish peroxidase
HUVEC	human umbilical vein endothelial cell
ICC	Immunocytochemistry
ICI	immune checkpoint inhibitor
IFC	immunofluorescence staining
IFNγ	Interferon-γ
IM	invasive margin
IRF3	interferon regulatory factor 3
IVC	individually ventilated cage
KIF5B	kinesin family member 5B
KIR	killer immunoglobulin-like receptor
KRAS	kirsten rat sarcoma viral oncogene homolog
LAG-3	lymphocyte activation gene 3
LCC	large-cell carcinoma
lncRNA	long noncoding RNA
LPS	lipopolysaccharides
mAbs	monoclonal antibodies
MAP2K1	mitogen-activated protein kinase 1
MC	mast cell
MCP1	monocyte chemoattractant protein-1
M-CSF	macrophage colony-stimulating factor
MDSC	myeloid-derived suppressor cell
micro-CT	micro-computerized tomography
MLL	methyltransferase myeloid lymphoid leukemia
MS	mass-spectrometry
NF-κB	nuclear factor κB
NK	natural killer
NPM	nucleophosmin
NSCLC	non-small-cell lung cancer
PBS	phosphate-buffered saline
PD-1	death protein 1
PGE2	prostaglandin E2
PIK3CA	Phosphatidylinositol-4,5-Bisphosphate 3-Kinase, catalytic subunit alpha
PlGF	placental growth factor
PPAR	peroxisome proliferator-activated receptor
qRT-PCR	quantitative real-time polymerase chain reaction

RRM1	ribonucleotide reductase M1
S1P	sphingosine-1-phosphate
SCC	squamous cell carcinoma
SCLC	small-cell lung cancer
STAT1	signal transducer and activator of transcription 1
TAM	tumor-associated macrophage
TC	tumor center
TF	transcription factor
TGFβ	transforming growth factor beta
TICAM-1	TLR3/Toll–IL1 receptor domain–containing adaptor molecule 1
TIGIT	T cell immunoreceptor with Ig and ITIM domains
Tim-3	T-cell immunoglobulin domain and mucin domain-3
TKIs	tyrosine kinase inhibitors
TLR	toll-like receptor
TMA	Tissue microarray
TME	tumoral microenvironment
TNF-α	tumor necrosis factor α
TRAILR	TNF-related apoptosis inducing ligand receptor
TSA	Tyramide signal amplification
VEGF	vascular endothelial growth factor
WHO	World Health Organization
WT	wild type
αKG	α-ketoglutarate
α-SMA	α-smooth muscle actin

List of reagents

Items	Affiliation	Catlog/specifications
Companion plates	BD BioSciences	353504 (24-well)
BCA assay	Thermo Fisher Scientific	23225
BD Falcon cell culture insert	Corning	353097
Cell Death Detection ELISAPLUS	Roche Applied Science	11920685001
Cell proliferation ELISA BrdU kit	Roche	11647229001 (colorimetric)
Chloroform	Sigma-Aldrich	67-66-3
Complete protease inhibitors	Sigma-Aldrich	11697498001
Crystal Violet solution	Sigma-Aldrich	548-62-9
Dimethylsulfoxide	Sigma-Aldrich	67-68-5
DMEM medium	Gibco	41966029
DMEM/F-12 medium	Gibco	11320033
DTT	Sigma-Aldrich	646563
Endothelial cell growth medium	Sigma-Aldrich	211-500
Eosin Y	AppliChem	AP253999.1210
FCS	Th. Geyer	S181B-500
Ficoll	GE Healthcare	17144002
HEPEs	Gibco	15630080
High Capacity cDNA Reverse Transcription Kit	Applied Biosystems	4368814
IL4	R&D Systems	204-IL-010 (human)
IL4	R&D Systems	404-ML (mouse)
Interferon-γ	R&D Systems	485-MI (mouse)
Interferon-γ	R&D Systems	285-IF-100 (human)
Leucosep™ Centrifuge Tube	Greiner Bio-One	227289
Lipopolysaccharide	Sigma-Aldrich	L2630 (from Escherichia coli O111:B4)
Matrigel	BD Biosciences	354234
Mayer's hematoxylin	AppliChem	254766
M-CSF	R&D Systems	416-ML (mouse)
Mycoplasma PCR Detection Kit	Sigma-Aldrich	MP0035
Opti-MEM medium	Gibco	31985054
Penicillin/streptomycin	Gibco	15140122
Percoll	GE Healthcare	17-0891-01
PerkinElmer Opal kit	PerkinElmer	NEL811001KT
Pertex	Medite GmbH	LEIC811
Phosphate buffered saline	Gibco	10010023
Poly-D-Lysine culture dishes	Thermo Fisher Scientific	152035
PowerUp™ SYBR™ Green Master Mix	Applied Biosystems	A25741
RIPA buffer	Santa Cruz Biotechnology	sc-24948
RPMI medium	Gibco	21875034
Trizol	Thermo Fisher Scientific	15596026
Trypsin	Thermo Fisher Scientific	25200056

List of figures and tables from external sources

Caption	Reference	Own publication (yes vs. no)
Figure 1	Ferlay, J. et al, International Journal of Cancer, 2019 [1]	No
Figure 3	Zheng et al., Oncotarget, 2017 [45]	Yes
Figure 4	Zheng et al., Oncotarget, 2017 [45]	Yes
Table 1	Zheng et al., Oncotarget, 2017 [45]	Yes
Table 11	Zheng et al., Cancer Research 2020 [61]	Yes
Figure 11	Zheng et al., Cancer Research 2020 [61]	Yes
Figure 12	Zheng et al., Cancer Research 2020 [61]	Yes
Figure 15	Zheng et al., Cancer Research 2020 [61]	Yes
Table 12	Zheng et al., Cancer Research 2020 [61]	Yes
Figure 17	Zheng et al., Cancer Research 2020 [61]	Yes
Figure 18	Zheng et al., Cancer Research 2020 [61]	Yes
Figure 19	Zheng et al., Cancer Research 2020 [61]	Yes
Table 13	Zheng et al., Cancer Research 2020 [61]	Yes
Table 14	Zheng et al., Cancer Research 2020 [61]	Yes
Figure 20	Zheng et al., Cancer Research 2020 [61]	Yes
Figure 21	Zheng et al., Cancer Research 2020 [61]	Yes
Figure 22	Zheng et al., Cancer Research 2020 [61]	Yes
Figure 23	Zheng et al., Cancer Research 2020 [61]	Yes
Figure 24	Zheng et al., Cancer Research 2020 [61]	Yes

List of publications

X. Zheng, A. Weigert, S. Reu, S. Guenther, S. Mansouri, B. Bassaly, S. Gattenlöhner, F. Grimminger, S. Pullamsetti, W. Seeger, H. Winter, and R. Savai. Spatial density and distribution of tumor-associated macrophages predict survival in non-small-cell lung carcinoma. ***Cancer Research***, 2020; 80: 4414–25. (Selected as journal cover)

X. Zheng, S. Mansouri, A. Krager, F. Grimminger, W. Seeger, S. S. Pullamsetti, C. E. Wheelock, and R. Savai. Metabolism in tumor-associated macrophages: a quid pro quo with the tumor microenvironment. ***European Respiratory Review***, 2020; 0: 200134.

Sarode, P., **X. Zheng**, G. A. Giotopoulou, A. Weigert, C. Kuenne, S. Gunther, A. Friedrich, S. Gattenlohner, T. Stiewe, B. Brune, F. Grimminger, G. T. Stathopoulos, S. S. Pullamsetti, W. Seeger, and R. Savai. Tumor-associated macrophage-specific β-catenin-FOSL2-ARID5A axis is a major driver of macrophage reprogramming and progression of lung cancer. ***Science Advances***, 2020; 6(23): eaaz6105.

Salazar, Y., **X. Zheng**, D. Brunn, H. Raifer, F. Picard, Y. Zhang, H. Winter, S. Guenther, A. Weigert, B. Weigmann, L. Dumoutier, J. C. Renauld, A. Waisman, A. Schmall, A. Tufman, L. Fink, B. Brune, T. Bopp, F. Grimminger, W. Seeger, S. S. Pullamsetti, M. Huber, and R. Savai: Microenvironmental Th9- and Th17- lymphocytes induce metastatic spreading in lung cancer. ***Journal of Clinical Investigation***, 2020; 130(7):3560-3575. (Selected as journal cover)

Solimani, F., R. Pollmann, T. Schmidt, A. Schmidt, **X. Zheng**, R. Savai, S. Muhlenbein, J. Pickert, V. Eubel, C. Mobs, R. Eming, and M. Hertl. Therapeutic targeting of Th17/Tc17 cells leads to clinical improvement of lichen planus. ***Frontiers in Immunology***, 2019; 10.

X. Zheng, K. Turkowski, J. Mora, B. Brune, W. Seeger, A. Weigert, and R. Savai. Redirecting tumor-associated macrophages to become tumoricidal effectors as a novel strategy for cancer therapy. ***Oncotarget***, 2017; 8(29):48436-48452.

X. Zheng, J. Zhou, B. Zhang, J. Zhang, J. Wilson, L. Gu, B. Zhu, J. Gu, J. Ji, and D. Deng. Critical evaluation of *Cbx7* downregulation in primary colon carcinomas and its clinical significance in Chinese patients. ***BMC Cancer***, 2015; 15:145.

X. Zheng, D. Deng: Functions of Polycomb group proteins and spatio-temporal patterns of their expressions. ***Chinese Journal of Biochemistry and Molecular Biology***, 2014; 30(5):415-420.

A. Weigert*, **X. Zheng***, A. Asafova*, …..R. Savai.: Fibrocytes boost the lung cancer niche via the endothelin system. ***Nature Communications***. Submitted (*equal contribution)

X. Zheng, …, R. Savai.: HDAC2 augments lung cancer progression by orchestrating tumor-associated macrophage phenotype. (Manuscript in preparation)

List of contributions to the congress

26/01/2020	Poster prize winner 9th annual meeting of the German Center for Lung Research (DZL), Travemünde , Germany
07/02/2019	Poster prize winner 8th annual meeting of the DZL, Mannheim, Germany
22/11/2018	Speaker Max Planck Institute retreat, Bad Marienberg, Germany
25/09/2018	Poster Frankfurt Cancer Conference, Frankfurt, Germany
08/02/2018	Poster DZL annual meeting, Bad Nauheim, Germany
18/09/2017	Best poster winner International Max Planck Research School retreat, Munich, Germany
09/09/2017	Poster European Respiratory Society (ERS) international congress, Milan, Italy
08/07/2017	Poster ECCPS retreat, Bad Nauheim, Germany
19/05/2017	Speaker and International Trainee Scholarship Award winner American Thoracic Society 2017 international conference, Washington, DC., America
23/03/2017	Speaker and William MacNee Award winner 15th Lung Science Conference of ERS, Estoril, Portugal
29/01/2017	Speaker 6th annual meeting of DZL, Munich, Germany
16/11/2016	Poster Max Planck Institute retreat, Germany
07/07/2016	Poster ECCPS retreat, Germany

Erklärung zur Dissertation

„Hiermit erkläre ich, dass ich die vorliegende Arbeit selbständig und ohne unzulässige Hilfe oder Benutzung anderer als der angegebenen Hilfsmittel angefertigt habe. Alle Textstellen, die wörtlich oder sinngemäß aus veröffentlichten oder nichtveröffentlichten Schriften entnommen sind, und alle Angaben, die auf mündlichen Auskünften beruhen, sind als solche kenntlich gemacht. Bei den von mir durchgeführten und in der Dissertation erwähnten Untersuchungen habe ich die Grundsätze guter wissenschaftlicher Praxis, wie sie in der „Satzung der Justus-Liebig-Universität Gießen zur Sicherung guter wissenschaftlicher Praxis“ niedergelegt sind, eingehalten sowie ethische, datenschutzrechtliche und tierschutzrechtliche Grundsätze befolgt. Ich versichere, dass Dritte von mir weder unmittelbar noch mittelbar geldwerte Leistungen für Arbeiten erhalten haben, die im Zusammenhang mit dem Inhalt der vorgelegten Dissertation stehen, oder habe diese nachstehend spezifiziert. Die vorgelegte Arbeit wurde weder im Inland noch im Ausland in gleicher oder ähnlicher Form einer anderen Prüfungsbehörde zum Zweck einer Promotion oder eines anderen Prüfungsverfahrens vorgelegt. Alles aus anderen Quellen und von anderen Personen übernommene Material, das in der Arbeit verwendet wurde oder auf das direkt Bezug genommen wird, wurde als solches kenntlich gemacht. Insbesondere wurden alle Personen genannt, die direkt und indirekt an der Entstehung der vorliegenden Arbeit beteiligt waren. Mit der Überprüfung meiner Arbeit durch eine Plagiatserkennungssoftware bzw. ein internetbasiertes Softwareprogramm erkläre ich mich einverstanden.“

Copenhagen 08,10,2021 _____

Ort, Datum Unterschrift

Acknowledgement

I would like to convey my sincere gratitude to Prof. Werner Seeger and Dr. Rajkumar Savai for accepting me to pursue a doctoral study at Max Planck Institute for Heart and Lung Research and the supervision throughout my studies. Their continuous guidance brought my work to a higher level. I highly appreciate their scientific dedication that constantly inspires me to widen my research from various perspectives.

I am indebted to the following scientists for their insightful advice and valuable assistance in troubleshooting: Dr. Jianning Zhao, Dr. Jochen Wilhelm, Dr. Andreas Weigert and Dr. Nefertiti El-Nikhely. I would like to acknowledge my colleagues Dr. Ylia Salazar, Siavash Mansouri, Poonam Sarode, David Brunn and Dr. Rui Gao for stimulating discussions and constructive suggestions. My thanks also goes to Marianne Hoeck, Yanina Knepper, Jeanette Knepper and Margarete Mijatovic, who provided superb technical support.

In addition, I would like express my thanks to my beloved family: my parents, grandma and Jianning for their wise counsel and sympathetic ear. They are there for me every step of the way, and I appreciate everything they have done for me. Finally, I could not have completed doctoral research without the support of my treasured friends Han Xu, Ruofei Yu, Hicham Houhou, Yanli Xu, Rui Xu and Yanyan Zhao. They are always there for me.